THESIS FOR THE DEGREE OF LICENTIATE OF ENGINEERING

Flame Characterisation and Nitrogen Oxides Assessment of Coal Replacement with Hydrogen in Rotary Kilns for Iron Ore Induration

SAMUEL COLIN

Department of Space, Earth and Environment

CHALMERS UNIVERSITY OF TECHNOLOGY

Gothenburg, Sweden 2025

Flame Characterisation and Nitrogen Oxides Assessment of Coal Replacement with Hydrogen in Rotary Kilns for Iron Ore Induration

SAMUEL COLIN

Department of Space, Earth and Environment

Chalmers University of Technology

SE-412 96 Gothenburg

Sweden

Telephone + 46 (0)31-772 1000

Printed by Chalmers Reproservice,

Gothenburg, Sweden 2025

Flame Characterisation and Nitrogen Oxides Assessment of Coal Replacement with Hydrogen in Rotary Kilns for Iron Ore Induration

SAMUEL COLIN

Department of Space, Earth and Environment

Chalmers University of Technology

Abstract: The iron and steel industry is a major contributor to global CO_2 emissions, largely due to the reliance on fossil fuel combustion, as well as emissions of nitrogen oxides (NO_x) due to high temperatures flames and fuel-nitrogen content. The induration of iron ore pellets is small but increasingly important step in the global iron and steel industry. The major rote for the European mining industry dominated by the Swedish mining company LKAB. In the electrification of the Swedish mining industry, LKAB seeks to substitute coal by hydrogen with hydrogen-coal co-firing as an intermediate solution. The replacement of coal with hydrogen presents both technical challenges, particularly in controlling flame behaviour and mitigating NO_x formation, as well as economic challenges, in capital intensive investments and uncertain energy markets.

This thesis investigates flame characteristics (such as flame area, stability, ignition zone, and particle temperature) and NO_x formation during hydrogen-coal co-firing under kiln conditions. The work focuses on a scenario in which 30% of the kiln heat demand is covered by hydrogen. A combination of experimental work and modelling is employed to assess flame behaviour and to identify optimal strategies for full-scale implementation of hydrogen-coal co-firing. Specific research objectives include defining the interactions between hydrogen and coal during combustion, and tailoring burner designs and hydrogen injection methods to enhance performance.

The results show that introducing a solid fuel into a gaseous flame environment rapidly shifts the combustion dynamics towards a predominantly solid fuel flame. Meanwhile, low amounts of hydrogen significantly improve the flame stability, intensity, and ignition of coal combustion. In a 30%-hydrogen combi-burner set-up, reducing the hydrogen velocity enhances flame stability. Lancing configurations exhibit reduced flame stability, delayed ignition, and decreased flame area and intensity as the distance between the hydrogen and coal injection sites increases.

Regarding NO_x formation, the formation of NO_x from the nitrogen bound in the fuel dominates the emissions profiles for both lignite and bituminous coal. Early release of volatile nitrogen compounds helps reduce the overall level of NO_x formation.

For hydrogen-coal co-firing, combi-burners consistently achieve lower NO_x emissions than coal-only firing. In contrast, NO_x performance in hydrogen lancing varies with the design parameters. Positioning the hydrogen lance closer to the coal burner improves NO_x performance. However, hydrogen inlet velocity is critical: a higher hydrogen velocity close to the coal burner increases NO_x formation, while a higher velocity in distant lancing configurations reduces NO_x emissions.

Future work will expand these findings to larger-scale systems and develop advanced measurement techniques for more-precise flame characterisation and NO_x control strategies.

Keywords: Co-firing gaseous and solid fuel, hydrogen, coal, carbon dioxide, nitrogen oxides (NO_x), spectroscopy, photo analysis, lancing, iron and steel-making

Acknowledgements

With heartfelt gratitude, I extend my deepest thanks to my mentors. To Fredrik Normann, whose continuous guidance and support throughout this research helped keep my boundless curiosity in check. To Klas Andersson and Adrian Gunnarsson, whose expertise and steady hands played a crucial role in shaping this work. To Francisco Javier Triana de las Heras, for the philosophical discussions and your meticulous feedback that sharpened my thinking. To Alexey Sepman, for your generosity in sharing knowledge and for the time you spent guiding me through a new area of Science (for me).

A special note of appreciation to my colleagues at LKAB, where knowledge met practice and theory met reality. Thanks to my colleagues and collaborators for the conversations that sparked new ideas and the insights that deepened my understanding. Special thanks to Christian Fredriksson for his shared knowledge and guidance, to Simon Töyrä for his invaluable support and countless hours spent explaining real-world applications, and to Johan Siikavaara for his dedication to supporting climate strategy and his open-ness to exploring solutions.

To my family, my greatest foundation – Marleen, your love has been my safe harbour, your patience a quiet force propelling me forward. Navigating the many dimensions of my life would have been impossible without your support and unshakable kindness. Milo and Norvid, your laughter has lifted the weight of endless hours studying the complexity and sometimes heaviness of the world, reminding me of life's simplest joys and offering perspective.

To my parents, who nurtured my curiosity and encouraged my ever-winding path, giving me unwavering faith. To my brother, for the countless enjoyable hours spent creating music projects together, exploring other ways to express the challenges revealed by Science, and for the hikes and deep conversations that have broadened my perspective and understanding of the world. To my sister, for her strength in demonstrating the importance of staying true to one's values, an enduring source of inspiration.

And to all who have offered a helping hand, a thoughtful word or a simple act of kindness along the way, I extend my deepest gratitude.

Gothenburg, Sweden

March 2025

LIST OF PUBLICATION

The thesis is based on the following appended papers, which are referred to in the text by their Roman numerals:

I. Colin, S.; Normann, F.; Fredriksson, C.; Andersson, K., Flame Characterization of Cofiring Gaseous and Solid Fuels in Suspensions. ACS Omega 2024, 9, 28268−28282.

II. Johansson, A.; Fernberg, J.; Sepman, A.; Colin, S.; Wennebro, J.; Normann, F.; Wiinikka, H. Cofiring of Hydrogen and Pulverized Coal in Rotary Kilns Using One Integrated Burner. International Journal of Hydrogen Energy 2024, 90, 342–352.

III. Colin, S.; Triana De Las Heras, F. J.; Normann, F.; Johansson, A.; Fernberg, J.; Sepman, A.; Wennebro, J.; and Wiinikka, H., Configuring Hydrogen Lancing to Reduce Carbon and Nitrogen Oxides Emissions from Coal-Fired Rotary Kilns with NOx Management. Accepted

Author contributions

Samuel Colin is the principal author of **Papers I** and **III**, having conducted the writing and visualisation, as well as the formal analysis. He also made major contributions to the writing and data analysis of **Paper II**. Samuel performed the experimental campaign in **Paper I**. In **Papers II** and **III**, Andreas Johansson, Johannes Fernberg, Alexey Sepman, Jonas Wennebro and Henrik Wiinikka conducted the experimental campaigns, while the campaign was conceptualised and the burner and lancing concepts were designed by Samuel Colin and Fredrik Normann. Andreas Johansson is the principal author of **Paper II**, with responsibility for writing and visualisation. Alexey Sepman conducted the TDLAS measurements in **Papers II** and **III**. Francisco Javier Triana De Las Heras contributed with the image analysis and associated discussions of **Paper III**.

We expend a lot of effort to improve the external conditions of our lives, but in the end it is always the mind that creates our experience of the world and translates this experience into either well-being or suffering. If we transform our way of perceiving things, we transform the quality of our lives.

Matthieu Ricard

TABLE OF CONTENTS

1 Introduction 1

1.1 Aims and scope 2

1.2 Content of the thesis 3

2 Background 5

2.1 Importance of limiting climate change 5

2.2 Technical causes for climate change 7

2.3 Which societal parameter impacts CO_2 emissions? – The Kaya identity 8

2.3.1 The term: $\boldsymbol{Population}$ 9

2.3.2 The term: $\boldsymbol{EnergyGDP}$ 10

2.3.3 The term: $\boldsymbol{GDPPopulation}$ 10

2.3.4 The term: $\boldsymbol{CO2Energy}$ 13

2.4 Importance of decarbonising the iron and steel industry 14

2.5 CO_2 partitioning of the iron and steel industry 16

2.6 H_2 strategy 18

2.7 Pelletising process 20

2.8 Importance of the flame characteristics for the grate-kiln pelletising process 25

2.8.1 Impacts of the flame characteristics and fuel on the stability of the process 25

2.8.2 Impacts of the flame on pellet quality 26

2.9 Work extendable to other applications 30

2.10 Combustion-related pollutants 31

2.11 Summary - Transitioning to a low-CO_2 fuel - Questions to answer 32

3 Co-firing of gaseous and solid fuels 33

3.1 Literature review of flame characteristics and NO_x emissions in co-firing solid and gaseous fuels 33

3.2 Formation of nitrogen oxide 36

3.2.1 Zeldovich mechanism 36

3.2.2 The NNH Route mechanism 37

3.2.3 N_2O route 38

3.2.4 Fenimore Mechanism (Prompt NO) 38

3.2.5 Nitrogen route for fuel nitrogen content (Fuel-N) 38

3.3 Nitrogen path in co-firing hydrogen and coal 43

3.4 Scaling up flames 44

4 Method 47

4.1 Step 1: Flame Characteristics in Co-Firing Gaseous and Solid Fuels 49

4.1.1 Chalmers 100-kW furnace 49
4.1.2 Burner 50
4.1.3 Fuels 51
4.1.4 Modelling 51
4.2 Step 2: Pilot-Scale Trials 52
4.2.1 Horizontal industrial combustion kiln – 150 kW 52
4.2.2 Combi-burner design HICK 53
4.2.3 Lancing design HICK 55
4.2.4 Fuel 57
4.3 Step 3: Up-Scaling and Demonstration 59
4.3.1 Experimental combustion furnace – 580 kW 59
4.3.2 Properties of fuels 60
4.4 Hydrogen Flame Diagnostics 60
4.5 Measurement Devices for Flame Characterisation 61
4.5.1 Fourier-Transform Infrared Spectroscopy (FTIR) 61
4.5.2 Non-Dispersive Infrared (NDIR) Spectroscopy 61
4.5.3 Electrochemical Sensors 62
4.5.4 Paramagnetic Sensors 62
4.5.5 Non-Dispersive Ultra-Violet (NDUV) Spectroscopy 62
4.5.6 Tuneable Diode Laser Absorption Spectroscopy (TDLAS) 62
4.5.7 Broadband Absorption Spectroscopy (BAS) 63
4.5.8 Emission spectroscopy in UV and VIS 63
4.5.9 IFRF Total heat flux and radiative heat flux 63
4.5.10 Cameras 63
5 Flame characteristics during co-firing 65
5.1 Step 1: Co-firing Lignite and Propane (Paper I) 65
5.2 Step 2: Co-firing Sub-bituminous Coal and Hydrogen (Papers II & III) 67
5.3 Full-Scale Observations: Coal and Oil Flames 69
6 NO_x Formation during Hydrogen-Coal Co-firing 71
6.1 Step 1: Co-firing Lignite and Propane (Paper I) 71
6.2 Step 2: Co-firing Sub-bituminous Coal and Hydrogen (Papers II & III) 74
6.3 Scaling comparison measurements 78
7 On-going work 81
7.1 Measurement of Flame Temperature via OH* Chemiluminescence 81
7.2 Scaling-up Co-firing of Coal and Hydrogen 82
8 Conclusion 83

NOMENCLATURE:

BF	Blast furnace for iron-making process.
BF pellets	Iron-ore pellets optimised for reduction in a blast furnace.
Burner	A single fuel burner that uses primary air.
Chalmers Unit	The Chalmers 100-kW experimental furnace used for **Paper I**.
Char-N	Nitrogen that is chemically bound into a solid char matrix, i.e., Fuel-N not released as Vol-N.
Char-NO	NO that is formed from the oxidation of Char-N.
Combi-burner:	A burner that is operated with at least two fuels and primary air.
DR pellets	Iron-ore pellets optimised for reduction in a direct reduction shaft furnace.
DRI	Direct reduction shaft furnace for iron-making process.
ECF	Experimental combustion furnace, which is the LKAB 580-kW experimental furnace used for on-going work.
EROI	Energy return on investment.
Fuel-N	Nitrogen that is chemically bound into a solid fuel.
Fuel-NO	NO that is formed from the oxidation of Fuel-N.
GK	Grate-rotary kiln
HICK	Horizontal industrial combustion kiln, which is the RISE 150-kW experimental furnace used for **Papers II** and **III**.
IPCC	The Intergovernmental Panel on Climate Change (IPCC)
IR	Infra-red wavelengths in the range of 700 nm to 1 mm (Near-IR:700–1,400 nm; Mid-IR: 1,400–3,000 nm; Far-IR: 3,000 nm–1 mm).
Lancing	Condition in which one fuel is injected into the furnace without primary air.
NO_x	Nitrogen oxides, i.e., the sum of nitric oxide (NO) and nitrogen dioxide (NO_2).
SG	Straight-grate pelletising process.
Thermal-NO	NO that is formed via the Zeldovich mechanism.
UV	Ultra-violet wavelengths in the range of 10–400 nm (UVA:315–400 nm; UVB: 280–315 nm; UVC: 10–280 nm).
Vol-N	Fuel-N that is released as a nitrogen-containing gas, e.g., HCN or NH_3, during volatilisation.
Vol-NO	NO that is formed from the oxidation of Vol-N.

1 Introduction

The growing concern over climate change and atmospheric pollution has focused global attention on energy intensive industries. The iron and steel industry, which is essential for modern Society given its roles in infrastructure, transportation, and manufacturing, is one of the largest contributors to global CO_2 and NO_x emissions due to its heavy reliance on fossil fuels. The production of iron and steel involves three key stages: raw material preparation (including pelletising and sintering); iron-making (via a blast furnace or direct reduction); and steel-making (utilising either a basic oxygen furnace or an electric arc furnace). Various technologies are being developed to enhance the sustainability of both iron-making and steel-making. In many of these advancements, pelletising is a crucial pre-requisite. While pelletising has a lower environmental impact than the other stages, it plays a vital role in reducing emissions across the entire iron and steel production chain.

For Sweden and Europe, pelletising processes are critical for producing high-quality iron ore pellets. Moreover, global demand for iron ore pellets is projected to grow until Year 2050, driven by the European steel industry's shift toward direct reduction (DR) processes. In this context, Sweden's iron ore operations play a pivotal role, with the European mining sector largely dominated by Swedish ore fields operated by LKAB. LKAB has set an ambitious target to render its entire iron ore production CO_2-neutral by Year 2045, primarily through electrification, with the integration of hydrogen into its processes. To replace fossil fuel use entirely with electrification, decades may be needed to overcome the economic and infrastructural challenges. Hydrogen-coal co-firing is an intermediate option to reduce the carbon footprint while proceeding in the direction of full decarbonisation. However, an efficient transition from coal to hydrogen firing in rotary kilns requires new knowledge of combustion stability, flame behaviours, and pollutant formation – especially NO_x formation – under co-firing conditions.

The effects of coal replacement should be considered in terms of the following aspects: 1) product chemistry and product properties; 2) process requirements and operational parameters; 3) full-scale measurements to characterise the full-scale process; 4) co-firing flame characteristics including flame properties, such as temperature, heat transfer, stability, and length; 5) NO_x formation during hydrogen coal co-firing; 6) flame measurement technologies for rotary kiln conditions, including optical measurements, cameras, International Flame Research Foundation (IFRF) probes, and gas analysers; and 7) hydrogen production and its economics. The present work develops the points 3, 4, 5, and 6.

1.1 Aims and scope

This thesis characterises flame properties and NO_x formation during hydrogen-coal co-firing under kiln conditions. The primary aim of this work is to replace 20%–30% of the total kiln heating with hydrogen. The secondary, long-term aim is full operation with hydrogen. The goal is to control flame behaviours to ensure efficient heat transfer and minimise NO_x emissions. The work focuses on technical-scale operations (i.e., pilot to full scale), with the emphasis on measurement techniques for flame characterisation that are applicable to various technical conditions. This research falls within the area of combustion science, focusing on experimental investigations that are supported by modelling.

This study adopts a step-wise approach to achieve the following key objectives:

- Step 1: Quantifying the impacts of co-firing gaseous and solid fuels on flame behaviours and NO_x emissions. This includes analysing the evolution of Fuel-NO and Thermal-NO formation, as well as assessing how the early release of volatile nitrogen species influences NO formation (**Paper I**).
- Step 2: Identifying and evaluating hydrogen injection strategies that minimise NO_x formation, while assessing the effects of such strategies on flame behaviours and characteristics (**Papers II** and **III**).
- Step 3 (ongoing): Assessing NO_x emissions and flame characteristics when co-firing hydrogen and coal in conditions closer to full-scale operation, scaling up the experimental set-ups to 580 kW.

In addition, measurement technologies are evaluated and developed throughout the burner development steps, with the following objectives:

- Evaluating conventional temperature and radiation measurements for high-temperature kiln conditions.
- Developing the *OH* chemiluminescence* method to determine the temperatures of hydrogen flames, and applying it to large pilot-scale and full-scale systems.

The findings from the first two development steps are presented in **Papers I–III**. Full-scale measurements complement the papers with comparisons and discussion of the results from **Papers I–III**. The third step, along with ongoing measurement method development, represents future work.

1.2 Content of the thesis

This thesis consists of an essay accompanied by the three published papers in the Appendix.

Chapter 2 presents the background to the work, starting with the importance of limiting climate change and the key factors that influence CO_2 emissions, using Kaya's identity as a framework. This chapter introduces the role of the iron and steel industry in sustainability and highlights the iron-ore pelletising process – how it depends on fossil fuels and its flame characteristics. **Chapter 2** also reviews the literature on hydrogen strategies, as well as the published NO_x formation and NO_x abatement strategies.

Chapter 3 covers the literature on co-firing of hydrogen and coal, and describes the theoretical background to high-temperature nitrogen chemistry, including the Zeldovich mechanism, the NNH route, the N_2O route, Prompt NO_x and the mechanisms for oxidation of fuel-bound nitrogen (Fuel-N). It also highlights the potential importance of these mechanisms in NO_x formation during hydrogen-coal co-firing and the limitations of scaling flames.

Chapter 4 outlines the methods used to characterise flame behaviour and NO_x formation during co-firing. It details the experimental and modelling techniques applied.

The experimental facilities, burner designs, and measurement devices applied in the work are presented in **Chapter 5**.

Chapters 6 and **7** summarise the results of **Papers I–III**, with complementary data from the full-scale campaigns. **Chapter 6** discusses the flame characteristics, focusing on the influences of fuel mixtures and burner configurations on ignition and flame stability and structure. **Chapter 7** discusses NO_x formation during hydrogen-coal co-firing. It highlights how fuel composition, burner design, and operating conditions influence NO_x formation.

Chapter 8 introduces the ongoing work of this thesis related to applying flame temperature measurement techniques using OH* chemiluminescence to technical-scale conditions. It outlines the main challenges associated with scaling up this method. In addition, the up-coming up-scaling and pilot-scale evaluations of the proposed techniques are introduced.

The thesis is concluded in **Chapter 9**.

2 Background

The negative impacts that modern civilisation has on ecosystems may be summarised according to the so-called “Triple Planetary Crisis”, which has three components: biodiversity loss, climate change, and pollution and waste. This crisis creates a complex web of challenges, making it difficult to work simultaneously and logically on both the system level and the underlying, precise solutions. In the transition to low-CO_2 systems, a system-wide perspective is essential to prevent counter-productive outcomes. If implemented in isolation, without progress in other areas of Society – such as values, ethics, economics, and politics – low-CO_2 systems could lead to more-complex challenges. This work is solely focused on technical aspects and aims to develop a technical solution to reduce the impact on climate change and to mitigate atmospheric pollution caused by nitrogen oxides in the iron-ore pelletising process. While it primarily aligns with UN sustainable development goal (SDG) 13 — "take urgent action to combat climate change and its impacts" — it also contributes to SDG 3 (good health and well-being), SDG 7 (affordable and clean energy), and SDG 11 (sustainable cities and communities), through its efforts to reduce nitrogen oxide emissions. This chapter will outline the context of climate change, its significance, and the key parameters that can be influenced. A brief overview of the iron and steel industry, including a description of its processes, and the importance of flames, will be provided. Finally, the transition to alternative fuels, with the emphasis on hydrogen, will be discussed.

2.1 Importance of limiting climate change

The connection between climate change and human activities is well established[1] and thoroughly documented in terms of their respective sources, by for example, the IPCC group, which updates, compiles and evaluates all the relevant scientific research on climate changes. Although the Earth experienced much higher temperatures with living ecosystems long before the human era, as shown by the reconstruction of temperatures for the eras spanning 600–80 million years[2], 80–0.02 million years ago[3], 7–0.02 years ago[4], 0.8 million years ago to present day[5], and 20,000 years ago to present day[6,7]. The threat of global warming relates not just to the temperature threshold that the system is reaching, but also to the un-precedented rate at which the global temperature is increasing[8–10]. Although mass extinctions have been attributed to various factors, the rate of change of the temperature in the Earth's climate has been identified as a key driver of most of the events[11–14]. Song et al.[10] have demonstrated a strong correlation between the rate of temperature change and the severity of mass extinctions. Based solely on this parameter, without

considering additional anthropogenic impacts on biodiversity, their projections indicate that the current rate of temperature increase could lead to a mass extinction event comparable to those observed during the Phanerozoic eon if global temperatures rise by 5.2°C by the end of this century. When considering geological time-scales, the human era is close to insignificant, and even more so the period with large-scale Societies, industrialisation and globalisation. Each climate is linked to a corresponding ecosystem, which must adapt or re-locate as the climate changes. Currently, 34% of the Earth's land[15] – equivalent to 46% of habitable land when excluding glaciers and barren areas – has already been converted from diverse ecosystems into agricultural land, predominantly for monoculture. In many instances, this intensive usage degrades the land to a near-desert condition over time. The remaining species struggle to adapt or re-locate quickly enough to keep pace with the current rate of global warming and globalisation. Although human intervention can offer some assistance, it is likely to be insufficient[16,17], leading to disruption of food chains and posing a serious threat to the survival of ecosystems. As human civilisations are closely connected to ecosystem stability, climate change increases existential risks for large-scale civilizations. The transition from hunter-gatherer Societies to agriculture-based ones, which was made possible by the relatively stable climate[18,19] of the past 10,000 years[20], has been crucial for the development of large-scale civilizations[21]. During rapid climate change, agriculture or sedentarisation in general is questionable, and therefore so are large-scale Societies. On a more immediate human time-scale, the current and growing risks include food insecurity[22,23], human health[24], economic decline[25–27], increasing inequality[28], rising insurance costs[29–31], earth system tipping points[32], ecosystem collapse[33], 6th mass extinction[10,34,35] and extreme weather events[36].

Estimations of the economic losses from climate change vary significantly depending on the methodologies and assumptions used in different models. However, as the levels of complexity of the models increase, their results tend to be increasingly pessimistic. This is due to the incorporation of additional phenomena, a shift from simple behaviours (linear) to non-linear ones, and the introduction of cascading effects, systemic interactions, and feed-back loops. For example, the network for greening the financial system (NGFS) models project that global losses will be 2–4-times higher by Year 2050 compared to earlier versions[37]. Despite their severe projections, these models still omit crucial factors, such as long-term climate adaptation, climate-induced migration, earth system tipping points, and nature-related risks. Thus, it seems likely that future versions of the model will give even more-pessimistic results.

Overall, the cost of climate inaction is highly likely to be much higher than the costs for transition or adaption in relation to climate change[27,38,39]. For only a 1°C warming, the macro-economic model of Bilal and co-workers predicts a GDP reduction of 12%[40]. The Emperor's new climate scenarios[41] propose a GDP loss of up to 63% by Year 2100 and an expected 50% loss between Years 2070 and 2090. The lowest GDP reduction is given by the dynamic integrated climate-economy (DICE) model developed by Nordhaus, which predicts that the climate impact will be 2% of GDP[42]. However, several critics have raised concerns regarding the over-simplification used in this model[43–45]. In the DICE model, climate change damages are assumed to increase in proportion to the square of the temperature rise, thus failing to capture non-linear phenomena, while real-world examples, such as the increasing frequencies of heatwaves, droughts, extreme weather events, and sea-level rises, clearly exhibit non-linear trends. Furthermore, the DICE model entirely overlooks critical aspects, such as earth system tipping points, cascading effects, and biodiversity loss, which can significantly amplify the GDP loss.

As a reminder, many of these models focus solely on climate impacts, whereas climate change is just one of several symptoms of the broader pressures that modern Society exerts on Earth's ecosystems. Nine planetary boundaries have been developed to assess the earth system and six of these have already been crossed[46–48].

2.2 Technical causes for climate change

While modelling the earth climate system is a large and complex task, some models have found good agreement[49–51] and have shown a clear deviation since the industrial revolution between natural drivers[1] and human drivers. This deviation can be largely attributed to changes in the concentrations of species emitted in large quantities by human activities, which, among other effects, alter the energy balance in the atmosphere[52,53].

The primary gas responsible for the greenhouse effect is first and foremost water vapour, which accounts for about half of the greenhouse effect[54]. This effect can be experienced under stable conditions, as when the sky during night-time is covered with clouds, the earth temperature remains higher than when the sky is clear. Although water vapour has a short life-time in the troposphere and, thus, is considered as zero CO_2-equivalents (CO_2-eq), it may affect the warming

[1] Some personal philosophical considerations could be included here. In my view, the term 'natural' is not well chosen, as humanity is not a separate entity from nature, but rather an integral part of it. This distinction is crucial for addressing certain aspects of the issue, psychological identification. A more-appropriate term would be 'drivers, modified or unmodified by humans.'

of the atmosphere. Water vapor is not a neutral element in the climate system. Human pollution tends to increase cloud formation (condensing water vapor) and hotter air (global warming) can hold more water vapor. Clouds, although water is in form of droplets, plays a complex function in heat transfer in earth system. Clouds entail a higher level of radiation of solar energy back into space, reducing the atmospheric temperature, while simultaneously trapping infra-red radiation emitted by the Earth's surface in the lower layers of the atmosphere, thereby limiting the planet's heat loss to space. Following water vapour, the dioxide of carbon (CO_2) contributes approximately 20%[54] of the greenhouse effect. Thereafter, methane (CH_4) (28 CO_2-eq), nitrous oxide (N_2O) (273 CO_2-eq), and hydrofluorocarbons (HFCs) (14,600 CO_2-eq) also playing significant roles. The respective contributions to current global warming from the main anthropogenic gases have been estimated at 1.11°C[55] for CO_2, 0.41°C[55] for methane, and 0.083°C[55] for nitrous oxide.

The main sources of anthropogenic methane[56,57] include the expansion of paddy-field rice cultivation, livestock production, and fossil fuel exploration and transport (referred to collectively as "fugitive emissions").

N_2O largely originates from agricultural activities[58], while HFCs were mainly used as substitutes for ozone-depleting substances until they were phased out thanks to the Montreal Protocol (ozone depletion).

Finally, CO_2, which is the most-abundant anthropogenic greenhouse gas, is largely produced from combustion of the fossil fuels used in the transport, energy, and industrial sectors, with a smaller contribution from land-use changes such as deforestation. Since the beginning of the industrial era, energy consumption has expanded rapidly. While the use of fossil fuels as a percentage of the total energy has decreased from close to 100% in Year 1900 to approximately 82% in Year 2023[59], this represents an absolute increase of 1,475% in total primary energy consumption during the same period[60]. To date, renewable energy sources have simply added more energy or limited the rate of increase of fossil fuel use; they have not yet replaced fossil fuels in absolute terms.

To reduce effectively the levels of CO_2, it is essential to understand that identifying its sources – primarily the combustion of fossil fuels – is not sufficient, as these sources are linked to various factors. These factors will be discussed in the following section using the Kaya identity.

2.3 Which societal parameter impacts CO_2 emissions? – The Kaya identity

Carbon dioxide emissions are influenced by numerous factors. Kaya's identity[61] helps identifying which variables can be controlled and changed quickly, and which needs more acceptance and

has effect in long term by breaking down the term CO_2 into various factors: population, economic activity, energy efficiency, and carbon intensity of energy production. Figure 1 shows the overall trends of each of the factors, then in this chapter, all factors will be discussed individually.

$$CO2 = Population \times \frac{Energy}{GDP} \times \frac{GDP}{Population} \times \frac{CO2}{Energy}$$

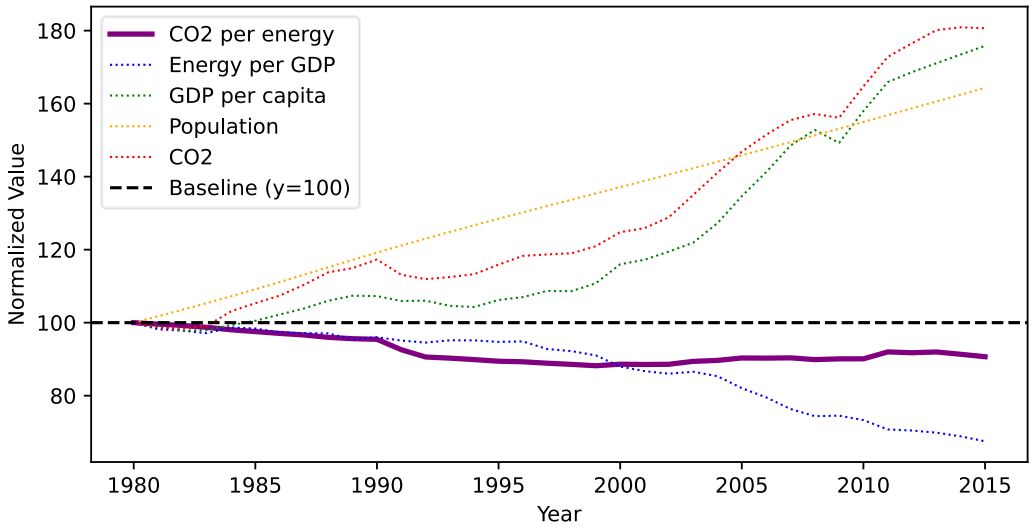

Figure 1. Kaya's equation, trend of the terms of the equation. Source of data[62–65]. This work focuses on decreasing the factor CO_2 per energy.

2.3.1 The term: *Population*

The global population has increased exponentially since the beginning of the industrial era from approximately 0.5 billion in 1600, 1.2 billion in 1850 and more than 8 billion today. It is a parameter that cannot be controlled in short term from a moralistic engineering perspective, but some actions are feasible as it is with education, equality/rights between men and woman in longer run. Nevertheless, it is important to recognize that age pyramid shape impacts country's economic health[66,67]. A rapid decline in population can negatively impact national stability and economic prosperity at different time scale. Moreover, Garrett et al[68] purpose that the population growth is rather a symptom than a driver of the exponential energy consumption and CO_2 emissions. Overall, population growth is influenced by numerous factors such as education, fertility, birth and death rates, and the human development index (HDI). Although accurately predicting the world population is challenging due to the vast number and uncertainty of variables. Projections up to the Year 2100 suggest a potential peak between 8 to 15 billion[69–71], with a

median estimate of 11 billion. Jørgen Randers, argued in his book[72] that global urbanisation could have a greater negative impact on human fertility than is typically accounted for in projections. He anticipates an earlier peak of global population in Year 2040, followed by a decline. Overall, there appears to be consensus that the human population will decrease in the long term, so a long-term decrease of this factor is foreseen in the Kaya identity.

2.3.2 The term: $\frac{Energy}{GDP}$

The $\frac{Energy}{GDP}$ term refers to the energy intensity of the economy. On a global scale, the economy can be viewed essentially as another unit for measuring energy, as nearly every economic activity is tied directly and/or indirectly to physical energy flows, with oil being the fundamental energy source because it is mainly used for the movement within Society (flow of materials/materiel/humans). The possibility of de-coupling to a sufficient extent economic growth from energy consumption at the global level has not yet been demonstrated[73–75], although a very weak de-coupling has been observed that may be attributed to efforts related to energy efficiency, and population movements to urban areas[76,77]. At the local level, several developed countries have transitioned from industrial production to the provision of services, resulting in economic expansion concomitant with a reduced energy demand. However, these countries still rely heavily on goods produced elsewhere, which may even increase their total emissions[73]. To conclude, in the long term, this factor appears to have a limited potential for further optimisation.

2.3.3 The term: $\frac{GDP}{Population}$

The term $\frac{GDP}{Population}$ represents the average economic activity per person. It typically increased as a country's develops and, overall, has increased considerably since the last century. GDP, which is the main macro-economic indicator used by the majority of countries, measures the size of the economy. While economic growth is often misinterpreted as a linear sign of societal progress, it is closely linked to increased environmental degradation. In general, a higher GDP is linked with greater environmental damage[78–80]. A hypothesised relationship between economic development and environmental degradation, known as the Environmental Kuznets Curve (EKC), suggests that environmental impact increases sharply during the early stages of economic growth. After reaching a turning point, further increases in GDP are expected to coincide with a decline in environmental damage. Despite its theoretical appeal, the EKC has so far failed to hold true at the global level. Moreover, it overlooks several types of environmental harm, such as biodiversity

loss, which do not follow the predicted pattern[81,82]. The factor $\frac{GDP}{Population}$ has enormous potential to decrease the pressures that civilisations impose on earth ecosystems, assuming that the dominant beliefs about it shift to a more-pragmatic understanding. Historically, the development of GDP dates back to the 1930s, when economist Simon Kuznets created the term to measure national economic performance during the Great Depression in the United States. At that time, the goal was to provide an accurate snapshot of production and consumption, to help policy-makers respond to the crisis. During World War II, GDP became essential for monitoring the production levels of war materials and resource allocation. However, Kuznets himself has warned against using GDP as an indicator of well-being, arguing that it reflects economic output rather than social welfare or human happiness[83]. Despite his caution, GDP was widely adopted after the war as the key measure of national success and it quickly became synonymous with societal health – a misconception that persists today. This oversimplification reduces the complexity of human well-being to a single economic figure, which leads to significant distortions. First, GDP is purely a quantitative approach that ignores whether it benefits Society or causes harm[84]. For example, expenses related to accidents, pollution or natural disasters increase GDP, even though they degrade people's quality of life. Second, GDP ignores ecological sustainability. GDP does not account for the depletion of natural resources or the environmental costs of economic growth, thus does not account for long term impact on itself. Daly (1996)[85] emphasises that the growing use of resources exceeds ecological limits, threatening future generations. In this perspective, at a certain size of economy, GDP becomes more a threat than some help. The GDP indicator tends to end in a destructive growth pattern due to its connection to physical flows. The obsession with infinite growth pushes governments to make short-term decisions aimed at boosting GDP, often at the expense of the environment and social cohesion[86]. Third, GDP fails to reflect social inequalities. A high GDP can conceal growing inequalities. Piketty (2014)[87] has shown that the distribution of wealth plays a crucial role in societal health. Research studies consistently show that economic growth over the last few decades has disproportionately benefitted the wealthiest individuals and corporate elites in Western countries, presenting a picture of higher GDP with lower social stability[88–92]. Finally, GDP does not consider psychological and social well-being. Studies such as those carried out by Diener and Seligman (2004)[93] have demonstrated that subjective well-being, social relationships, and life satisfaction are essential factors that GDP entirely overlooks. However, Lambert et al.[94] have found that access to high-quality energy – and consequently, a high GDP – is directly linked to human well-being. While the relationship between energy access and human well-being may hold true under some conditions, the study of

Lambert et al.[94] did not consider the impacts of cultural factors, such as values, cultural life goals, and levels of self-consciousness with regards to the relationship between energy consumption and quality of life. Therefore, the assumption that high energy consumption correlates with a high quality of life may only be valid within specific cultural contexts. The predominance of Western perspectives in most of the literature increases the risk of adopting absolute beliefs about well-being, when in reality, these conclusions may be culture-specific[95]. Moreover, research has shown that small-scale Societies can exhibit high levels of satisfaction with life despite low incomes[96]. Lastly, the method used to measure well-being can significantly influence the conclusions[97].

When it comes to alternative indicators and concepts to GDP, the human development index (HDI), ecological footprint or gross national happiness (GNH) or regenerative good growth[98] may be more-relevant indicators of societal progress and resilience[99]. Furthermore, in the broader perspective, economics is a study of human behaviors[100], which evolve in response to changing moral value systems. Shifts in moral values may have a strong potential to reduce the GDP per capita by emphasising well-being through reducing dependence on external factors[79,101–109]. This might be achieved with, for example, some political projects aimed at enhancing well-being and stability while reducing the size of the economy[78,110]. However, nowadays this philosophy faces challenges with strong contradictions against mainstream beliefs and a non-alignment with current economics laws[111] (with an example of the priorities adopted by most industries, i.e., price, performance, resilience, and then sustainability, as opposed to the priorities of the Degrowth Project, in which the planetary boundaries and social well-being are prioritised). To conclude, the future growth of the factor $\frac{\boldsymbol{GDP}}{\boldsymbol{Population}}$ is uncertain. On one hand, the dominant philosophy (Neoclassical economics) strongly emphasises economic growth, while on the other hand, emerging movements and discussions (related to, for example, degrowth), growing awareness of the limited measurement provided by GDP, the possibility that globalization has peaked (an essential condition for growth), and the finite nature of energy (for example, peak production of cheap conventional oil) and raw materials, along with rising extraction costs over time, complicate the outlook. The notion that economic growth can continue indefinitely within a finite world, as implied by the Solow–Swan model—foundational to neoclassical macroeconomic frameworks and developed by Robert Solow (Nobel Laureate) and Trevor Swan—is based on a set of assumptions that largely neglect fundamental principles of physics, particularly the qualitative properties and finite constraints of energy and material resources. Implicitly, the model assumes that all material and energy inputs can be substituted or mitigated through technological progress, an assumption that is fundamentally inconsistent with the

physical laws governing resource use, energy transformation, and entropy. Focusing on this factor to reduce CO_2 emissions by changing societal indicators and shifting cultures is seen to produce resilient and long-term effects, though it remains challenging and is often viewed as a utopian ideal today.

2.3.4 The term: $\frac{CO2}{Energy}$

Finally, this term describes the CO_2 intensity per unit of energy and is directly linked to the type of primary energy used. The global primary energy in Year 2023 is fuelled at around 82% by fossil fuels. The value of $\frac{CO2}{Energy}$ can be lowered significantly through a fuel-shifting strategy and/or employing carbon removal technologies and/or energy efficiency improvements. Applying this strategy to iron production, the term can be adapted to the following form:

$$\frac{CO2}{ton\ product} = \frac{CO2}{Energy} \times \frac{Energy}{ton\ product}$$

The term $\frac{Energy}{ton\ product}$ corresponds to the energy efficiency of the production (which will not be developed in this thesis). The term $\frac{CO2}{Energy}$ in this context refers to the CO_2 intensity of the energy utilised in the iron pelletising process. Given the economic and technical challenges associated with implementing carbon removal technologies, this study focuses on reducing the value of $\frac{CO2}{Energy}$ through fuel substitution strategies. Adopting the hypothesis that no improvement is implemented in the energy efficiency and carbon intensity of Swedish electricity, the decrease in CO_2 emissions achieved through fuel switching from coal to hydrogen may be in the magnitude of 83%. On average, the combustion of one MWh of sub-bituminous coal (the type of coal used in the current application) yields 346 $kgCO_2/MWh$. To give a sense of scale, taking in account an electrolysis efficiency in the order of 0.7 coupled with the carbon intensity of the electricity in Sweden given by Ember[112] and the Energy Institute[113], 1 MWh of hydrogen is emitting roughly 60 $kgCO_2/MWh$[114,115].

A word of caution is needed when it comes to the transition to large-scale, low-CO_2 Societies. Handling the climate problem is a necessity. However, if climate change is regarded mainly as an engineering problem rather than a cultural symptom of modern Societies, the overall damage may be even greater, creating additional problems. The shift to low-CO_2 energy sources such as electrification is increasing dramatically the need for materials[116,117]. As a result, there are increases in mining and the related pollution levels in ecosystems. Moreover, the Geological

Survey of Finland has released a report[116] in which the demand for materials contingent on the global phasing out of fossil fuels is presented. The simulation, which includes security of storage that lasts only 6 hours, already entails demands for lithium and cobalt than exceed the known resources. When this storage capacity is increased to 28 days, the demands are much higher than the known resources of copper, nickel, lithium, cobalt, graphite and vanadium. Furthermore, this study emphasises that these results reflect only a single generation of low-CO_2 infrastructure, including substantial amounts of energy produced by solar panels and wind turbines. Solar panels and wind turbine technologies have a typical lifespan of 20–30 years [118,119]. Although some materials can be recycled, the processes involved are often costly and energy-intensive, which in turn contributes to a sustained long-term demand for raw materials[120–123].

While the known resources will grow, the density of minerals that are currently exploited will decrease[116] and the costs of exploitation will increase. Discoveries of large ore bodies with high concentrations and easy access (high economic exploitation) are becoming rarer, adding one more challenge to tackling the triple planetary crisis concomitant with a growing economy.

2.4 Importance of decarbonising the iron and steel industry

Today's Society is built on high levels of energy and material inputs. A simplistic picture of the body of modern civilisation is that oil is the blood, steel is its skeleton, cement is its flesh, copper is its nervous system, and fertilisers are the stomach.

Overall, 98%[124] of the total iron production is used to produce steel, with only 2% used as a special product. Figure 2 shows the evolution of global mining production over the years, presented: (a) with mineral fuels; and (b) without mineral fuels. The extraction and processing of iron ore is the second-most-important mining production process in terms of weight after the mineral fuels, and accounts for 94%-wt of the metals mined (2019)[125]. The process from iron to steel is highly energy-intensive and accounts for around 8%[126] of the global energy demand, provided mainly in the form of coal (69%)[126], which generates around 7%[126] of global CO_2 emissions.

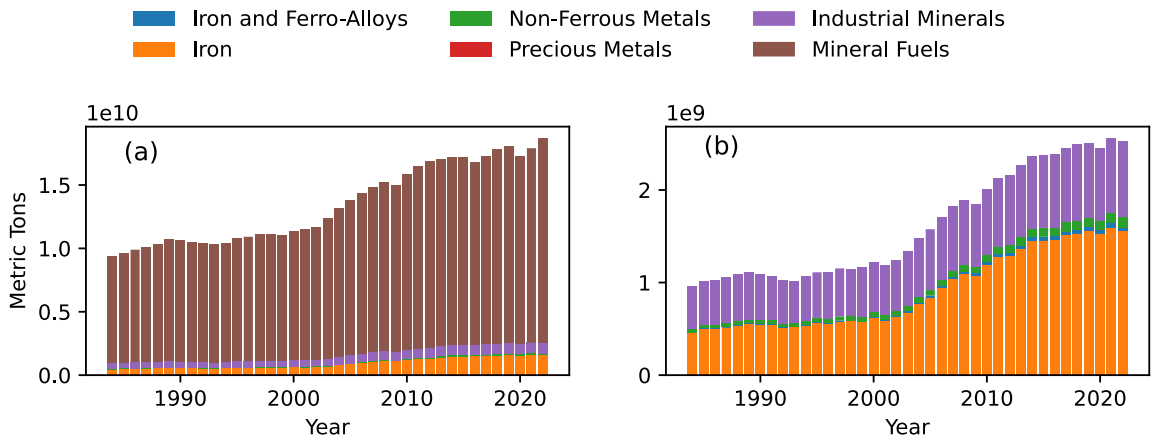

Figure 2. World mining production for the period of 1984–2022 by groups of minerals.[127,128] **Iron and Ferro-Alloy Metals:** Iron (97% of the Iron and Ferro-Alloy Metals), Chromium, Cobalt, Manganese, Molybdenum, Nickel, Niobium, Tantalum, Titanium, Tungsten, Vanadium**; Non-Ferrous Metals:** Aluminium, Antimony, Arsenic, Bauxite, Beryllium, Bismuth, Cadmium, Copper, Gallium, Germanium, Indium, Lead, Lithium, Mercury, Rare Earth Minerals, Rhenium, Selenium, Tellurium, Tin, Zinc**; Precious Metals:** Gold, Platinum-Group Metals (Palladium, Platinum, Rhodium), Silver; **Industrial Minerals:** Asbestos, Baryte, Bentonite, Boron Minerals, Diamond (Gem/Industrial), Diatomite, Feldspar, Fluorspar, Graphite, Gypsum and Anhydrite, Kaolin (China-Clay), Magnesite, Perlite, Phosphate Rock (incl. Guano), Potash, Salt, Sulphur, Talc (incl. Steatite and Pyrophyllite), Vermiculite, Zircon; and **Mineral Fuels:** Steam Coal (incl. Anthracite and Sub-Bituminous Coal), Coking Coal, Lignite, Natural Gas, Petroleum (incl. Natural Gas Liquids), Oil Sands, Oil Shales, Uranium.

The iron and steel industry involves a sequence of processes that transform raw materials into final steel products. It begins with the extraction of iron ore from the earth, through either open-pit or underground mining, after which the ore is transported to processing plants for further treatment. The extracted ore is then crushed and grounded into fine particles, which then undergo a concentrating process using methods such as magnetic separation, flotation, and gravity separation. These processes remove impurities and increase the iron content, and producing a concentrated ore.

Thereafter, the iron ore is transformed into a form (lump, sinter or pellets) that is usable for the iron-making. Iron lumps, which represent the simplest form, thus need little processing, are in decline owing to the depletion of the world's high-grade iron ore resources and the fact that iron of higher grade is produced with pellets. Pelletising of iron ore involves mixing the concentrated ore with binders and forming small pellets, which are hardened through thermal treatment. Sintering, on the other hand, involves heating fine iron ore particles until they bond into larger masses, called sinter, often with the addition of fluxes such as limestone to improve the quality of the product. Although sintering is currently used more commonly, it has a significantly worse environmental impact and a higher energy consumption compared to pelletising[129,130]. Given the decline in demand for both lump and sinter and the increased need for steel, the demand for pellets is expected to increase[131].

The prepared raw materials are then converted into iron in the iron-making stage. This is achieved either in a blast furnace (BF) (70% of iron-making[132,133]), or through direct reduction (DR). In the BF process, iron ore in the form of pellets or sinter, along with coke and limestone, is heated with carbon monoxide to reduce the iron ore and produce molten iron, also known as pig iron. Alternatively, the DR method reduces the iron ore to solid iron called direct reduced iron DRI, using reducing gases without melting the ore. This method is favoured because of its lower carbon intensity and is considered more environmentally sustainable than the BF process.

The final stage is steel-making, whereby iron is transformed into steel. This is achieved using the basic oxygen furnace (BOF) or electric arc furnace (EAF) methods. In the BOF process, molten pig iron from the BF is transferred to a furnace where oxygen is blown through it, reducing the carbon content so as to produce molten steel. This method is highly efficient for large-scale production. The EAF method, on the other hand, melts scrap steel or DRI using electrical energy, offering environmental advantages and the flexibility to use recycled materials. Furthermore, it produces various grades of steel with fewer emissions, making it a key technology for sustainable steel production.

2.5 CO_2 partitioning of the iron and steel industry

When discussing CO_2 emissions, it is important to specify the types of emissions that are being addressed. One widely used methodology is the greenhouse gas protocol, which defines emissions in terms of three scopes. Scope 1 covers direct emissions from sources owned or controlled by the entity, such as fuel combustion on-site, company vehicles, and industrial processes. Scope 2 accounts for indirect emissions from purchased energy, including electricity, steam, heating, and cooling. Scope 3 encompasses other indirect emissions across the value chain, such as those from the supply chain (purchased goods, services, waste, and transportation), business travel, employee commuting, and the use or disposal of sold products. Scope 1 has the highest level of control, while Scope 3 has the lowest level of control and can be challenging to measure. Defining Scope 3 emissions can also be unclear due to their broad implications. For example, large-scale Societies would not exist without the iron and steel industry. Thus, in that case, with extremely broad boundaries taken, all the modern emissions may be integrated in the Scope 3 of the iron and steel industry. This applies to several fundamental industries, such as mining and energy extraction/production companies. Focusing on Scope 1 emissions offers the greatest potential for change, as it is the most-controllable scope. When considering the iron and steel industry as a single entity, Scope 1 emissions are largely dominated by the processes

themselves, making them important for sustainability. The share of CO_2 emissions for the pellets-based steel making route is 8-10% for the raw material preparation (made by pelletising process), 60-70% for the iron-making process, and 20%–30% from the steel-making process.

Although pelletising processes contribute a relatively small percentage to the overall iron and steel production chain, they remain a crucial step for achieving decarbonisation across the entire chain. Several solutions are under development for iron-making, and most of the projects have entered the stage of construction or testing, among them the ULCOS[134] (Ultra-Low CO_2 steel-making), SALCOS[135] (Salzgitter Low CO_2 Steel-making), HYBRIT (Hydrogen Breakthrough Iron-making Technology)[136], and MIDREX[137] projects in Europe, and COURSE50[138] in Japan. Some other technologies and projects that aim to produce iron directly based on fines, thereby side-stepping the pelletising plant, include flash iron-making, CIRCORED[139], and HYFOR (Hydrogen-based Fine-Ore Reduction)[140]. Table 1 summarises the technologies, fuels used, and the inputs/outputs of the processes. Most of these innovative iron-making processes rely on iron ore pellets as the primary feedstock. Thus, the pelletising plant is foreseen as an important process in the future, playing a crucial role in enabling decarbonisation of the entire iron and steel value chain.

Table 1. Features of the low-CO_2 iron-making projects.

Project/Process	**Input**	**Fuel/Energy Source**
HYBRIT (Sweden)	Iron ore pellets	Green hydrogen (H_2)
COURSE50 (Japan)	Pellets or lump ore + coke	Hydrogen injection + coke
H2 Green Steel (Sweden)	Iron ore pellets	Green hydrogen
SALCOS (Germany)	Iron ore pellets	Initial blend with natural gas, later 100% H_2
ULCOS (Europe) – Ultra-Low CO_2 Steel-making	Iron ore	Carbon capture and storage
MIDREX (Global)	Iron ore pellets	Natural gas (NG) or H_2
CIRCORED (Trinidad)	Iron ore fines (no pelletising needed)	Natural gas (can transition to H_2)

HYFOR (Austria)	Iron ore fines (no pelletising needed)	Green hydrogen (H_2)
Boston Metal (USA)	Iron ore concentrate	Renewable electricity (Molten Oxide Electrolysis)
GrInHy (Germany)	Iron ore pellets	Green hydrogen (via high-temperature electrolysis)
SUSTEEL (South Korea)	Iron ore pellets	Hydrogen + Carbon Capture and Storage
Emirates Steel (UAE)	Iron ore pellets	Green hydrogen + natural gas

2.6 H_2 strategy

Since hydrogen is considered to the most-suitable fuel for reducing CO_2 emissions in iron-making, the development of an extensive hydrogen production infrastructure is expected. In terms of energy consumption, the iron ore pelletising process represents a relatively small share compared to iron-making. Therefore, if a large-scale hydrogen infrastructure is already established for iron-making, utilising a portion of it for pelletising plants would be both feasible and practical.

Electrification is thus seen as the path to be taken for low-CO_2 Societies[98]. Nevertheless, switching from fossil fuels to electrification entails significant economic challenges due to the energy return on investment (EROI) of the primary energy source, as seen, for example, in the case of Belgium[141]. For electrification to contribute to a low-CO_2 system, electricity must be generated from renewable energy sources or nuclear power. However, fossil fuels historically have a much higher EROI than most renewables, with the exception of hydro-electric power[142,143].

Hydro-electricity generation on rivers, while efficient, is limited by geographical and environmental factors: it requires sufficient rainfall levels, an elevation drop, and large initial investments. It also disrupts ecosystems, displaces populations, and faces increasing risks from climate change, such as droughts and changing rainfall patterns, which may reduce its output and increase the risk of dam collapse.

On a positive note, while energy production from fossil fuels has historically been shown to have a significantly higher EROI than renewable energy production, the future evolution is a topic of

debate and may change over time. First, a comparison of all the EROI values at the same unit for the final energy form of electricity shows that the EROI of fossil fuels is much lower than previously estimated, bringing it closer to that of renewable energy[144] or even lower[143].

In the iron and steel industry, the required final energy form is heat, in which case fossil fuels retain an advantage in the medium-term future. However, the extraction of fossil fuels is becoming increasingly costly and energy-intensive due to difficult access to reserves and declining resource quality, which necessitates more processing, as in the example of natural gas[145]. In contrast, renewables may improve their EROI thanks to technological advancements, mass production and policy supports[146,147].

Thus, while the transition to a renewable energy system may initially face economic hurdles, in the longer run this transition to a low-CO_2 Society could eventually make it economically competitive. Court et al.[142] have reported that the EROI peaks for oil and natural gas have already passed, while the peak for the coal is awaited between Year 2025 and Year 2045. This makes coal far too attractive in the absence of policy initiatives to curb climate change impacts.

Transitioning from the discussion of primary energy sources, which are the raw forms of energy, to final energy, which is the energy ready for consumption by end-users – specifically in the case of iron ore pelletising – presents two options for retrofitting current fossil fuel burners with electrification: direct and indirect electrification. Direct electrification is achieved using plasma burners, while indirect electrification involves the use of hydrogen, which requires an intermediate step to convert water into hydrogen using electricity.

Even though plasma technology shows some potential, several challenges remain. This technology is not yet sufficiently mature to implement, and the radiation levels from the plasma are low when using air. This issue can be mitigated by using alternative gases, such as CO_2, although this entails additional operational costs.

The plasma technology may offer lower infrastructure costs compared to hydrogen. However, hydrogen production has the added benefit of generating O_2, which can be valuable in the iron ore pelletising process as O_2-enriched air can be used to enhance pellet oxidation (in case of magnetite pellets). Furthermore, as previously discussed, a hydrogen production infrastructure is likely to be developed for iron-making. Since pelletising requires significantly less energy than iron-making, integrating hydrogen production for pelletising with iron-making could be more practical and cost-effective. In addition, the hydrogen burner technology is simpler and is

currently more robust. As a result, hydrogen has attracted considerable interest for use in iron pelletising plants and serves as the transitional fuel explored in this thesis.

It is worth noting that reducing CO_2 at the source, rather than treating exhaust gases with carbon capture, is the preferred route. The fuel switching strategy is favoured over the carbon capture technology due to the composition and volume of the exhaust gases. The exhaust gases from pelletising plants are large in volume, with a CO_2 concentration of only 2%–3%. The overall process operates at a high lambda of around 5, resulting in an O_2 concentration of 16%–17% at the outlet. The combination of large volume of exhaust gas and low CO_2 concentration makes the carbon capture technology highly expensive, inefficient, and difficult to implement on-site due to the large scale. Other compensatory mechanisms, such as the enhancement of forest carbon sequestration (boreal forest in this case), appear to be complex and highly debated making it risky as a base strategy for achieving CO_2 neutrality[148,149]. This limitation is exemplified by the decrease of the carbon sink in boreal forests[150]. Several key factors contribute to this issue, including deforestation driven by the forestry industry, direct climate change impacts (such as increased drought and heat waves), and indirect effects related to climate change and biodiversity changes (disease outbreaks)[151–154].

Finally, a last word of caution is needed. While hydrogen is seen as a promising technological solution to cut significantly the CO_2 emissions of the iron and steel industry[155], the hydrogen strategy risks limiting its own potential for positive climate impact as the technology is scaled up. The first issue is ensuring that electricity for hydrogen production comes from low-CO_2 sources, and the second issue is addressing the increasing risk of hydrogen leakage into the troposphere. Significant leakage of hydrogen into the troposphere could undermine the climate benefits of the hydrogen strategy by reacting with existing hydroxyl radicals (OH)[156]. This reaction reduces the availability of OH, which is the primary radical responsible for oxidising methane[157]. As a result, methane's atmospheric life-time could be indirectly extended, amplifying its warming effect.

2.7 Pelletising process

Two main types of pellets are produced with iron ore through pelletising processes: Direct Reduction (DR) pellets for shaft furnaces; and Blast Furnace (BF) pellets for blast furnaces. Iron ore pellet production consists of four main stages: extracting the ore, sorting, concentrating, and pelletising.

Extracting the ore from iron body in an open pit or an underground mine is the first step in the making of iron ore pellets. Iron ore naturally occurs in various mineral forms, including magnetite

(Fe_3O_4), hematite (Fe_2O_3), limonite ($FeO(OH)\cdot nH_2O$), goethite (α-$Fe^{3+}O(OH)$), siderite ($FeCO_3$), and pyrite (FeS_2). The primary minerals used in global pellet production are magnetite[158], which has a high iron content of 72.4%, and hematite, which contains 69.9% iron. At the extraction stage, iron ore is in form of large rocks (approximately 10 cm in diameter) that are mixed with other minerals.

In the sorting stage, non-iron-bearing rocks are separated from the iron ore by crushing and magnetic separation, increasing the iron content from approximately 45% to around 62%. At this stage, the iron ore is in form of small rocks.

The concentrating stage further increases the iron content and removes impurities. The ore is finely ground and mixed with water to form a slurry. This slurry goes further through magnetic separation that increases the iron content to about 72%, while unwanted substances are removed chemically through flotation. At this stage, iron ore cannot be used directly in the traditional iron-making process without the final stage of pelletising.

The concentrate must be agglomerated into uniformly sized pellets, typically between 9 and 16 mm in diameter, to ensure optimal iron-making performance. To facilitate this agglomeration, binders (mainly bentonite and organic binders, though others may also be used) are added[159–162]. As discussed previously, these binders help the pellets achieve sufficient strength before the induration process, lower the induration temperature requirement, and improve the mechanical strength after induration. Flux agents (such as limestone and dolomite) are also added, to help clean the impurities in the BF through slag formation. The balling process is carried out using either discs or drums, with pellet sizing controlled through sieving. Once properly sized, the pellets enter the induration phase, where they are hardened to achieve the required mechanical strength for iron-making and transport.

After processing in the pelletising plant, the pellets are predominantly in the form of hematite. One advantage of processing magnetite rather than hematite is that the oxidation of magnetite to hematite is an exothermic reaction, releasing 482.4 kJ/mol of Fe_3O_4. It has been estimated that magnetite requires approximately 633–844 MJ/t whereas hematite requires 1,055–1,266 MJ/t[129] in the pelletising plants. When working with hematite ores, this heat release does not occur, requiring an external heat source, which increase energy consumption and carbon emissions. To address this, hematite is agglomerated with a controlled amount of carbon (0.7–2.0% by weight[129,163,164]), which burns during induration, providing the necessary heat. Mixing of hematite and magnetite pellets is also possible and has been shown to yield a good-quality product[165].

The sorting and concentrating stages are cold processes with minimal atmospheric emissions. Nearly all the emissions in this part of the production chain come from the pelletising process that hardens the pellets through the so-called induration, which combusts fossil fuels.

While shaft furnaces[166] were used initially, straight-grate (SG) systems currently dominate induration processes[158] followed by grate-rotary kiln (GK) systems[158]. Although the GK process was developed after 1960 in the iron-pelletising sector, this technology is much older and was introduced around 1880 for the cement industry[167,168].

Figure 3 describes typical SG and GK processes. The SG and GK processes for pellet production consist of four sequential steps: drying, pre-heating, induration, and cooling. In the SG process, all four steps are carried out on a single continuous grate. In contrast, the GK process divides these steps across three distinct units: a grate for drying and pre-heating, a rotary kiln for induration, and an annular cooler for the final cooling step.

Before entering the SG or GK process, the pellets contain 7%–9%-wt water and are called ‘green pellets’ at this stage. In the drying step, the pellets are completely dried at controlled heating rates to avoid cracking, with drier temperatures in the range of 150°–350°C. This process is divided into two zones: an up-draught drying zone, where air passes through the pellet bed from bottom to top; and a down-draught drying zone, where air flows from the top downwards. Both zones are essential for ensuring that the pellets are fully dried.

Next is the pre-heating zone, where the temperature is raised further, reaching between 500°C and 1,100°C, to initiate the development of the mechanical strength of the pellets. For rotary kilns, it is particularly important that the pellets attain sufficient strength during this stage to withstand the transition from the grate to the kiln without breaking.

The induration zone, which happens in the rotary kiln, follows, where pellets are exposed to the highest temperatures, ranging from 1,150°C to 1,250°C. This stage is critical for achieving the final mechanical properties of the pellets. The flame in this zone plays a crucial role in maintaining the appropriate temperature and heating rate to ensure proper induration.

Finally, in the cooling zone, the pellets are cooled to approximately 80°C, making them suitable for transport or storage. During this stage, heat is recovered and re-distributed within the grate zones or the kiln's secondary airflow, optimising energy efficiency and supporting the overall thermal distribution of the process.

Both SG and GK plants can produce either BF-pellets or DR-pellets[169]. Since BF operations are dominating iron-making processes, the BF pellets pre-dominate in both the SG and GK. However,

due to better environmental results being obtained for iron-making in shaft furnaces, the use of DR pellets is expected to increase in the future[170,171]. This is crucial when starting a transition for a process that lasts for decades, in assuring that the product will still be needed.

While the four steps are similar, fundamental differences appear between the SG and GK kilns. Airflow distribution in a grate kiln is managed through parallel pipes, while in a straight grate, the airflow is distributed internally. The pellet bed in the SG kiln is higher, typically 50–70 cm, and remains stationary. In contrast, the pellet bed in a grate kiln is usually 15–25 cm high and moves through the process with several transitions. The pellets exit from the grate to the kiln, tumble continuously within the rotating kiln, and then exit via a chute from the kiln to the cooler. These transitions demand specific pellet properties, especially between the grate and the kiln, where not all pellets are fully oxidised, to ensure that they maintain integrity during handling. Grate kilns generally consume more energy due to higher radiation losses from the rotary kiln[169] and the potential for additional energy loss through the parallel pipes used for heated air distribution. In terms of burners and flames, the induration process in an SG relies on several small burners, creating multiple small flames, whereas a GK operates with a single burner and flame driving the entire process. GKs generally produce higher-quality products due to the continuous tumbling in the rotary kiln. The consistency in quality is higher for a GK process than for an SG process, as demonstrated by the temperature profiles of the top and bottom layers of the pellets in Figure 3. While maintenance costs for GKs tend to be higher, this difference tends to decrease as the size of the plant increases[169]. Heat transfer from the flames to the bed in an SG is primarily achieved through convection[172–175], while in a rotary kiln, radiation is the dominant form of heat transfer[176–179]. When it comes to fuels, SGs, due to their several shorter flames, are more suitable for oil and gas fuels. On the other hand, rotary kilns, with their long and consistent temperature profile, are suitable for solid fuels, though some rotary kilns also use oil or natural gas.

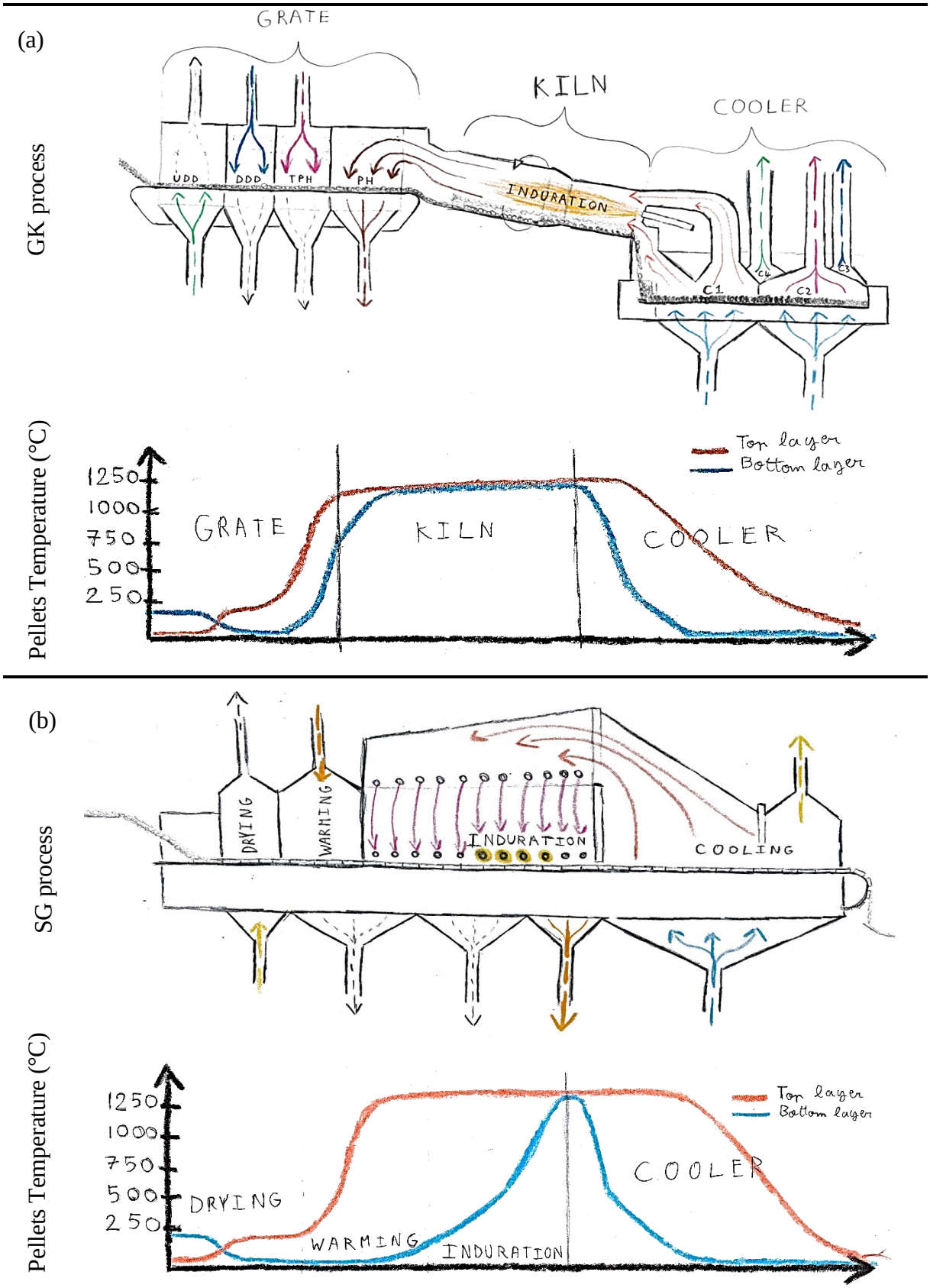

Figure 3. (a) The GK process consists of UDD, DDD, TPH, and PH zones, followed by treatment in a rotary kiln (induration zone) and an annular cooler with four decreasing temperature zones: C1, C2, C3, and C4. (b) In a single machine, the SG process integrates multiple stages, including the drying zone, warming zone, induration, and cooling.

Transitioning from fossil fuels to hydrogen appears to be less challenging for the SG process than for the rotary kiln process. This is because the SG relies on multiple shorter flames and convective heat transfer, which align well with hydrogen's combustion characteristics. However, an important consideration is that hydrogen flames are significantly less-radiative than those of carbon-based fuels. Moreover, hydrogen combustion is expected to produce higher flame temperatures than combustion of the fuels currently used in rotary kilns. The combination of higher gas temperatures, particularly at the centre of the gas flow in the kiln during the initial phase, and lower radiative heat transfer may actually help to create a more-uniform temperature profile along the kiln's wall, as compared with traditional coal or oil[176]. However, in the case of co-firing hydrogen with coal, this effect could pose challenges. The presence of H_2 may increase the initial temperature of the coal particles, enhancing their combustion rate and radiation output, which could result in a shorter coal flame with high local intensity at the beginning of the kiln. Therefore, studying flame behaviours in hydrogen-coal co-firing within the GK system is essential to understand and mitigate potential operational issues.

2.8 Importance of the flame characteristics for the grate-kiln pelletising process

The function of the flame is to generate the mechanical properties of the pellets so as to ensure both transportation and optimal running conditions for the BF or shaft furnace through controlling the temperature distribution within the process. As discussed previously, co-firing hydrogen and coal may change significantly the flame properties, as compared with 100% coal-firing. The flame characteristics are of great concern, as they influence both the stability of the process and the quality of the product.

2.8.1 Impacts of the flame characteristics and fuel on the stability of the process

Two important parameters that are influenced by the flame characteristics and fuel type are: (i) the refractory material in the kiln and (ii) the slag build-up.

The interior of the kiln is lined with a refractory material that withstands high temperatures, thereby limiting heat loss and protecting the steel shell. The refractory material is sensitive to several factors, such as cycling (heating and cooling sequence of the kiln—executed without a production load), temperature profile (hot spots, temperature gradient), mechanical stress (alignment of the kiln on its rolling wheels), chemical reactions and wearing that occurs between the product and refractory material[180]. A change of fuel mixture may affect the temperature profile, the locations of hot spots, and the heating-up and cooling-down processes of the kiln. The

main risk is that uncontrolled, significant changes in the flame conditions may cause cracking and/or spalling of the refractory material. To achieve the Year 2030 goal, the fuel currently used for heating and cooling will remain the same, i.e., heavy oil (EO5). However, the temperature profile in the kiln will likely change in line with production load. The heating and cooling processes will become more important to study in the subsequent decarbonisation stages, when hydrogen or other alternatives fuels will be used under this particular operational condition of the kiln.

The second parameter that may disturb production is "slag build-up", which refers to the accumulation and formation of slag on the interior surfaces of the kiln. Slag is composed mainly of impurities from the ore, fluxes (such as limestone), and ash from the fuel. These materials meld at high temperatures to form a liquid or semi-liquid slag that adheres to the kiln's lining and other surfaces. The main elements from the fuel responsible for slag formation originate from the fuel-ash content: Illite, Pyrite, Calcite, Quartzite, Siderite and organically bound Na, K, and Ca. A small quantity of slag can help to maintain the refractory material in situ, whereas a large quantity limits production and cleaning the kiln to remove the slag becomes necessary.

2.8.2 Impacts of the flame on pellet quality

BF and DR pellets have few quality indicators in common; they each have specific indicators designed to meet the requirements of their respective ironmaking processes. DR pellets generally have a higher iron content (67% or more) than BF pellets, which typically contain 62%–65% iron[181,182]. This higher iron content is essential for the DR process, where the ore is reduced at lower temperatures using reducing gases. In addition, DR pellets have higher porosity[181], which enhances gas permeability, a critical factor for efficient gas-solid reactions that reduce iron ore to metallic iron in DR processes. Producing DR pellets in pelletising plants requires higher energy levels for the following reasons:

- **Higher Iron Content and Lower Binder Levels:** Since DR pellets have a higher iron content to improve metallisation rate during reduction, they contain less binder material compared to BF pellets. This imbalance requires higher induration temperatures to achieve the required mechanical strength, increasing the overall energy consumption.
- **Absence of Liquid-Phase Sintering:** BF pellets contain higher levels of silica and alumina, which promote the formation of a liquid phase during induration. This liquid phase acts as a binder, filling the gaps between particles and improving pellet strength at lower temperatures.

- **Fluxing Agents:** BF pellets often include fluxing agents such as limestone and dolomite, which help form slag in BFs to capture impurities. DR pellets are less-fluxed, maintaining their chemical purity to enhance reduction efficiency in DR processes.

In a rotary kiln, the flame characteristics (temperature distribution, radiation, flame length, and intensity) play crucial roles in determining pellet quality. Several key quality parameters for pellets are directly influenced by the conditions within the kiln during the induration process. To elucidate the influences of the flame characteristics on pellets quality, two cases are presented:

Case 1: The flame presents a smooth heat transfer along the kiln. The pellets are experiencing a consistent, high-temperature zone of around 1200°C for a period of at least 20 minutes. The pellets oxidise fully to hematite.

Case 2: The fuel used transfers most of the heat at the beginning of the kiln, creating a peak temperature zone at the beginning of the kiln and a lower temperature zone at the end of the kiln. The pellets will remain at a temperature of <1,100°C for most of the kiln, and will thereafter enter a zone with temperature >1,400°C at the end of the kiln. In this case, due to the short time spent at temperatures in the range of 1,200°–1,300°C following by a very-high-temperature zone, the pellets may sinter only on the shell, creating a strong shell, with the remaining magnetite at the core.

The first risk that arises between Cases 1 and 2 is that in Case 2, internal cracking may occur. Moreover, the following quality indicators may be significantly impacted (Figure 4 illustrates where in the process these quality parameters become significant):

Tumbling Strength index (TI - ISO 3271) (BF and DR pellets) which refers to the pellet's resistance to disintegration during handling and transportation. This is critical when the pellets drop from the grate to the kiln and from the kiln to the cooler during the process. It is equally important in the logistics chain, wherein pellets must endure repeated transfers between containers (e.g., trains, silos, and the iron-making process) without breaking apart.

Cold Compression Strength (CCS - ISO 4700) (BF and DR pellets) ensures that the pellets maintain their structural integrity when subjected to pressure from the overlying layers during storage and transportation. This measures the resistance of the pellets to breakage under compressive loads. A high crushing strength indicates good mechanical stability during handling and transportation. Several studies have reported that an induration time of approximately 20 minutes for temperatures in the range of 1,200°–1,250°C is optimal to achieve the highest CCS value[158,166,183]. The CCS value appears to be specific to each pellet production chain. In some

cases, the DR pellets have higher CCS values than the BF pellets, while in other cases, the BF pellets have similar or higher CCS values[184,185].

Low-Temperature Disintegration (LTD - ISO 13930) (BF pellets only) indicates the pellet's ability to resist cracking or fragmentation at around 500°C. This is vital to avoid early degradation during the initial stages of reduction.

Reduction Under Load (RUL - ISO 7992) (BF pellets only) ensures that pellets remain structurally intact when reduction starts under the high pressure imposed by multiple pellet and coke layers at high temperatures.

Reduction Disintegration and Metallisation (RDM - ISO 11257) (BF pellets only) assess both the pellets tendency to disintegrate during the reduction process and the percentage of final metallic iron produced. Maintaining a high level of metallisation while minimising disintegration is vital for ensuring process performance and product quality.

Linder test – Reduction Disintegration index (RDI - ISO 11257) (DR pellets only) measure the degradation and reducibility at low temperature apply for DRI conditions.

In terms of tumbling strength, CCS, LTD, RUL, and RDM/I, Case 1 demonstrates significantly higher quality than Case 2. In Case 2, the presence of a magnetite core and a hard shell causes the pellets to be more fragile, which means that they crack and break under weaker stresses. In contrast, the pellets produced in Case 1 exhibit superior durability and structural integrity. Moreover, besides the mechanical properties, two other quality parameters may be impacted: the free-swelling index; and reducibility.

Free-swelling index (FSI - ISO 4698) (BF pellets only) measures how much the pellets expand during the reduction process. Excessive swelling (>20%) increases the risk of structural failure and disintegration. Compared to magnetite, hematite exhibits minimal swelling under reduction conditions, contributing to a smoother operation. In Case 1, the pellets will not swell as much as in Case 2, avoiding an increase in pressure during the iron-making process, and thereby limiting the risks of pellet disintegration and operational disruption.

Reducibility index (RI) (BF pellets only) measures how easily and quickly the pellets are reduced from iron oxide to metallic iron. Higher reducibility means faster reduction, which enhances process efficiency. Both BF and DR pellets use this quality criterion; however, the tests differ depending on the type of pellets, with ISO 4695 applied for BF pellets and ISO 11258 for DR pellets. Hematite shows better reducibility than magnetite, so if the pellets are not oxidised fully to hematite, in Case 2 for example, the time to reduction in the iron-making process becomes

longer. As a consequence, the iron-making will consume more energy. Moreover, the porosity of the pellets is very important with respect to facilitating the reduction process: if the pellets enter a too-high-temperature zone, the porosity level will decrease. A balance needs to be achieved between high cold compression strength and high porosity. A higher temperature of induration leads to lower porosity[166,183,186,187].

Finally, one parameter specific to DR pellets is impacted by induration temperature profile.

Sticking index (ISO 11256) (for DR pellets only) measures the tendency of DR pellets to adhere to one another to prevent the pellets from sticking together inside the DRI furnace. The sticking index is impacted by several parameters such are porosity, oxidation state, time at high temperature during induration, and mechanical strength of the pellets.

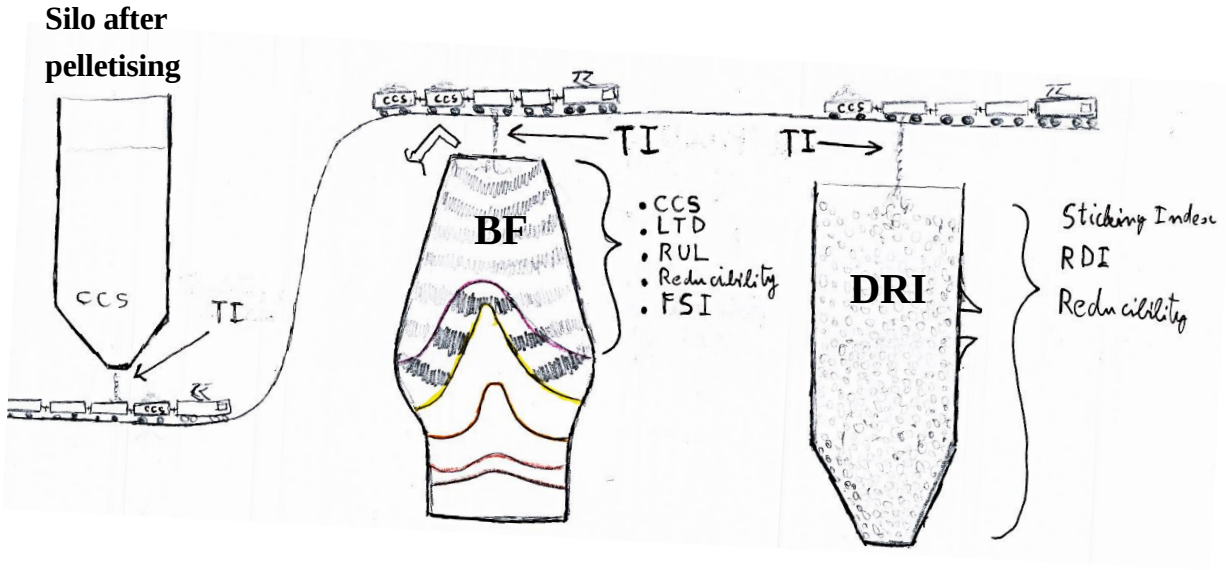

Figure 4. Pellet quality and its importance. CCS: cold compression strength; TI: tumbling index; LTD: low temperature disintegration; RUL: reduction under load; FSI: free-swelling index; RDI: reduction disintegration index.

2.9 Work extendable to other applications

Iron ore processing represents a less-significant application of rotary kilns. Cement production, lime production, various chemical processes (including the production of alumina, titanium dioxide, and other chemicals) and metallurgical processes (e.g., the production of ferro-alloys) also utilise rotary kilns, contributing to CO_2 emissions. Cement and lime production plants are the dominant users of the rotary kiln technology. According to Circle Economy, the world consumes 100.6 billion metric tonnes of materials annually. Of this total, the 3.2 billion metric tonnes of metals produced in Year 2019 would account for just 3% of our overall material consumption. In fact, the world's annual production of cement alone is around 4.1 billion metric tonnes, dwarfing total metal production.

The key differences between iron ore rotary kilns and cement rotary kilns lies in the temperature requirements, oxygen demand, and secondary air temperature. Iron ore rotary kiln required a bed temperature typically in the range of 1,150°–1,250°C, whereas cement production requires higher temperatures of approximately 1,400°–1,500°C. The O_2 concentration in the exhaust gases is in the range of 1%–4% in cement kilns, whereas it rises to 15%–17% in iron ore rotary kilns. Finally, the temperature of the secondary air flow in cement rotary kilns is typically in the range of 800°–1,000°C[188,189], while in iron ore rotary kilns it is higher, in the range of 1,000°–1,150°C.

Quantifying the Responsibility. While it is challenging to attribute a precise percentage of global CO_2 emissions directly to rotary kilns, estimates can be drawn from sector-specific data:

- *Cement industry*: Responsible for 5%–8% of global CO_2 emissions. Approximately 40%–50% of CO_2 emissions from the cement industry arise from the combustion of fossil fuels in the rotary kilns used for calcination and clinker production. The remaining 50%–60% of the CO_2 emissions are released during the calcination process itself, during which limestone is broken down[190–193].
- *Lime production from limestone to quicklime*: Accounts for about 1%[194,195] of global CO_2 emissions.
- *Other industrial uses*: Likely contribute to a smaller, albeit non-trivial, share of global CO_2 emissions.

Combining the data, it can be estimated that direct emissions of rotary kilns contribute to roughly 8%–10% of global CO_2 emissions when considering their roles across the various industries.

2.10 Combustion-related pollutants

Aside from reducing CO_2 emissions, it is essential to decrease the levels of nitrogen oxides released in the atmosphere due to their deleterious effects on the environment and human health[196]. In the troposphere, NO_x species impact photochemical smog[199] and ozone in the urban area[200], while in the stratosphere it influences mainly the reduction of ozone[201–203]. Overall, NO_x has impacts on the health of ecosystems (acidification, reduction of crop yields) and the health of humans (cancer-causing). These impacts may be less-severe in Europe and North America than in Asia, where very high concentrations of NO_x have been recorded in urban zones[204].

NO_x may serve as a better indicator of sustainability than CO_2. This is because NO_x shows strong correlations with each pillar of sustainability, providing a more-comprehensive and encompassing view[197]. While it is mainly NO_2 that affects the environment, NO is a precursor of NO_2. Globally, NO_x mainly arise from transport and industry through combustion technologies. In the iron and steel industry, for the case of China[198], sintering is the main source of NO_x, followed by the pelletising process and the BF.

Policy – Two limits have been set for the quality of air as standard for Europe with a maximum concentration of NO_x as NO_2 of 200 $\mu g/m^3$ for an averaging period of 1 hour, with no exceeding of this level more than 18 times per year. The second limit is 40 $\mu g/m^3$ for an averaging period of 1 year[205]. Moreover, for industrial furnaces, CEN - EN 14792 standard (Stationary source emissions - Determination of mass concentration of nitrogen oxides - Standard reference method: chemiluminescence)[206] specifies the limit for emissions in the flue gas that is used for the pelletising process.

NO_x units – Several units are commonly used to express NO_x concentrations. According to EU Directives, NO_x levels are expressed in mg/m^3 of NO_2 on a dry basis, under standard conditions (273 K and 101.3 kPa) and at a specified oxygen value. For measurements, the term ppm (parts per million) is frequently used to indicate the concentration of NO and/or NO_2 in flue gases. In this study, ppm will be used in the findings from the Paper I, and the unit mg/MJ will be used for Paper II, III, ECF data and full-scale data to compare the efficiency of the flame in producing less NO_x for the same amount of fuel.

NO_x abatement strategies – Staging combustion is scarcely feasible in a rotary kiln for the iron industry due to the rotary kiln and the need for a high O_2 partial pressure for the product. This means that there are two alternatives to reduce NO_x levels: post-treating NO_x and/or developing a low-NO_x burner.

Post-treatment systems, such as selective catalytic reduction (SCR), selective non-catalytic reduction (SNCR), and wet scrubbing incur significant additional costs and their efficiencies might be limited by a high exhaust flow (>300,000 Nm^3/h) and a high lambda value, rendering the NO_x concentration low (< 300 ppm).

2.11 Summary - Transitioning to a low-CO_2 fuel - Questions to answer

To summarise Chapter 2, the aim of this thesis is to explore the potential to reduce by 25% the CO_2 emissions from pelletising plants through the adoption of a co-firing strategy, partially replacing coal with hydrogen. This investigation raises the following key questions:

- How do the flame behaviour and flame characteristics change when transitioning from the reference fuel to a co-firing flame?
- How do the NO_x emissions evolve under co-firing conditions?
- What would be the most-effective strategy for implementing hydrogen at full scale?

3 Co-firing of gaseous and solid fuels

This chapter presents a literature review on the alterations to flame characteristics and NO_x emissions levels that occur during the co-firing of gaseous and solid fuels. In addition, the theory of NO_x formation relevant to the studied applications and fuels is discussed.

3.1 Literature review of flame characteristics and NO_x emissions in co-firing solid and gaseous fuels

The literature on hydrogen (H_2) and coal co-firing is limited. Most of the existing research has focused on co-firing gaseous fuels, particularly ammonia (NH_3), with coal. However, exploring other co-firing set-ups, such as H_2 with refuse-derived fuel (RDF), H_2 with NH_3, natural gas with H_2, and natural gas with coal, could provide valuable insights that are relevant to the field.

Ammonia-Coal:

Zhu et al.[207] demonstrated that adding NH_3 to coal enhanced the release of volatiles, resulting in earlier ignition under both fuel-lean and fuel-rich conditions. They observed that under co-firing conditions, coal particles exhibited higher oxidation reactivity, which aligns with the findings of Ueki et al.[208] in their study of H_2-coal co-firing.

Ishihara et al.[209] showed that when NH_3 was co-fired with coal the nitrogen oxide (NO_x) concentrations increased linearly with up to 60% NH_3, after which they decreased at higher NH_3 concentrations (80%). Similarly, Tamura et al.[210] showed that air-staging significantly reduced NO_x emissions during coal-ammonia co-firing. Zhang et al. [211] reported a similar trend, where the NO_x levels increased with up to 30% NH_3 content but decreased as the NH_3 concentration reached 50%, which was the highest level tested.

Ding et al.[212] conducted a numerical study that highlighted the complex effects of NH_3 on NO_x emissions. They concluded that the addition of NH_3 either reduced or increased the outlet NO_x levels depending on the residence time at high temperatures. Longer residence times led to higher levels of NO_x emissions. In addition, they found that NH_3 reduced the combustion rate of pulverised coal. Chen et al. also performed a numerical study, concluding that the co-combustion of coal and ammonia significantly increases NO_x emissions[213].

Hydrogen-Ammonia:

Biebl et al.[214] reported that air-staging could reduce NO_x emissions during ammonia-hydrogen co-firing, and they observed that H_2 addition to NH_3 helped decrease the NO_x levels. Interestingly,

they noted that the flame colour during NH_3/H_2 co-firing was distinctly yellow/orange, as compared to the bluish flame produced during NH_3/CH_4 or NH_3/CO co-firing.

RDF-Hydrogen:

Hercog et al.[215] found that co-firing refuse-derived fuel (RDF) with hydrogen at a 90:10 ratio increased NO_x emissions. Their study, which combined experimental and modelling approaches, was applied to cement kiln combustion. Hydrogen was found to enhance combustion, in that it promoted earlier ignition.

Hydrogen-Coal:

Pisa et al.[216] conducted an experimental study in a 2-MW pilot furnace, observing a reduction in NO_x emissions when H_2-enriched gas was injected into a pulverised coal combustion system. Ueki et al.[208] investigated H_2 injection into coal combustion and found that H_2 enhanced the release of volatile matter and increased the porosity of char, thereby improving coal combustion. They also identified an optimal H_2 flow rate for efficient combustion.

Ilbas et al.[217] performed a numerical study in which they observed that H_2 injection into coal combustion increased the gas temperature but led to an exponential increase in NO_x emissions with increasing H_2 content. Ehlmé et al.[218], using modelling, have shown that adding particles to a H_2 flame, such as in hydrogen-coal co-firing, significantly influences radiative heat transfer, as compared to pure H_2 flames.

Coal-hydrogen in Blast Furnaces:

Gan et al.[219] conducted a numerical study on the effect of adding H_2 to BFs. They found that while H_2 improved the combustion of biochar, it hindered the combustion of char due to O_2 consumption by H_2. A similar study carried out by Ren et al.[220] reported that H_2 addition enhanced the combustion of pulverised coal in BFs. Liu et al.[221] found that H_2 injection into BFs facilitated the devolatilisation of coal but hindered the combustion of the resulting volatiles.

Natural Gas and Hydrogen:

In turbine applications, Lee et al.[222] found that adding H_2 to natural gas reduced the flame length but increased the NO_x emissions.

Methane-Coal:

Kim et al.[223] conducted a numerical study and found that adding methane to coal combustion reduced the overall NO_x emissions by decreasing the level of Fuel-N and increasing NO_x

reduction by re-burning. However, they hypothesised that the reduction in Fuel-NO_x was linearly correlated to the amount of Fuel-N in the mixture that contradicts experimental findings, suggesting that this linear assumption may not hold true in practice.

Table 2 summarises all the studies and their main conclusions for co-firing hydrogen or coal with another fuel. While much of the existing research has explored the potential of H_2 co-firing with a variety of fuels, there is a notable gap in the knowledge regarding hydrogen and coal co-firing in large flames, specifically in rotary kilns.

Table 2. Summary of studies on the relevant co-firing cases.

Study	Fuels	Conclusions
Zhu et al.	Ammonia + Coal	Ammonia enhances volatiles release and earlier ignition, with increased coal oxidation reactivity during co-firing.
Ueki et al.	Hydrogen + Coal	Hydrogen enhances volatiles release and increases char porosity, improving combustion, with an optimal hydrogen flow rate for efficiency.
Ishihara et al.	Ammonia + Coal	NO_x increases linearly for up to 60% ammonia but decreases at higher concentrations of ammonia (80%).
Tamura et al.	Ammonia + Coal	Air-staging significantly reduces NO_x emissions during ammonia-coal co-firing.
Zhang et al.	Ammonia + Coal	NO_x levels increase for up to 30% ammonia, then decrease as the ammonia concentration reaches 50%.
Ding et al.	Ammonia + Coal (Numerical)	Ammonia can either reduce or increase the level of NO_x depending on the residence time, with longer residence times causing higher levels of NO_x emissions. Ammonia also reduces the coal combustion rate.
Chen et al.	Ammonia + Coal (Numerical)	Coal-ammonia co-firing significantly increases the levels of NO_x emissions.
Biebl et al.	Ammonia + Hydrogen	Air-staging reduces the levels of NO_x emissions during ammonia-hydrogen co-firing. Hydrogen helps decrease the levels of NO_x, burning with a distinct yellow/orange flame.
Hercog et al.	RDF + Hydrogen	RDF-hydrogen co-firing (90/10) increases the levels of NO_x emissions. Hydrogen enhances combustion, promoting earlier ignition.
Pisa et al.	Hydrogen + Coal	Hydrogen injection reduces NO_x emissions during pulverized coal combustion in a pilot furnace.

Ilbas et al.	Hydrogen + Coal (Numerical)	Hydrogen injection increases the gas temperature but causes an exponential increase in NO_x emissions with higher hydrogen content.
Ehlmé et al.	Hydrogen + Coal (Modelling)	Adding coal to hydrogen flames significantly increases radiative heat transfer.
Gan et al.	Hydrogen + Coal (Blast Furnace)	Hydrogen enhances biochar combustion but hinders coal combustion due to oxygen consumption by hydrogen in blast furnaces.
Ren et al.	Hydrogen + Coal (Blast Furnace)	Hydrogen addition enhances pulverised coal combustion in blast furnaces.
Liu et al.	Hydrogen + Coal (Blast Furnace)	Hydrogen injection aids devolatilisation of coal but hinders combustion of the resulting volatiles in blast furnaces.
Lee et al.	Hydrogen + Natural Gas	Hydrogen addition reduces the flame length but increases NO_x emissions in turbine applications.
Kim et al.	Methane + Coal (Numerical)	Adding methane reduces NO_x emissions both by decreasing the levels of Fuel-N and re-burning NO_x. However, their linear assumption for Fuel-NO_x reduction may not be valid in practice.

3.2 Formation of nitrogen oxide

Here, only the formation of NO is discussed, as it is by far the major species in NO_x emissions from high-temperature flames. Numerous elementary reactions contribute to the formation of NO during combustion[224]. Nitrogen atoms to form NO can come from two sources: the Fuel-N and the air. The rate of NO formation depends on the rate constants and the radical pool.

3.2.1 Zeldovich mechanism

The rate of NO formation via the Zeldovich mechanism increases exponentially with temperature, becoming significant at temperatures >1,700 K, which is why it is termed *thermal NO formation*. At these high temperatures, molecular nitrogen and oxygen undergo a series of reactions. The primary elementary reactions are as follows[225,226]:

- $N_2 + O \leftrightarrow NO + N$ (R1)
- $N + O_2 \leftrightarrow NO + O$ (R2)
- $N + OH \leftrightarrow NO + H$ (R3)

R1 is both the initiating and the rate-limiting step, requiring a high activation energy (320 kJ/mole). R1 and R2 represents a chain sequence reaction that results in a large amount of NO being produced by a small amount of atomic oxygen.

The rates of R1 and R2 are sensitive to temperature, not only due to the high activation energy of R1, but also because of the concentration of atomic oxygen, which increases rapidly at high temperature.

The reaction detailed in R3, known as the extended Zeldovich reaction, is important under reducing conditions when the rate of R2 is reduced by the low O_2 concentration.

For the modelling, since the rate coefficient of R1 is well-established, calculating the thermal NO production rate is straight-forward if the concentration of oxygen atoms is known. Away from the flame front, equilibrium O-atom concentrations allow for simplified calculations. However, in the flame front region, the super-equilibrium radical concentrations complicate the estimation of NO formation. Super-equilibrium occurs due to fast bimolecular reactions at the flame front and slower termolecular recombination reactions post-flame. Accurate prediction of Zeldovich NO production requires a proper description of the chemistry kinetics at the flame front.

3.2.2 The NNH Route mechanism

Bozzelli and Dean[227] have proposed an NO formation route that involves NNH radicals according to R4 and R5:

- $N_2 + H \rightarrow NNH$ (R4)
- $NNH + O \rightarrow NO + NH$ (R5)

The NNH route is linked to the N_2O route via R6[227]:

- $NNH + O \rightarrow N_2O + H$ (R6)

The importance of the NNH route is not fully understood. Haworth et al. have concluded that the NNH pathway is of minor importance for NO formation in most combustion systems[228]; Purohit et al.[229] have found that the NNH pathway dominates in the early flame region for fuel-lean H_2 flames, while Glarborg et al.[230] have observed that the NNH pathway is most significant under slightly reducing conditions and at higher temperatures. Other studies have shown the importance of the NNH pathway at low temperatures[231,232], at high temperatures[233], in a fuel-rich mixture[234], in H_2 flames[235–240], and for hydro-carbon fuels with high carbon-to-hydrogen ratios[241]. There seems to be a consensus regarding the presence of the NNH pathway at the flame front, where high concentrations of H and O radicals appear from the H_2 flames. Although the NNH route may

be of importance at the flame front when co-firing hydrogen and coal in rotary kilns, it is still expected to be significantly less important than thermal NO_x and Fuel-NO_x formation, so it is not studied in this work.

3.2.3 N_2O route

The N_2O-route is initiated by the intermediate formation of N_2O through the recombination R7. The collision with M, representing all molecules present in the reaction, promotes the reaction at high pressures due to the higher concentrations of a third body. These three-body reactions typically have low activation energy. Therefore, they can be important at lower temperatures. The N_2O route is also favoured in lean combustion conditions[242] making it of low importance for the current application.

- $N_2 + O + M \rightarrow N_2O + M$ (R7)

The N_2O thus formed may then react to form NO via the following reactions:

- $N_2O + O \rightarrow NO + NO$ (R8)
- $N_2O + H \rightarrow NO + NH$ (R9)

3.2.4 Fenimore Mechanism (Prompt NO)

The Fenimore mechanism, identified by Fenimore in 1971[243], pertains to the interactions of fragmented hydrocarbons with molecular nitrogen at relatively low temperatures. Lamoureux et al. have provided a comprehensive analysis of the pathway from path-N to nitric oxide (NO)[244]. The primary equations governing this mechanism are as follows:

- $O + N2 + M \rightarrow N_2O + M$ (R10)
- $H + N_2O \leftrightarrow NO + NH$ (R11)
- $O + N_2 \leftrightarrow NO + NO$ (R12)

3.2.5 Nitrogen route for fuel nitrogen content (Fuel-N)

Coals typically have a nitrogen content in the range of 0.5%–2.0% by weight[245–247], which is denoted as *Fuel-N* in this work. The conversion rate of Fuel-N to NO has been found to decrease along with increases in the nitrogen content of the fuel[248,249]. It is acknowledged that the vast majority of the Fuel-N is sequestered within aromatic rings[247,250–252]. N-5 (pyrrole-type) is the most-abundant (50%–80%), followed by N-6 (pyridine-type) (20%–40%), and N-Q (quaternary type) (0%–20%)[253–255]. Figure 5 depicts a schematic of coal particle devolatilisation. Initially, the coal particles undergo drying, followed by further heating, which initiates devolatilisation. This process results in the fragmentation of the coal particles into volatiles and

char. The volatiles are categorised into two primary groups: light gaseous species and tar. The volatiles react with the surrounding air in a small envelope around the remaining particle, which is char. Volatiles combust on a relatively short time-scale compared to the combustion of char, which takes place subsequently during the flame reactions.

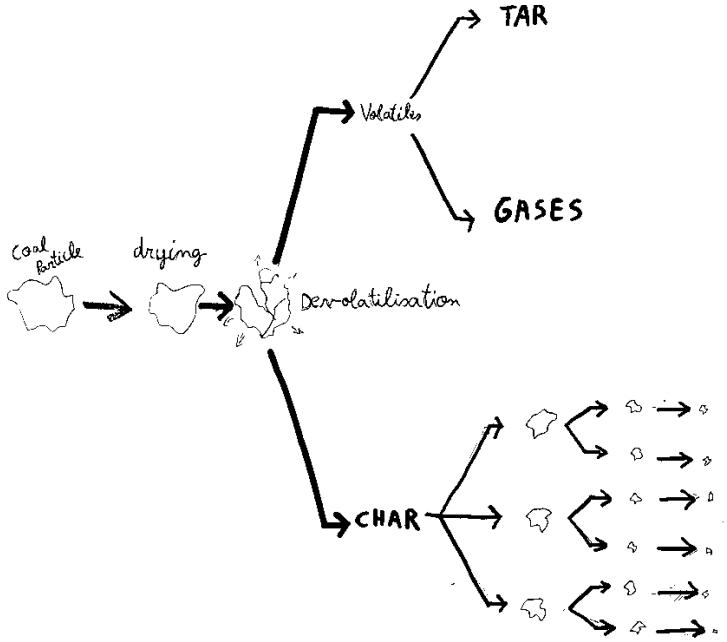

Figure 5. Schematic of the devolatilisation of coal particles.

Tar

Tar includes a broad range of compounds, and it has not been fully defined[256]; however, it is accepted that the majority of the species that form tar are aromatics[257–259]. Several studies have discussed the function of tar as a precursor of soot, which means that it plays an important role in heat-radiative activities [259–261]. Tar plays an indirect role in NO formation, and this aspect is not developed further in the current work.

Volatiles

Volatiles refers to volatile components that are released as gases during solid fuel devolatilisation. High levels of volatile matter generally lead to easier ignition. It is generally acknowledged that higher-rank coals are associated with lower contents of volatiles[262,263]. Furthermore, an increase in pyrolysis temperature is known to facilitate the release of nitrogen-containing volatiles[254,264–267], and a higher heating rate tends to enhance the overall yield of volatiles. The existing literature suggests that the augmented generation of volatiles at high heating rates can be attributed to two primary factors. First, there is enhanced thermal fragmentation of the coal's molecular structure[263],

which serves to impede secondary reactions. Second, there is notable migration of fixed carbon into the gaseous phase[268].

Nitrogen is predominantly released in the form of volatiles, primarily as hydrogen cyanide (HCN) and ammonia (NH_3). Kambara et al.[254] have found that HCN and NH_3 collectively account for 90%–95% of total nitrogen emissions from pulverised coal, with the remaining nitrogen being released in trace amounts of additional nitrogen-containing compounds, which include CH_3CH, CH_2CHCN, and C_6H_6CN. HCN is widely regarded as the principal nitrogen-containing volatile emitted during the devolatilisation process for moderate- to high-rank coals in high-temperature processes, with its importance increasing as the coal rank rises[254,269,270]. Conversely, NH_3 is recognized as playing a more-substantial role in the devolatilisation of low-rank coal varieties[271,272]. Ammonia has been documented as predominating over HCN during coal devolatilisation; however, such occurrences are typically associated with low-rank coals and devolatilisation temperatures below 900°C[273].

Debate continues to rage regarding the origins of HCN, NH_3. Among the various hypotheses dealing with the formation of NH_3, Kambara et al.[254] have suggested that NH_3 formation originates from quaternary nitrogen (N-Q) present in the gas phase. In contrast, Nilson et al.[274] have proposed that NH_3 is produced via the intermediary compound HNCO. Wolfrum et al.[275] have hypothesised that NH_3 arises from the hydrogenation of HCN in the gas phase. Bessilakis et al.[276] have indicated that a portion of the NH_3 might be generated on the surface of char. In addition, Schäfer et al.[277] have proposed that NH_3 formation occurs through the hydrolysis of HCN. Li et al.[278] have suggested that NH_3 is formed through the direct hydrogenation of coal-derived nitrogen (coal-N) by hydrogen radicals. Finally, Yuan et al.[279] have proposed that nitrogen is released directly as -NH and $-NH_2$ radicals that subsequently combine with H_2. As the reactions of –NH and $– NH_2$ radicals with H radicals form NH_3 but do not involve bond breaking or recombination, they conclude that NH_3 is a primary product before the formation of HCN. Moreover, they have shown that the process of HCN formation from -NH, $-NH_2$, $-CH_2$, and $-CH_3$ involves bond breaking and recombination, resulting in a higher activation energy barrier for HCN formation compared to NH_3 formation.

Liu et al.[280] have reported that the presence of water during initial pyrrole pyrolysis impacts the HCN/NH_3 ratio. In the presence of H_2O, both HCN and NH_3 are formed, while in the case of H_2O depletion, only HCN is formed.

The oxidation of HCN or NH_3 ultimately results in the formation of either N_2 or NO. The pathway through which nitrogen transitions from HCN and NH_3 to NO is heavily influenced by local environmental conditions, leading to variations ranging from 0% to 100%.

Under oxidative conditions, characterised by the presence of O or OH, the nitrogen contained in volatile compounds is predominantly converted to NO. Conversely, in reductive environments, where species such as isocyanate (NCO) or NO are present, the nitrogen-containing species that initially formed NO, N-, NCO, and NH- are more likely to be reduced to nitrogen gas (N_2).

As illustrated in Figure 6, which includes the main pathways for modelling HCN and NH_3 taken from Glarborg et al.[281], HCN undergoes oxidation to form the NCO radical either directly or via CN as an intermediate. NCO appears to be a crucial species, in that it serves as a branching point for multiple reaction pathways, leading to the formation of NO, N_2 or N_2O. In an oxygen-rich environment, NCO predominantly reacts to produce NO, whereas in the presence of NO, it tends to facilitate the formation of N_2, although it may also oxidise to N_2O.

For NH_3, its conversion to NO occurs in the presence of OH, O, and H, progressing through intermediate species such as NH_2, NH, and HNO. Alternatively, if NO is already present, NH_3 can lead to N_2 formation via the intermediate species of NH_2 and NH, followed by N, NNH, and N_2O.

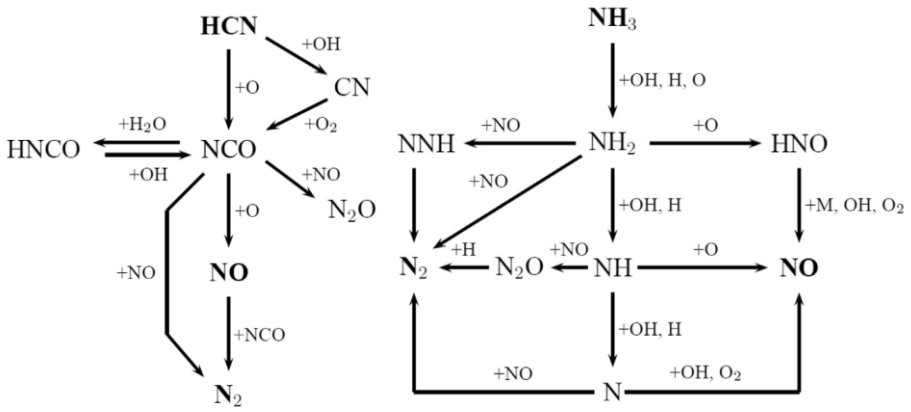

Figure 6. (a) Modelling the HCN to NO pathway. (b) Modelling the NH_3 to NO pathway. Reference[282]

Char combustion

During the process of pyrolysis, nitrogen liberation from coal char has been found to occur through two distinct mechanisms. First, nitrogen can be transported away within the tar aromatic clusters as they undergo vaporisation[283]. Second, nitrogen can be released from the char in the form of volatile light gases, facilitated by ring rupture[284].

The presence of oxygen facilitates the conversion of the nitrogen bound to char into NO[285,286]. Discussions regarding the interactions of char with NO are on-going[287,288] and are attracting a lot of attention because char-N has been found to be a significant contributor to NO formation in certain conditions. It is necessary to consider the challenging distinction between intrinsic and apparent char-N conversion. Intrinsic char-N conversion refers to the direct formation of NO from char-N before any subsequent reactions, while apparent char-N conversion accounts for both the formation and reduction of NO by the char itself. Since most measurements are taken post-combustion, apparent conversion data dominate the literature.

Despite extensive studies on char-N conversion, the obtained results exhibit considerable variability, with reported char-N conversion values in the range of almost 10%–100%, with the variability being attributed to differences in stoichiometry, sample size, and experimental methods[289–293].

Phong-Anant et al.[294] have demonstrated that under fuel-lean conditions (λ = 1.25–1.67, T = 1,673–1,773 K), vol-N is the predominant source of NO, whereas under fuel-rich conditions (λ < 1), char-N accounts for 60%–90% of the total NO produced, whereas at near-stochiometric conditions, the conversion rate decreases to 20%–30%. They have also reported that NOx formation from volatile matter is proportional to the amounts of HCN and NH_3 released, while char burnout is the primary factor influencing the conversion of char-bound nitrogen (char-N) to NOx.

Jensen et al.[287] have demonstrated that char-N conversion to NO approaches 100% at high temperatures (1,323–1,423 K) when small samples (<1 mg) are combusted, due to minimising NO-char reduction. At 1,123 K, the conversion rate dropped to 65%, with further reductions observed as the sample size increased. The availability of oxygen did not significantly influence the conversion rate for small samples, suggesting that intrinsic char-N conversion is close to completion at high temperatures, and the lower reported values primarily arise from NO reduction by char. Furthermore, Jensen et al. have observed that NO reduction by char occurs significantly faster, immediately after pyrolysis, as compared to when the char is prepared separately, possibly explaining the discrepancies in the literature regarding NO-char reduction kinetics.

The experimental approach also significantly affects the char-N conversion values. Molina et al.[295] have compared two methods that gave different outcomes. In the first (Type I) experiment, char was injected into a helium atmosphere and pyrolysed for 60 seconds before an O_2/He mixture was introduced for combustion. This method resulted in low rates of char-N conversion (10%–15%). In the second (Type II) experiment, char was directly injected into the O_2/He stream,

yielding higher conversion rates (40%–55%). The authors attributed this difference to lower local stoichiometry in the Type I experiment, which likely promoted homogeneous reduction involving HCN. Although the role of HCN as an intermediate in char-N conversion is not fully established, some modelling studies[296,297] have suggested that assuming HCN as a primary product can yield reasonable predictions.

The conditions under which char is produced influence significantly the conversion of char-N. Shimizu et al.[298] have emphasised that the pyrolysis process affects subsequent NO formation.

Song et al. [292] have reported that, for lignite char, the conversion of char-N to NO_x ranges from 0% to 40% at 1,250 K. Similarly, the study conducted by Spinti et al.[289] has shown that the rate of char-N conversion to NO_x varies between 50% and 60% for lignite and is 40%–50% for bituminous coals. Furthermore, their findings indicate that enriching the combustion air with NO leads to a decrease in the apparent NO_x formation within the char flame. The optimal condition was identified at 900 ppm NO, under which the apparent char-N conversion to NO_x was reduced to 0%. Furthermore, Spinti et al. have observed that increasing the partial pressure of O_2 enhances char-N conversion to NO_x, a trend that has also been reported by Visona et al.[297].

N-partitioning between volatiles and char

During coal devolatilisation, Fuel-N is released with either the volatiles or the char. The percentage partitioning of the nitrogen in coal between char and volatiles can vary between 0% and 100%[299–302]. Knowledge of the coal rank and combustion conditions is needed for estimating the partitioning. Song et al.[303] have demonstrated that in a coal-feeding system where there is a high volume of transport air within the pulverised coal flow, the generation of NO is influenced by the concentrations of both the char-N and vol-N. Conversely, when the transport air is minimalised, the production of NO_x is predominantly derived from vol-N. Hansson et al.[304] have found that for bark and at a pyrolysis temperature <1,000°C, the NO_x originating from volatile sources is primarily generated at the ignition point.

Pershing et al.[305] have shown that in pulverised coal combustion, the majority of NO_x originates from vol-N. However, Edland et al.[306] have determined that in rotary kiln combustion of low-volatiles, pulverised sub-bituminous coal, most of the NO is produced from the char.

3.3 Nitrogen path in co-firing hydrogen and coal

On the one hand, NO formation in H_2 flames is expected to be dominated by thermal NO, due to the high-temperature application[235,307,308]. On the other hand, the formation of NO during the

combustion of coal in full-scale power plants is primarily attributed to the presence of Fuel-N[306]. Under conditions of hydrogen-coal co-firing, the nitrogen pathway to NO involves complex interactions, which may differ significantly depending on how the coal and hydrogen are implemented.

Substituting 30% of the coal with hydrogen corresponds to a reduction of 30% in the flow of Fuel-N. However, it is crucial to recognize that the conversion of Fuel-N to NO is not directly proportional to the concentration of Fuel-N present. The introduction of even a modest amount of Fuel-N into the combustion process significantly enhances NO formation[248,249]. In contrast, when a consistent concentration of Fuel-N is already established, additional increments of Fuel-N do not yield a corresponding increase in NO emissions. Thus, a 30% reduction in the flow of Fuel-N may not significantly impact the Fuel-NO levels.

A proposed, theoretical, low-NO formation strategy during the substitution of 30% of the coal with hydrogen involves three strategic goals to be achieved through H_2 injection. These are: (i) increased heating rate and temperature of the coal particles, to motivate the release of Fuel-N in volatiles; (ii) the depletion of O_2 in the jet coal flames, to force the conversion of as much as possible of the volatiles-N into N_2; and (iii) the mixing of early NO with later char-NO, so as to enhance the reduction of volatiles-NO by char-NO.

3.4 Scaling up flames

The final section of this chapter presents a literature review that concerns the challenges associated with scaling flames, which is a critical issue in combustion research when transitioning from laboratory-scale experiments to industrial applications.

Table 3 presents the two main scaling approaches of constant velocity scaling and constant residence-time scaling, each of which affects the flame characteristics, such as ignition, combustion efficiency, emissions, and heat transfer, in distinct ways.

Constant Velocity Scaling: In the constant velocity scaling method, the velocity of the reactant flow is maintained consistently between the scales. This approach preserves the aerodynamic effects but alters the residence time of the reactants in the flame zone.

Constant Residence-Time Scaling: In the constant residence-time approach, the residence time of the reactants in the flame zone is maintained across the scales, ensuring similar chemical reaction times and combustion characteristics. While this method preserves the reaction kinetics, it alters the aerodynamic effects, potentially influencing flame shape and stability.

However, scaling down a full-scale configuration while maintaining constant residence time can be impractical due to the extremely low velocities required, which may not be feasible for achieving accurate scaling, particularly in solid fuel combustion.

Ekland et al.[309] investigated the impact of constant velocity scaling on NO_x emissions in industrial jet flames, focusing on those with high excess air ratios, such as those used in rotary kilns for iron ore pellet production. Their findings indicate that, even when combustion settings and velocities are accurately scaled, the oxygen concentration encountered by the fuel during char combustion varies across the scales. Since NO_x formation is strongly influenced by char combustion, these scaling-induced variations can significantly affect the overall NO_x emissions. Smart et al.[310] explored the impacts of various scaling criteria on the performances of swirl-stabilised, pulverised coal burners. They compared burners that were scaled from a 50-MW thermal input reference case to a 2.5-MW set-up, applying both the constant velocity and constant residence-time scaling approaches. Their findings demonstrate that the choice of scaling criterion significantly impacts burner performance, especially regarding ignition distance and NO_x emissions. The constant velocity burner exhibited higher NO_x emissions compared to the constant residence-time burner. Overall, they concluded that for pulverised coal flames, the constant residence-time approach yields better results. In a similar vein, Weber[311] have further emphasised that scaling influences the flow characteristics within combustion chambers, as well as the heat transfer rates and the levels of emissions of pollutants, particularly NO_x. Hsieh et al.[312] identified several factors that affect NO_x emissions in scaling conditions, such as burner size, turn-down ratio, combustion air pre-heating, excess air dilution, and fuel staging. They found that these factors contribute to multiple NO_x formation regions, each with distinct scaling behaviours. Their study proposed that the primary source of NO_x at full load is the near-burner region, suggesting that maintaining fuel injection and the Reynolds number is crucial for accurately scaling NO_x emissions from small- to full-scale systems. Sun et al.[313] conducted a batch combustion study, albeit not directly related to rotary kiln applications. Their conclusions indicate that flame behaviour varies with fuel size, with larger fuel quantities manifesting stronger internal radiation effects.

The work conducted in the HICK and ECF Units is scaled according to the constant velocity scaling of the coal flow. Residence time scaling is not feasible because the coal injection velocity is too low. While the velocity of the coal flow is constant, the ratio of transport air to coal flow is not maintained at the same level. Due to the smaller scale, coal transportation becomes more challenging, requiring an increased transport air flow compared to a full-scale Unit.

Table 3. Comparison of the scaling up of flames using constant velocity scaling and constant residence time scaling.

Aspect	Constant Velocity Scaling	Constant Residence Time Scaling
Residence Time	Decreases with scale	Maintained
Flow Velocity	Constant	Increases with scale
Heat Transfer	May change due to altered residence time	More consistent
NO_x Formation	Affected due to shorter residence time	More predictable
Flame Stability	Less stable at smaller scales	Can alter aerodynamic effects, may be challenging in small scales
Aspect	Constant Velocity Scaling	Constant Residence Time Scaling

4 Method

The methodology of the work of this thesis is structured in a step-wise manner, progressively increasing the scale of fuel input from 100 kW to 580 kW. An overview of the method is presented in Figure 7. The measurement data from the pilot-scale units are related to the measurement data from the LKAB full-scale production plants. Table 4 provides a comparative overview of the pilot-scale and full-scale combustion plants, highlighting the key operational parameters, such as power capacity, fuel type, secondary air temperature, lambda (air-to-fuel ratio), and burner configurations. The pilot-scale units, including the Chalmers Unit, HICK, and ECF, operate at significantly lower power levels (100–580 kW) and utilise various fuel combinations, including lignite, sub-bituminous coal, propane, and hydrogen. In contrast, full-scale plants operate at much higher capacities (30–50 MW) and primarily use oil (EO5) and sub-bituminous coal as fuel sources. The Chalmers Unit operates with ambient-temperature primary air and does not utilise a secondary air flow, unlike the other furnaces, which use heated secondary air. The secondary air temperature in the HICK unit is notably lower at 850°C compared to those in the full-scale plants (1,100–1,200°C), while the ECF unit is intermediate at 1,000°C.

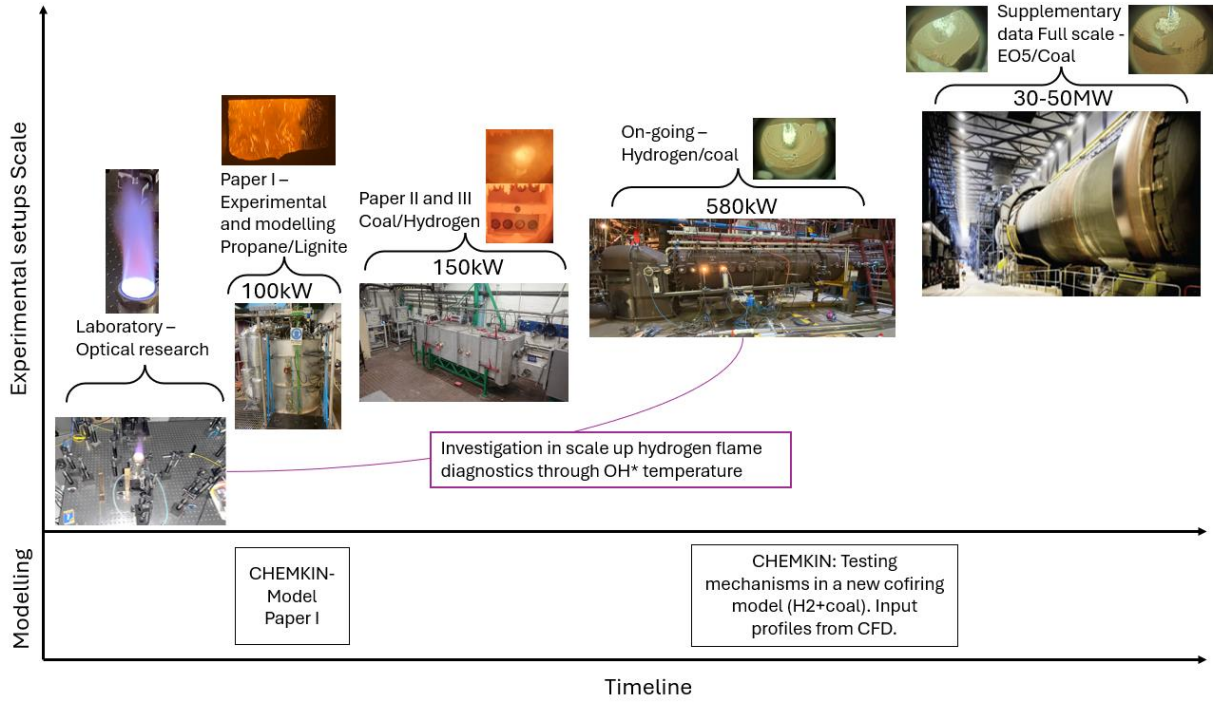

Figure 7. Overview of the method applied in this thesis.

Table 4. Comparisons of the pilot-scale and full-scale plants.

	Power	Fuel	Secondary air temperature (°C)	Lambda	Burners Type	Pellets bed
Chalmers Unit	100 kW	Lignite Propane	Ambient temperature	1.15 and 1.623	Combi-burner	No
HICK	150 kW	Sub-bituminous coal, hydrogen	850	3.6	Combi-burner and burner and lancing	No
ECF	580 kW	Sub-bituminous coal, hydrogen	1,000	4–5	Combi-burner	No/Yes (simulated)
Full-scale plants	30–50 MW	Oil (EO5) Sub-bituminous coal	1,100–1,200	4–6	Combi burner and separated burners	Yes

Experimental campaigns incorporating both conventional and advanced measurement techniques, alongside theoretical modelling, are employed to analyse the flame characteristics and NO_x chemistry. The primary measurements include the thermocouples in the shells of the furnaces, the outlet gas concentrations, in-flame gas concentrations, ignition locations (inferred from the spectrometry data, as detailed in **Paper III**), flame width and length (from camera visualisation), flame stability (from spectrometry and camera data), flame intensity, coal particle temperature, and heat transfer from the flame. Note that not all measurements were applied in every campaign. An overview of the measurement techniques is presented at the end of this chapter.

These measured flame characteristics are critical for assessing the burner technologies. The evaluation of co-combustion flames entails three steps (described in detail below): 1) Flame characteristics; 2) Pilot-scale trials; and 3) Up-scaling and demonstration. In addition, since previous measuring devices did not capture changes in hydrogen combustion, a laboratory-scale measurement technique that uses OH Chemiluminescence to determine gas temperature near the flame front is now being explored for scaling-up flames. A section dedicated to this technique is presented in the on-going work.

4.1 Step 1: Flame Characteristics in Co-Firing Gaseous and Solid Fuels

To assess the flame characteristics during the co-firing of gaseous and solid fuels, a fuel sweep ranging from 100% propane to 100% lignite at constant power was performed while the flames were characterised with a camera and by measuring the outlet gas concentration. In-flame gas concentrations were measured for three cases: 100% lignite; 50% lignite and 50% propane; and 100% propane. Although the operating conditions differ from those of full-scale applications, this step provides flexibility and extensive measurement capabilities for detailed analyses. The experiments were conducted using the Chalmers 100-kW combustion unit, which offers an ideal platform for accurate measurements. In addition, a computational model was developed to examine the partitioning of NO_x between thermal-NO and Fuel-NO, as well as the impact of early volatiles release. The furnace, the burner type, the fuel analysis, and the modelling approach with underlying assumptions are presented next.

4.1.1 Chalmers 100-kW furnace

The experiments described in Paper I were conducted in the Chalmers 100–kW combustion unit, which is presented in Figure 8. The furnace contains four water-cooled rods near the wall to extract heat from the combustion process and stabilise the flame. Air and fuel are injected at the top of the furnace through a multi-fuel burner that is capable of operating with both gaseous and solid fuels. Studies performed in this furnace may be found in the following references[314–316].

To allow optical and physical access to the flame, seven measurement ports (M1 to M8) are installed on the furnace side.

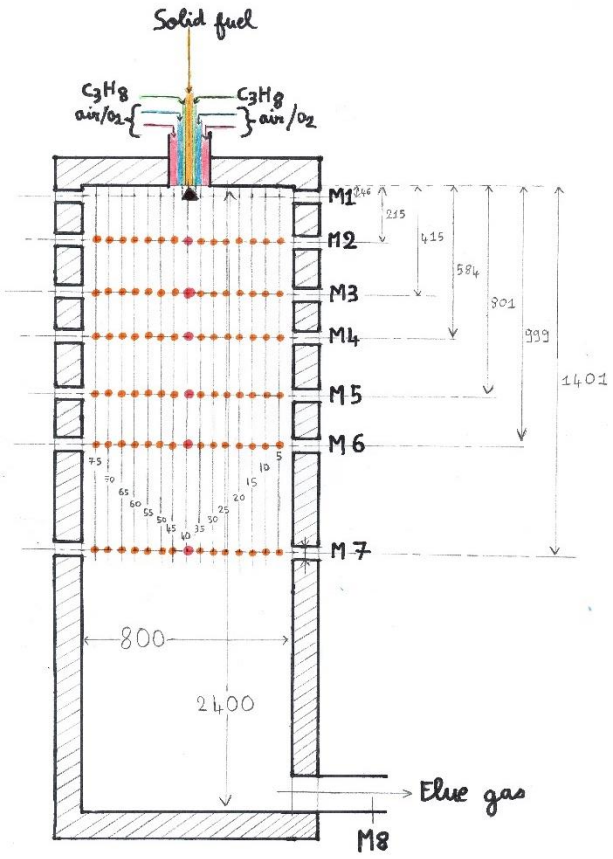

Figure 8. The cylindrical 100-kW Chalmers unit with height of 2400 mm and diameter of 800 mm. M1 to M8 refer to the measurement ports. The burner is installed at the top with primary air, propane and lignite injections. The drawing is included in Paper I.

4.1.2 Burner

Figure 9 presents a schematic overview of the burner in the Chalmers 100-kW unit. The burner allows central solid fuel feeding and annular gas injection through a perforated plate with eight holes. These gas injection holes are surrounded by two swirled air feeders, angled at -45° for the inner air and 15° for the outer air. A cone at the burner outlet helps to spread the solid fuel, improving combustion stability. Under co-firing conditions, the cone ensures thorough mixing of the two fuels.

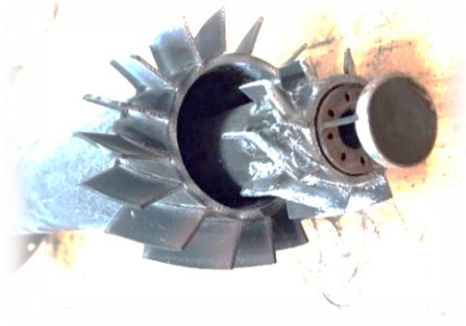

Figure 9. Photograph of the combi-burner used in the Chalmers Unit. The centre hole is for lignite injection, the surrounding holes are for propane, and both outer registers with blades is for the primary air with swirl.

4.1.3 Fuels

The fuels used in **Paper I** are propane and lignite. Sub-bituminous coal – used in the full-scale unit – has also been tested in place of lignite. However, it did not ignite properly in the Chalmers furnace, due to too-low-temperature conditions. Thus, only the results for lignite are presented. The proximate, ultimate and calorimetric analyses of the lignite are presented in Table 5.

Table 5. Proximate, ultimate, and calorimetric analyses for lignite.

Proximate analysis (as-received)		**Standard**
Moisture (%)	10.2	ISO 589:2018 mod
Volatile matter (%)	57.9	ISO 562:2010 mod
Fixed carbon* (%)	36.5	ISO 562:2010 mod*
Ash (%)	5.6	ISO 1171:2018
Ultimate analysis (as received)		**Standard**
Cl (%)	0.017	ASTM D4208-2019 mod
S (%)	0.659	ASTM D4239-2018
C (%)	61.8	ASTM-D5373:2016
H (%)	4.4	ASTM-D5373:2016
N (%)	0.7	ASTM-D5373:2016
O* (%)	26.9	ASTM D3176-2015*
Calorimetric analysis (as-received)		**Standard**
Calorific value Hi/LHV (MJ/kg)	22.9	ISO 1928:2020

*Calculated values.

4.1.4 Modelling

To gain a deeper understanding of NO_x formation in the lignite and propane flames within the Chalmers Unit, a detailed reaction model in CHEMKIN format was utilised. Two models were developed, one for the lignite flame and one for the propane flame, both based on a fixed gas temperature approach. A plug flow reactor (PFR) was chosen over a stirred tank reactor (CSTR), as a CSTR reactor is appropriate for combustion with low levels of turbulence and high mixing

zones before combustion, whereas a PFR is more suitable for non-pre-mixed and turbulent flames.

The temperature profiles of these models were established using in-flame temperature measurements conducted with a suction pyrometer in the Chalmers Unit. Additional input parameters included reactor length (matching the Chalmers Unit), fuel composition and flow, air composition and flow ($\lambda = 1.15$), and mixing profiles. In both models, the fuel was propane (C_3H_8) at a flow rate of 1.73 g/s, with increasing amounts of HCN to simulate Fuel-N levels up to 1.4 wt.%. The mixing profile was based on the lowest oxygen measurements in the flame – along the central line for propane and 10 cm off-centre for lignite.

Although the profiles are derived from experimental data, the primary objective of the model is not to precisely replicate real conditions, but instead to evaluate NO formation mechanisms under conditions that closely resemble experimental conditions.

The reaction mechanism used, developed by Mendiara and Glarborg[317], includes 97 species and 779 elementary reactions. Further details of the model can be found in **Paper I**. Sensitivity analyses were conducted on the temperature profiles and the implementation of Fuel-N as HCN and/or NH_3. Additional details and the results of this analysis are presented in **Paper I**.

4.2 Step 2: Pilot-Scale Trials

The hydrogen injection techniques were experimentally evaluated. The experiments were conducted in the pilot-scale unit HICK. HICK is a 150-kW furnace with temperature and flow conditions closer to full-scale applications than the Chalmers Unit. Two hydrogen injection strategies were evaluated: hydrogen-coal combi-burner, and hydrogen lancing with coal burner. This work evaluates the impacts of the injection technology on NO_x formation and flame characteristics. The evaluation includes combi-burner designs, hydrogen velocity, and hydrogen lance positions. The pilot-scale set-up balances industrial relevance with cost efficiency, allowing for the testing of various burner and lancing configurations. The furnace, the combi-burner and the lancing configuration, as well as the fuel analysis are presented below.

4.2.1 Horizontal industrial combustion kiln – 150 kW

Papers II and **III** are based on experimental data from the co-firing of hydrogen and coal in the HICK Unit located at the Research Institutes of Sweden (RISE) facility in Piteå, Sweden. An overview of the HICK Unit is presented in Figure 10. The maximum fuel capacity is 150 kW,

and the design replicates the combustion conditions of a rotary kiln. Several other studies have been conducted in this furnace[318,319].

The burner hood consists of a burner unit and a pre-heating unit. The pre-heating unit is designed to replicate the secondary air that is pre-heated by the cooler in a full-scale induration plant. However, HICK does not achieve the secondary air temperature of the full-scale unit, operating instead at a temperature of 850°C.

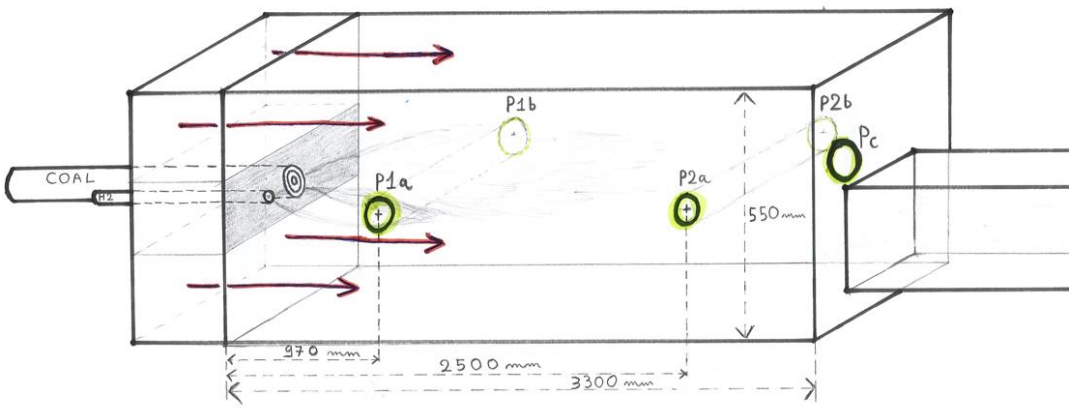

Figure 10. The HICK Unit; P1a, P1b, P2a, P2b are the measurement ports for spectroscopy, Pc is the optical port for the camera. This drawing is presented in Paper III.

4.2.2 Combi-burner design HICK

The work includes two HICK campaigns focusing on: 1) combi-burner configurations; and 2) lancing configurations. An overview to the evaluated combi-burner configurations is presented in Figure 11. The combi-burner evaluation includes designs for central and annular coal-feeding. The "O-" configuration features central coal injection and annular hydrogen injection. The "I-" configuration features central hydrogen injection and annular coal injection.

All the O-configuration designs have the same coal injection conditions with five distinct hydrogen injection configurations, designated as A, B, C, Dd, and Du, differing with respect to the number (velocity) and placement of injection points. All the configurations utilise holes with a uniform diameter of 2 mm.

In the I-design configurations, the annular coal injection is maintained for four distinct hydrogen inlet velocities, designated as A, B, C, and D. These velocities are achieved through a single hole with diameter ranging from 2 to 6 mm.

The operational conditions for these experiments are detailed in Figure 11 and Table 6.

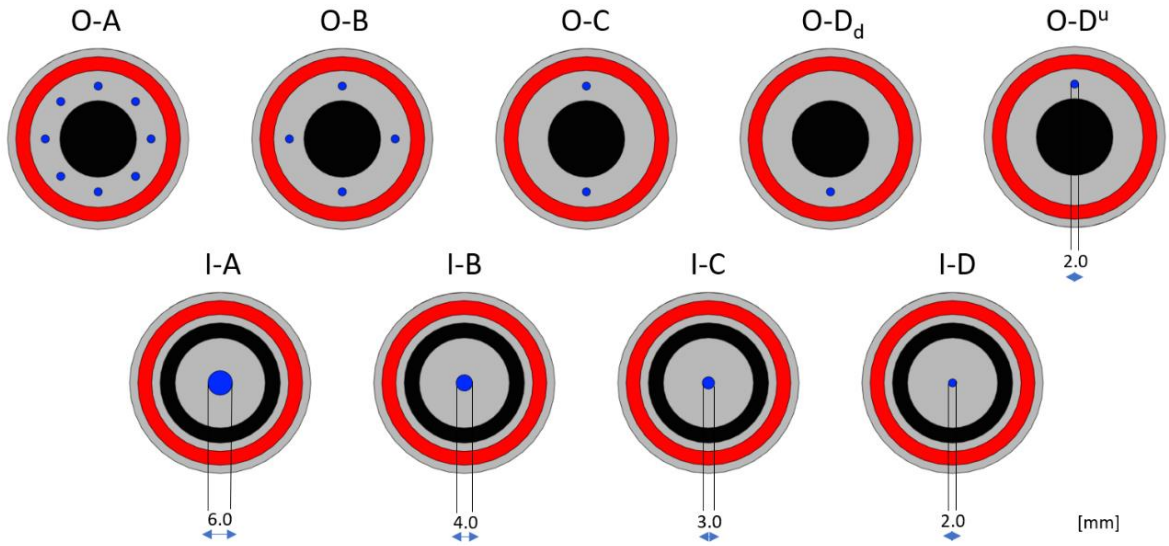

Figure 11. Various burner configurations, as observed from within the kiln. The regions marked in red denote the primary air inlets, while the blue regions indicate the points of hydrogen gas injection. The areas depicted in black represent the coal injection sites. In the O-type burners, coal is centrally injected, encircled by hydrogen injection ports and an annular primary air slit. Conversely, in the I-type burners, hydrogen is injected at the centre, accompanied by coal and primary air, which are introduced through annular slits that encircle the hydrogen injection site.

Table 6. Operational conditions of the HICK combi-burner.

	H_2		**Coal**		**H_2 + Coal**								
Burner	O-A	I-A	O-A	I-A	O-A	O-B	O-C	O-D$_d$	O-D^u	I-A	I-B	I-C	I-D
H_2 Velocity [m/s]	517	460	-	-	155	310	620	1241	1241	138	310	552	1241
Power [kW]	139 ± 0		128 ± 2		130 ± 1								
Power H_2 [kW]	139		0		41								
Power coal [kW]	0		128 ± 2		89 ± 1								
Feeding rate coal [kg/h]	0		15.1 ± 0.2		10.5 ± 0.1								
Transport air [dm^3/s]	0		3.33		2.50								
Secondary air [dm^3/s]	6.67		6.67		6.67								
Preheated air [dm^3/s]	106 ± 2		106 ± 2		106 ± 2								
Lambda	3.6		3.6		3.6 ± 0.1								

4.2.3 Lancing design HICK

A total of eight distinct lancing configurations were evaluated and compared against the pure coal cases and a reference hydrogen-coal combi-burner, designated as B_160_REF, which was previously utilised in the initial study and is referred to as 'O-A' in the present analysis. A summary of the experimental cases is provided in Table 7 and Table 8. The testing of all the configurations necessitated 3 days of measurements. Each experimental day commenced and concluded with the operation of a coal reference case, comprising 100% coal. These coal reference cases are labelled accordingly, for instance, for Coal_12, the initial numeral denotes the day (Day 1 in this instance) and the subsequent numeral indicates whether it is the starting or concluding reference ('2' signifies the ending reference).

Two primary lancing configurations were identified: a hydrogen lance-burner distance of 70 mm (designated as L) and a hydrogen lance-burner distance of 30 mm (designated as N). The distance refers to the measurement from the centre of the coal pipe to the centre of the hydrogen lance. The diameter of the coal pipe is 18 mm, so the distances of 70 mm and 30 mm correspond to 3.9-times and 1.7-times the diameter of the coal pipe, respectively. Furthermore, the hydrogen inlet velocities were tested within a range of 140– 1,240 m/s. Additional configurations included hydrogen lances angled towards the coal burner at 15° (designated as V) and lances inserted into the furnace to a depth of 100 mm (designated as I).

Table 7. Summary of the lance-burner configurations evaluated during the experimental campaign and in the reference combi-burner.

Co-firing configurations	Velocity (m/s)	CC*	Case nomenclature	Comments
B** 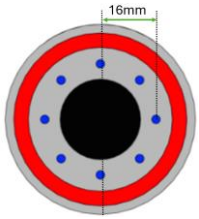	160	-	**B_160_REF**	Reference combi-burner
N** 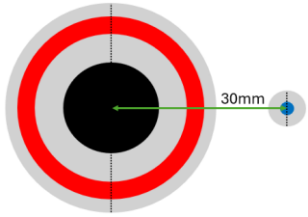	140	0.592	**N_140**	
			N_140_I	100 mm inside the furnace.
			N_140_V	At an angle of 15° to the coal flow.
	550	1.046	**N_550_V**	At an angle of 15° to the coal flow.
	1,240	5.262	**N_1240**	
L** 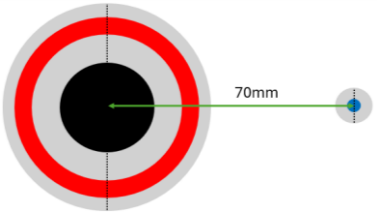	140	0.592	**L_140**	
			L_140_V	At an angle of 15° to the coal flow.
	1,240	5.262	**L_1240**	

*Craya-Curtet number calculated using the same method as described previously[320].

**The red regions correspond to the primary air inlets, the blue regions indicate the locations of hydrogen gas injection and the black region designate the coal injection.

Table 8. Illustration of the burner nozzles and specifications of the burner/lance flows. Designations: 1, Coal flow; 2, Primary air flow; and 3, Hydrogen flow.

100% Coal	**Co-firing -** Integrated burner B_160_REF	**Co-firing** – Burner Lance
	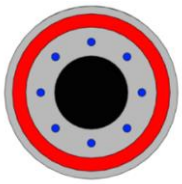	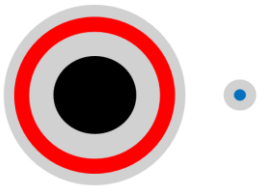
Black region: 15 kg/h coal + 200 lpm transport air. Red region: Primary air – 400 lpm.	**Black region:** 10.5 kg/h coal + 150 lpm transport air. Red region: Primary air – 400 lpm. Blue region: H_2 234 lpm (39 kW).	**Black region:** 10.5 kg/h coal + 150 lpm transport air. Red region: Primary air – 400 lpm Blue region: H_2 234 lpm (39 kW).

4.2.4 Fuel

The sub-bituminous coal used in the HICK was directly sourced from full-scale operations. The hydrogen had a purity level >99.9 vol.-%. The properties of hydrogen are presented in Table 9, while the proximate, ultimate, and calorific analyses of the coal are shown in Table 10, and the coal particle size distribution is shown in Figure 12.

Table 9. Properties of hydrogen.

Analysis	Unit	
Calorific value Hi/LHV	MJ/kg	118
Calorific value Hi/LHV	MJ/Nm^3	10.6
Density	kg/Nm^3	0.09
SAR (stoichiometric air ratio)	Nm^3/Nm^3 H_2	2.38

Table 10. Solid fuel proximate, ultimate, and calorimetric analyses.

Proximate analysis (as-received)	**Sub-bituminous Coal**	**Standard**
Moisture **(%)**	0.5 ± 0.05	ISO 589:2018 mod
Volatile matter **(%)**	19.2 ± 1	ISO 562:2010 mod
Fixed carbon* **(%)**	68.2 ± 5	ISO 562:2010 mod*
Ash **(%)**	12.1 ± 0.6	ISO 1171:2018
Ultimate analysis (as-received)		**Standard**
Cl **(%)**	< 0.01	ASTM D4208-2019 mod
S **(%)**	0.3	ASTM D4239-2018
C **(%)**	77.0	ASTM-D5373:2016
H **(%)**	3.9	ASTM-D5373:2016
N **(%)**	1.33	ASTM-D5373:2016
O* **(%)**	5.3	ASTM D3176-2015*
Calorimetric analysis (as-received)		**Standard**
Calorific value Hi/LHV (MJ/kg)	30.473	ISO 1928:2020

*Calculated by differences.

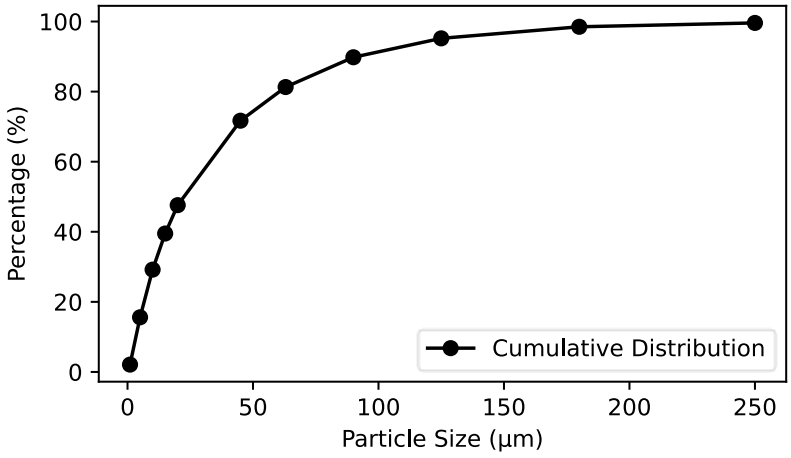

Figure 12. Coal particle size distribution.

4.3 Step 3: Up-Scaling and Demonstration

The developed technologies were scaled and demonstrated in the ECF Unit, a 580-kW unit with secondary air temperatures that reach 1,000°C and secondary air flows that simulate the turbulence patterns of full-scale units. Multiple burner designs, all sharing the same outer dimensions, were tested to facilitate rapid burner replacement and to reduce costs.

4.3.1 Experimental combustion furnace – 580 kW

The ECF is designed to replicate combustion conditions in both the GK and SG systems. A schematic representation is given Figure 13. Previous studies using this furnace have been published[321–323].

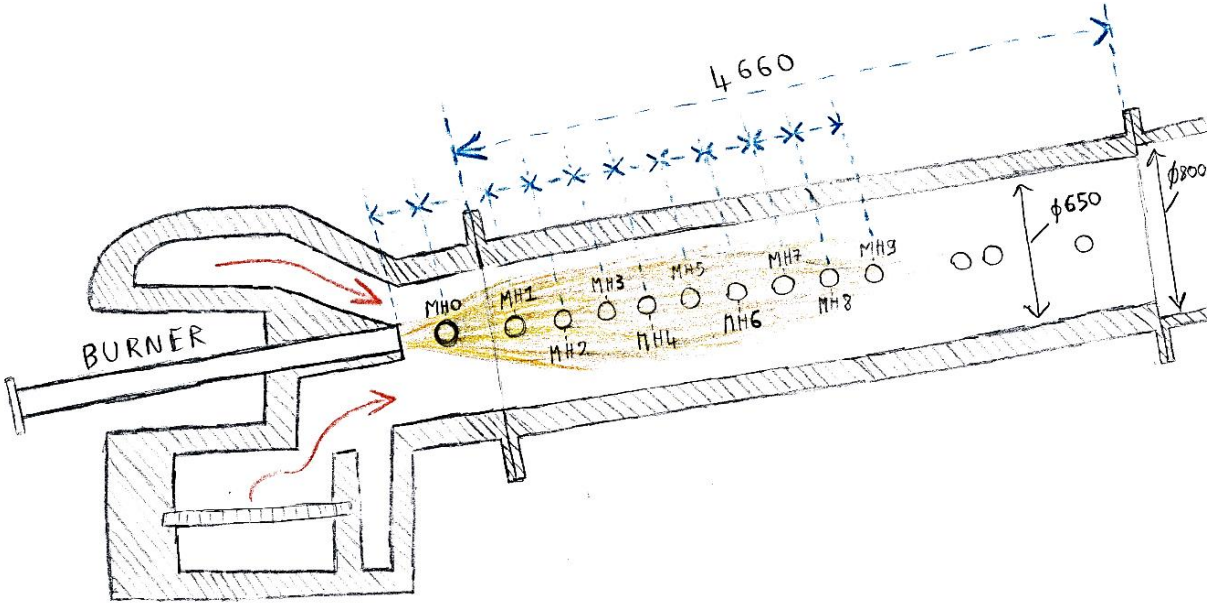

Figure 13. The ECF furnace. The measurements ports are labelled from MH0 to MH9. The first section is 650 mm in diameter and 4,660 mm in length, corresponding to the down-scaling of the kiln. Sections 2 and 3 (not shown) are each 800 mm in diameter. The kiln is angled by 3% in alignment with the burner. The secondary air flow comes from the upper and lower sections, simulating the secondary flow in a full-scale kiln.

The ECF features two inlets for hot secondary flows, which, in full-scale operations, are sourced from the cooler. Hot air is generated in an air pre-heater, achieving a temperature that is consistent with that of the full-scale system, up to 1,150°C. In GK-mode, the heated air is introduced into the ECF both from above and below the burner. The scale factor utilised in the ECF is 7.7, indicating that all linear measurements are 7.7-times lower than those of one full-scale kiln. The total length of the ECF is approximately 14 m, including the chimney. It is divided into three sections, each measuring approximately 4 m. The first 4-m section is representative of the full-scale kiln. Furthermore, the ECF is raised at the outlet end, resulting in a tilt of approximately 3°, mirroring the orientation of the full-scale system.

The outer diameter of the steel shell of the ECF is 1,220 mm, with a uniform thickness of 10 mm throughout the kiln. The construction of the re-built section 1 includes, from the outer layer inwards, 20 mm of microtherm insulation, 110 mm of insulating brick, and 145 mm of castable material, giving an inner diameter of 650 mm. In contrast, the inner diameters of sections 2 and 3 are both 800 mm.

4.3.2 Properties of fuels

The sub-bituminous coal and the hydrogen qualities in the ECF are the same as those in the HICK Unit. The characteristics of the coal, including the chemical analyses and particle size distribution, are presented Table 10 and Figure 12, respectively.

4.4 Hydrogen Flame Diagnostics

For determining the temperature change in the hydrogen flame, some studies have found that OH* chemiluminescence can be used as indicator of temperature in a laboratory-scale system. To test this method using our current measurement devices, a laboratory set-up dedicated to optical measurements was employed, the configuration of which is presented in Figure 14. The experimental set-up incorporates a flat flame burner, specifically designed for methane, and a versatile burner that is capable of operating in both flat flame and diffusion flame configurations. The diffusion flame settings can be used for methane and hydrogen. The apparatus utilises a tuneable diode laser absorption spectroscopy (TDLAS) system for the measurement of the temperature of the H_2O, to compare with the OH* chemiluminescence and OH* absorption (BAS OH*). The set-up includes a broad-band lamp and two spectrometer channels within the ultraviolet-visible-near-infrared (UV-NIS) range. One spectrometer is configured to analyse the OH* absorption of the broad lamp signal, while the other is dedicated solely to the measurement of emission spectra. The emission and absorption measurement methods are scaled up in the ECF Unit, so as to compare the results for larger flames.

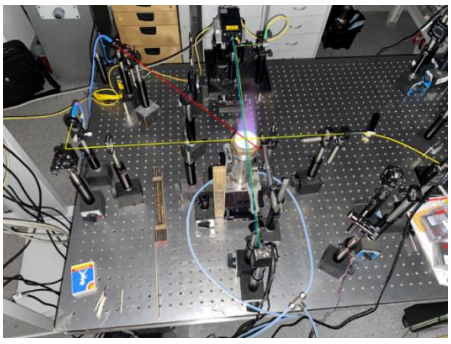

Figure 14. Overview of the laboratory set-up for the OH*-temperature measurement. The yellow line indicates the absorption path, the red line the emission line, the blue line the TDLAS CO_2, and the green line the TDLAS H_2O

4.5 Measurement Devices for Flame Characterisation

Table 11 provides an overview of the measurement devices used in this work, categorised into four groups: gas concentration, heat flux, video, and temperature measurements. The primary measurement methods are outlined briefly below, and references to more-detailed descriptions of each measurement technique are listed in Table 11.

4.5.1 Fourier-Transform Infrared Spectroscopy (FTIR)

Fourier-transform infrared (FTIR) spectroscopy is a multi-component analytical technique that quantifies gas concentrations by detecting infrared absorption at characteristic wavelengths. A broad-spectrum infrared beam is passed through the gas sample, with specific wavelengths being absorbed corresponding to the vibrational modes of the quantified molecule. A Fourier transform is then applied to convert the recorded signal into an absorption spectrum[324]. The gases measured in this study and their respective absorption wavelengths include: CO at 4.6 µm (2,170 cm^{-1}); CO_2 at 4.26 µm (2,349 cm^{-1}) and 15 µm (667 cm^{-1}); NO at 5.3 µm (1,887 cm^{-1}); NO_2 at 6.25 µm (1,600 cm^{-1}); SO_2 at 7.3 µm (1,370 cm^{-1}); H_2O at 2.7 µm (3,700 cm^{-1}) and 6.3 µm (1,590 cm^{-1}); NH_3 (ammonia) at 10.6 µm (943 cm^{-1}); and HCN (hydrogen cyanide) at 3.0 µm (3,333 cm^{-1}).

A key advantage of FTIR spectroscopy is its ability to measure simultaneously multiple gas species, including H_2O, with high sensitivity, making it particularly useful for complex gas mixtures, although it cannot measure O_2. However, FTIR systems are relatively expensive and require more maintenance than other gas analysis methods. Furthermore, they may exhibit sensitivity to interfering gases, potentially affecting measurement accuracy[325].

4.5.2 Non-Dispersive Infrared (NDIR) Spectroscopy

Non-dispersive infrared (NDIR) spectroscopy measures gas concentrations by detecting infrared absorption at specific wavelengths. Unlike FTIR, NDIR utilizes narrow-band infrared sources and gas-specific optical filters, enabling accurate and selective measurements[326,327]. Characteristic absorption wavelengths include: CO at 4.6 µm (2,170 cm^{-1}); CO_2 at 4.26 µm (2,349 cm^{-1}); NO at 5.3 µm (1,887 cm^{-1}); NO_2 at 6.2 µm (1,613 cm^{-1}); and SO_2 at 7.3 µm (1,370 cm^{-1}). Similar to FTIR, the NDIR method is limited to gases that exhibit strong infrared absorption and is not applicable to O_2measurement. However, NDIR offers high levels of accuracy and reliability, while requiring minimal maintenance.

4.5.3 Electrochemical Sensors

Electrochemical sensors quantify gas concentrations by detecting the reaction between the target gas and an electrode within an electrolyte solution, generating an electrical signal that is proportional to the gas concentration[328]. This method is cost-effective, compact, and offers a rapid response, making it particularly useful for quick measurements in challenging locations, such as the commercial TESTOS instrument. However, sensor performance degrades over time, necessitating periodic calibration. In addition, electrochemical sensors exhibit cross-sensitivity to other gases, which may interfere with measurement accuracy. Electrochemical sensors typically quantify gas-phase oxygen concentrations.

4.5.4 Paramagnetic Sensors

Non-dispersive gas analysers, which typically utilize paramagnetic methods, include the commercial MAGNOS instrument. The paramagnetic method leverages the unique magnetic properties of the measured component (typically O_2), where an external magnetic field induces gas movement, causing a detectable shift in the sensor[329]. While this method is highly robust, it can be sensitive to vibrations and temperature fluctuations.

4.5.5 Non-Dispersive Ultra-Violet (NDUV) Spectroscopy

Non-dispersive ultraviolet (NDUV) spectroscopy measures UV absorption at the characteristic wavelengths of the target species, i.e., NO (in the wavelength of 226 nm) and NO_2 (400 nm), as in the commercial instrument LIMAS. NDUV is highly efficient for measurements of high concentrations of NO. It offers high sensitivity and selectivity, and unlike NDIR, it is not affected by interference from water vapour, since water vapour is not affecting the UV spectra through absorption. However, the main limitation of NDUV spectroscopy is that it can only measure gases that absorb in the UV range, which requires a reliable UV light source and a robust calibration system.

4.5.6 Tuneable Diode Laser Absorption Spectroscopy (TDLAS)

TDLAS is a technique for measuring gas concentrations and temperature of the measured component. In this study, it has been applied to detect H_2O in the flue gases. The method involves directing a laser beam at a specific wavelength through the flame, where the target gas molecules absorb light according to their unique absorption spectra. By tuning the diode laser to these absorption lines and analysing the transmitted light intensity, the gas concentration is determined using the Beer-Lambert law.

To enhance sensitivity and reduce noise, a wavelength modulation spectroscopy set-up is employed. This approach enables real-time, non-intrusive monitoring of combustion processes. Details of the methods used in this work can be found elsewhere[330].

4.5.7 Broadband Absorption Spectroscopy (BAS)

The broadband absorption spectroscopy (BAS) technique typically measures in-flame OH-concentrations. This method involves directing a broadband light UV source through the combustion zone, where OH radicals absorb light (mainly the peaks at 306.7 nm and 309.2 nm). The absorption spectrum is then analysed to determine the OH concentration and temperature.

4.5.8 Emission spectroscopy in UV and VIS

Emission spectroscopy measures the temperatures from the radiation of solid surfaces, such as coal and soot particles or furnace walls, as well as from the electronically excited state of OH. The temperatures of solids are determined by fitting the measured spectra to Planck's law, while excluding spectral regions that are affected by absorption from gases, such as CO_2 and H_2O. The coal particles, soot, and furnace walls are assumed to exhibit blackbody-like behaviours. The method for extracting temperature from the OH* emission spectra is less mature and is discussed in more detail in the *On-going work* section.

4.5.9 IFRF Total heat flux and radiative heat flux

The IFRF total heat flux probe measures the combined heat transfer from radiation, convection, and conduction, although conduction is negligible in combustion systems. The probe is positioned at the furnace edge to capture the thermal conditions affecting the wall or bed. The probe consists of a stainless-steel plug with two Type K thermocouples placed at a known distance apart, to determine the axial temperature gradient and the resulting heat flux.

In the IFRF radiative heat flux probe, an ellipsoidal radiometer quantifies the radiative heat transfer across all wavelengths. The probe is positioned at the furnace shell to assess the radiative heat received by the wall or bed. While traversing the flame with the probe is possible, this was not performed in this study.

4.5.10 Cameras

In this study, several different cameras in the visible light (VIS) spectrum are used to record the flames. Video analyses are used to quantify flame properties, such as flame area, intensity profiles, grey scale, contrast, and stability. The method is described in detail in **Paper III**.

Table 11. Summary of measurement devices used in the experimental campaigns.

Type of measurement	**Technology**	CHALMERS	HICK	ECF	FULL-SCALE	LAB	Method
Gas concentration	FTIR - H_2O, CO_2, CO, NO, NO_2	X	X	X	X		FTIR - Fourier-transform infra-red spectroscopy - Method[331]
	MRU Air MGA Prime - O_2, CO_2, CO, NO, NO_2		X				NDIR (non-dispersive infra-red spectroscopy) for CO_2, CO, NO, NO_2; Electrochemical O_2Sensors
	Testo 350 - O_2, CO_2, CO, NO, NO_2		X				NDIR (CO_2), Electrochemical sensors for O_2, CO, NO, NO_2.
	NGA analyser – O_2	X					Non-Dispersive Gas Analyser – O_2 concentration
	URAS (CO, SO_2, CO_2, O_2) MAGNOS (O_2) LIMAS (NO, NO_2)			X			URAS: NDIR for CO, SO_2, CO_2; Electrochemical O_2 sensor. MAGNOS: Para-magnetic O_2 sensor LIMAS: NDUV – Ultra-violet detection of NO and NO_2 .
	TDLAS – H_2O		X			X	H_2O concentration and H_2O temperature - Method[332,333]
	TDLAS – O_2			X			Method[334]
	Spectrometer Ocean Optics HR6XR300-10 + broad lamp			X		X	OH* absorption (BAS)[335]
Heat flux	Total Heat Flux – IFRF		X	X			Total heat flux at the edge of the wall (w/m^2)
	Radiative Heat Flus – IFRF			X			Radiative heat flux at the edge of the wall (w/m^2)
Video analysis	iPhone camera	X					Flame visualisation
	Samsung S22 S901B Camera		X				Flame visualisation, flame stability
	Allied Vision Prosilica GT1910 monochrome CCD camera		X				Flame visualisation, flame area, stability, flame contrast, flame grey Methods in **Paper II**
	Full scale camera				X		Flame visualisation
	FORGE 5GigE - FG-P5G-50S4C-C			X			Flame visualisation, flame area, stability, flame contrast, flame grey
Temperature	Spectrometer - Ocean Optics HR2000+GC		X	X			Coal particle temperature, Soot temperature - Method[318,336]
	Spectrometer – Ocean Optics HR6XR300-10			X	X	X	Coal particle temperature, Soot temperature - Method[318,336] Scaling up the method for OH* temperature under development
	Suction pyrometer	X		X			Method[337]

5 Flame characteristics during co-firing

This chapter examines the changes in flame characteristics when co-firing solid and gaseous fuels, compared to combustion processes with 100% solid fuel and 100% gaseous fuel. The findings are presented in three main sections. Step 1 (**Paper I**) explores the evolution of flame behaviour when shifting from gaseous to solid fuels, using lignite and propane. Step 2 (**Papers II** and **III**) expands the investigation to the co-firing of sub-bituminous coal and hydrogen, assessing the influences of burner configurations and injection parameters. Finally, full-scale observations provide insights into the behaviours of coal and oil flames under industrial operational conditions.

5.1 Step 1: Co-firing Lignite and Propane (Paper I)

Gaseous fuels exhibit higher reactivities than solid fuels, leading to more-intense and compact flames. In contrast, solid fuels require additional time to undergo drying, devolatilisation, and combustion of both volatiles and char. The experiments conducted for **Paper I**, using lignite and propane, analysed the flame transition across 0-100% lignite-to-propane ratios. Figure 15 presents the average intensity recorded on videos with thresholds for the 10% and 1% highest intensities of a lignite, a mixture of (50% lignite and 50% propane) and a propane flame, respectively. The mixture of lignite and propane more closely resembles a lignite flame than a propane flame. The intense combustion zone is near the burner – where volatiles release is most significant – similar to that of lignite but even more pronounced. This aligns with the in-flame measurements of HCN presented in **Paper I**. The propane flame shows a much later high-intensity flame compared to lignite. Observations made during the campaign indicate that as propane is gradually replaced by lignite, the flame structure rapidly transitions to the geometrical characteristics of a solid-fuel flame (defined here as the visible light emitted by the flame), accompanied by a notable reduction in temperature. Overall, the lignite flame exhibits a broader, less-distinct, and more-fluctuating structure than the sharper, more-compact propane flame. It is noteworthy that the pure lignite flame reveals significantly more visible lignite particles than the mixture of lignite and propane flame.

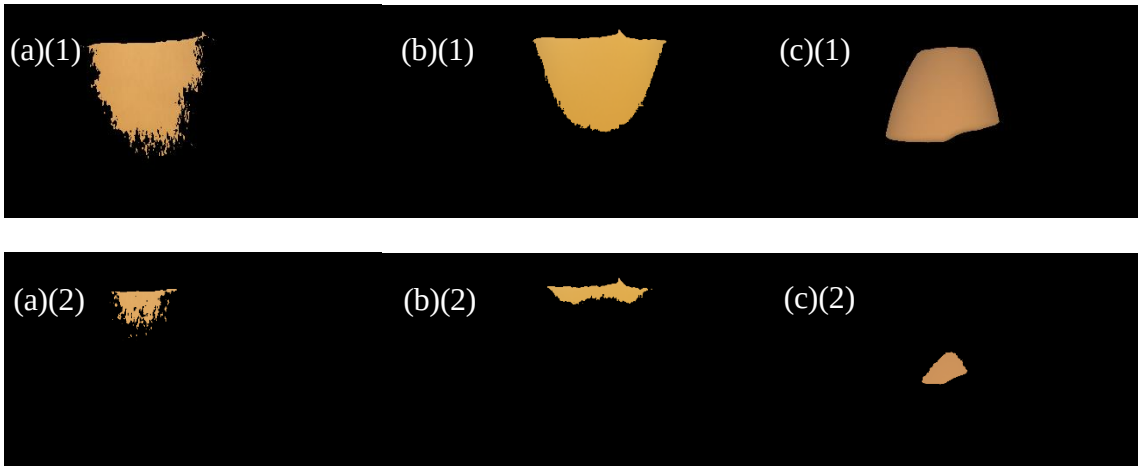

Figure 15. Representative images acquired at port M2 with a threshold at 5% (.1) and 1% (.2) highest-intensity pixels: (a) lignite; (b) 50% lignite and 50% propane; and (c) 100% propane.

Figure 16 presents the in-flame O_2 and CO concentrations for three fuel compositions: 100% lignite; 50% lignite and 50% propane; and 100% propane. Despite the geometric and thermal changes, the in-flame O_2 and CO concentrations maintain a gaseous flame-like distribution, although they appear more dispersed and less well-defined. The spatial distributions of these gases reveal significant differences in combustion characteristics. In the 100% lignite flame, the CO concentrations are relatively low, forming in two localised zones approximately 10 cm from the flame centre-line, each extending 30 cm in length, with a peak CO concentration of 1.7%. In the 100% propane flame, CO formation is more centralised, occurring in a zone that is 70 cm long and 10 cm wide, with a significantly higher peak CO concentration (10.2%).

The O_2 concentration profiles differ between the flames. The combustion of 100% propane creates a large region that is characterised by oxygen deficiency, extending 10 cm in width and persisting up to 80 cm from the burner. The propane flame O_2-lean region almost disappears for the case of co-firing, along with a much larger zone of O_2 concentration >5%. The pure lignite flame presents a large, high-O_2 concentration zone at the centre with no O_2-lean regions. The lowest O_2 concentration is detected at around 10 cm from the centre.

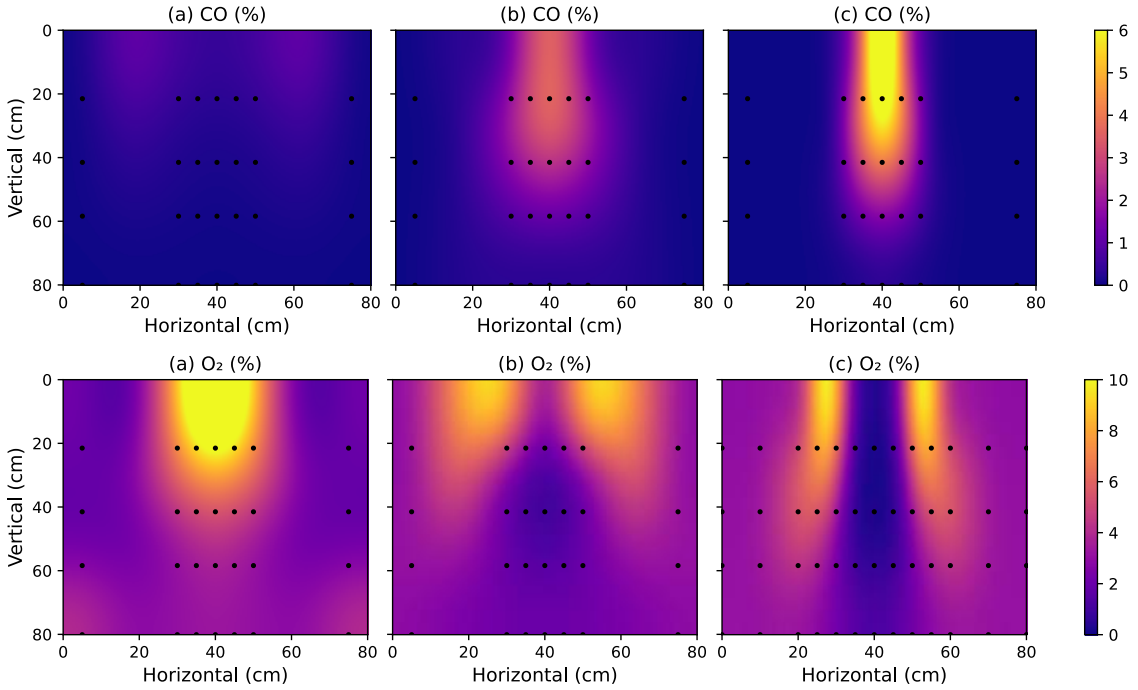

Figure 16. Measurements of CO (%) and O_2 (%) in the: (a) 100% lignite flame; (b) 50% lignite and 50% propane flame; (c) 100% propane flame.

5.2 Step 2: Co-firing Sub-bituminous Coal and Hydrogen (Papers II & III)

Building upon the findings of **Paper I**, **Papers II** and **III** investigate the co-firing of sub-bituminous coal (low volatile matter content of <20%) and hydrogen. Consistent with the findings of **Paper I**, the general observations from the HICK Unit indicate that the coal flames exhibit a less-compact structure, reduced brightness, and greater fluctuations compared with the co-firing scenarios, as supported by the TDLAS H2O readings, as well as visual assessments from the cameras, total heat flux probe, and spectrometers.

Nevertheless, a more-detailed examination reveals that the method of hydrogen injection into the coal, along with the velocity of the injection, plays a critical role in determining the characteristics of the flames. In the context of a combi-burner, an increase in the velocity of the hydrogen results in an increase in flame intensity and a reduction of the flame's cross-sectional area. The increased velocity of the hydrogen likely enhances turbulence within the fuel jet, thereby improving mixing with the surrounding hot secondary air-flow and leading to an increase in combustion intensity. Furthermore, an increase in the hydrogen velocity beyond 621 m/s correlates with an extension of the flame length and/or a delay in the ignition process compared to lower velocities, as evidenced by the TDLAS H2O measurements (vol-%).

In the context of hydrogen lancing, when the hydrogen lance is positioned 30 mm from the coal burner an increase in hydrogen velocity concomitantly reduces the area of the flame by 51%.

However, at a greater distance of 70 mm, the influence of hydrogen velocity on the coal flame area is markedly diminished, with a 36% reduction of the flame area. This may be attributed to reduced interactions between the coal and the hydrogen flames. Furthermore, angling the hydrogen lance directs the hydrogen closer to the coal burner, resulting in an even greater expansion of the flame area, with an 85% increase for the N_140_V compared to the N_140 configuration and a 49% increase for the L_140_V compared to the L_140 configuration.

During the combi-burner campaign in the HICK Unit, the flames were not documented using a CMOS camera; instead, recordings were made with a mobile phone, which also captured videos on the first day of the lancing campaign. The variability in positioning and limitations related to controlling the mobile phone's camera settings preclude a comprehensive comparison of all the visual parameters between the lancing and combi-burner methods. Figure 17 illustrates the coefficient of variation of the flame area obtained from the mobile phone video recordings for the combi-burner campaign, including the co-firing cases and reference coal case, together with three additional cases from the lancing campaign with the B_160_REF, L_1240, and N_1240 configurations. In addition, the figure presents data from the CMOS camera for all the lancing configurations, along with their corresponding reference cases (B_160_REF) and the coal reference cases. The stability of the flame, as indicated by the coefficient of variation of the flame area, demonstrates a strong correlation between the data collected using the mobile phone and the data obtained with the CMOS camera for the following cases: B_160_REF, L_1240, and N_1240. Therefore, the data obtained from the mobile phone are considered valuable for further analyses.

Pure coal cases exhibit significantly greater instability than co-firing cases. However, during the final days of the lancing campaign, the furnace temperature distribution was notably higher, resulting in considerably lower instability than in the other pure coal cases. In cases of co-firing, increasing the velocity in both the combi-burner and lancing configurations typically leads to a decrease in stability. The lancing configurations show the most significant changes, with instability increasing by 94% between L_1240 and L_140, and by 178% between N_1240 and N_140. However, the combi-burner O-A case bucks this trend, which may be explained by periods of great instability in the coal flow from the feeder during the filming. For lancing, an increase in distance from the coal burner similarly diminishes the stability by 243% for the low-velocity (L_140 versus N_140) and by 140% for the high-velocity (L_1240 versus N_1240) cases. Notably, the high-velocity setting of L_1240, when applied at a greater distance, approaches the stability threshold characteristic of a pure coal flame, which is recognized as the least-stable configuration in co-firing scenarios. In contrast, the N_140_V configuration exhibits

the highest stability, closely followed by the low-velocity combi-burner. Furthermore, preliminary observations suggest that the I-burner, which incorporates hydrogen injection at its centre, exhibits marginally superior stability compared with the O-burner configuration.

Overall, the results from **Papers II** and **III** indicate that co-firing, as compared to using 100% coal, enhances the combustion efficiency for both the lancing and combi-burner techniques. This improvement is reflected in lower CO concentrations in the exhaust, brighter and more stable flames (as observed in the video analysis), and more-defined combustion under co-firing conditions. Furthermore, for the lancing method, the spectrometer measurements show a significant increase in coal temperature at port 1, along with earlier ignition timings.

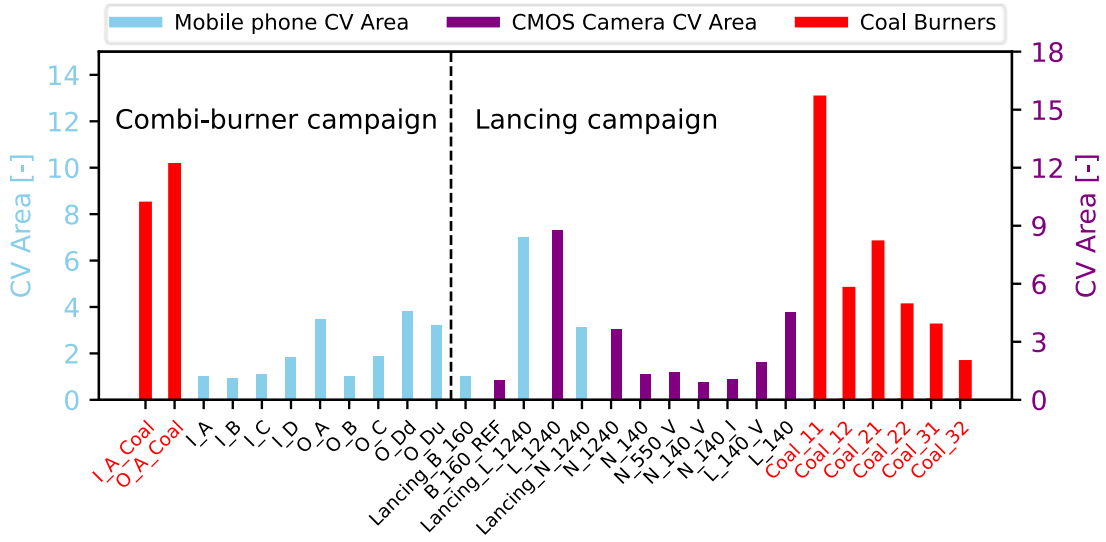

Figure 17. Coefficient of variation of the area of the flame as a function of the burner/lance configuration. The pure coal cases were performed both in the combi-burner campaign (indicated in red on the left-hand side of the plot) and in the lancing campaign (indicated in red on the right-hand side of the plot).

5.3 Full-Scale Observations: Coal and Oil Flames

During full-scale operations, coal is used for approximately 80% of the time, while oil is utilised for the remaining 20%, primarily during the warming-up and cooling-down phases of the process. There are also instances of co-firing, where both oil and coal are used simultaneously. Figure 18 and Figure 19 display averaged images of coal flames, from a 50% coal and 50% oil mixture and from a pure oil flame, for two different plants. A threshold of 2% of the maximum intensity is applied, as lower intensity thresholds tend to capture reflections from the materials inside the kiln. The area (in pixels) is calculated based on this 2% intensity threshold. It is evident that oil exhibits significantly higher intensity than coal, and this is particularly noticeable for the co-firing conditions, where only the oil area is visible (2). Spectrometry measurements, indirectly

measuring soot temperature and particle temperatures for both the oil and coal, further support this observation, showing average increases of 106°C and 145°C between the oil soot and coal particles in the respective plants 1 (Figure 18) and 2 (Figure 19). Coal displays a central zone of low intensity compared to oil, a phenomenon that is especially pronounced in Plant 2. As anticipated, the oil flame is notably shorter than the coal flame, with this difference being particularly evident in the second plant, especially under co-firing conditions.

Overall, coal flames are more diffuse and less intense than oil flames. The turbulence appears to alter the flame shape between the two plants, with the Plant 2 exhibiting much-straighter flames, especially when using oil, as compared with Plant 1. It must be mentioned that in the case of co-firing hydrogen and coal, if the observations from Step 2 persist when scaling up to full scale, an intensified zone at the front of the coal flame would be expected. In this case, the flame would resemble the current oil flame more closely than the coal flame.

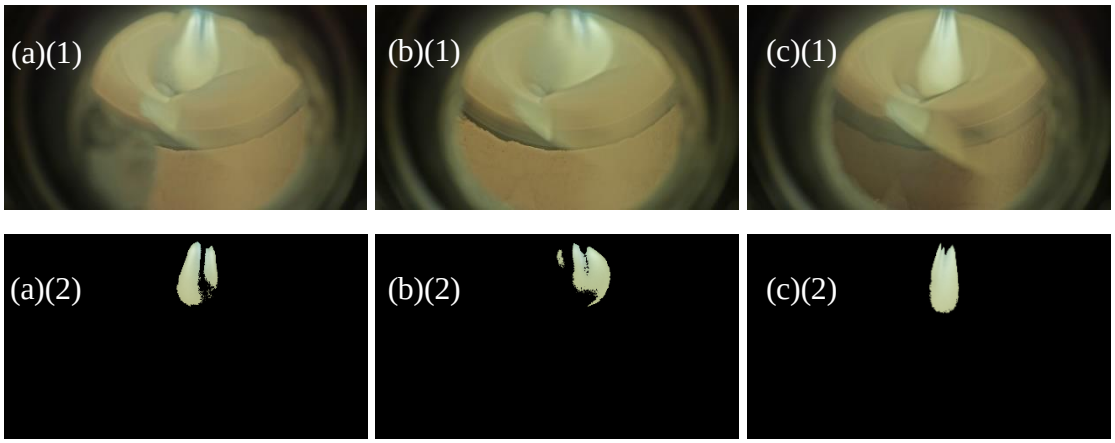

Figure 18. Average images (1) and intensity thresholds at 2% (2) of the highest intensity in Plant 1. The first panel is 100% coal (a), the second panel is 50% coal and 50% oil (b), and the third panel is 100% oil (c).

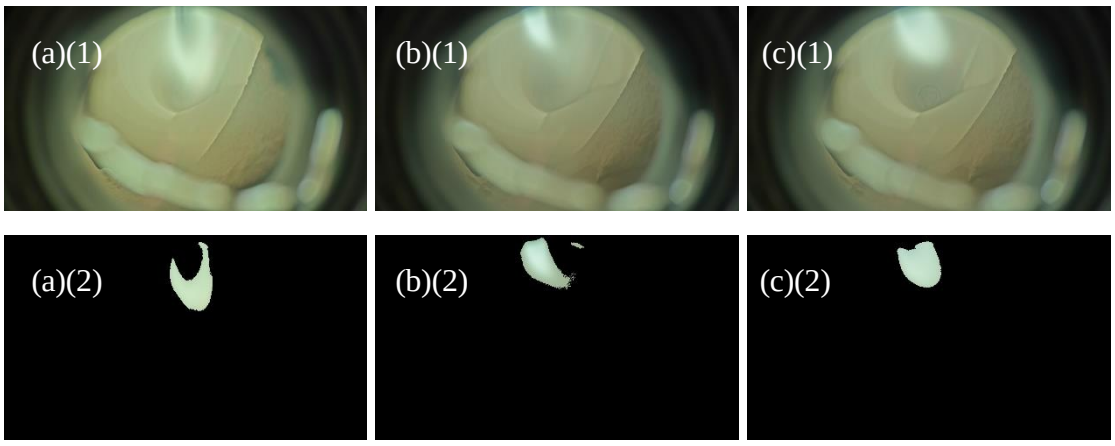

Figure 19. Average images (1) and intensity thresholds at 2% (2) of the highest intensity in Plant 2. The first panel is 100% coal (a), the second panel is 50% coal and 50% oil (b), and the third panel is 100% oil (c).

6 NO_x Formation during Hydrogen-Coal Co-firing

This chapter explores the changes in NO_x formation when co-firing solid and gaseous fuels, in comparison to combustion with 100% solid or 100% gaseous fuels. The results are organised into three main sections, in the same order as presented previously. In Step 1 (**Paper I**), the investigation focuses on the variation of outlet NO_x emissions as the fuel mixture transitions from 100% gaseous fuel to 100% solid fuel. In addition, the study quantifies the respective contributions of Fuel-NO and thermal-NO using a model for both gaseous and solid fuels, and concludes with an analysis of the impact of early volatile release on outlet NO emissions. Step 2 (**Papers II** and **III**) assesses the NO_x emissions from two injection methods, emphasising the effects of velocity and injection distance, particularly the distance between the coal and hydrogen injections for the lancing method. As a final point, measurements from the NO_x outlet in full scale for both coal and oil are discussed, with the focus on assessing one primary measure to reduce NO_x in coal flames.

6.1 Step 1: Co-firing Lignite and Propane (Paper I)

In **Paper I**, it is observed that the concentration of NO in the exhaust increases with the use of a higher proportion of lignite relative to propane. Figure 20 presents the results for the NO increase as a function of Fuel-N input, comparing both the modelling and experimental findings. When the model is run without HCN (Fuel-N), NO is primarily formed by thermal-NO while it is assumed that any additional NO observed in situations where HCN is added to the PFR is either directly or indirectly attributable to the addition of HCN, as no other parameters are being altered. Consequently, the additional NO is considered to result from the presence of Fuel-N.

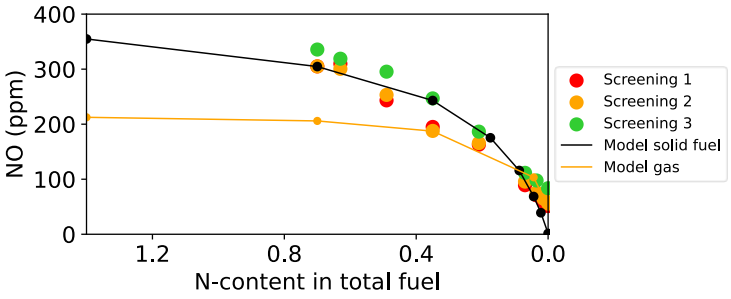

Figure 20. Concentration of NO as a function of the N-content of the fuel mixture (both experimental and modelling data are used).

Notable discrepancies between the modelling and experimental results are observed. In the experimental set-up, as the level of Fuel-N increases, the temperature and mixing profiles change, whereas in the modelling, both variables remain constant. The model indicates that, under constant conditions, Fuel-NO becomes dominant as the Fuel-N input increases. For a 100% lignite setting, which corresponds to a Fuel-N content of 0.7% by mass, the partitioning of thermal-NO and Fuel-NO is as follows: 75% of the outlet NO is formed due to the presence of HCN in the gas model, while in the solid fuel model, where the temperature profile is significantly lower, 99.6% of the NO is attributed to Fuel-N. In absolute terms, the solid fuel model generates substantially more NO than the gas model, due to a much higher O_2 concentration caused by a faster mixing profile. A sensitivity to temperature analysis shows that with an increase of 100°C, Fuel-N responsibility for NO formation decreases to 32% for the gas model, while it remains virtually unchanged at 99.5% for the solid fuel model. In addition, a sensitivity analysis was conducted in relation to the forms of nitrogen added, comparing injections of HCN and NH_3. The results, as presented in **Paper I**, indicate that the trends are consistent across both forms of nitrogen for the gas model. However, at the lower temperature profile that is characteristic of the solid fuel model, NH_3 results in a significantly higher NO concentration in the outlet, as compared to HCN.

Three key measured parameters, along with one indirectly measured factor, influence the level of NO formation during the transition from a propane flame to a lignite flame. The level of Fuel-N, the flame temperature and the O_2 in-flame concentration.

Concerning the Fuel-N, replacing propane with lignite leads to a logical decrease in the flow of Fuel-N. Figure 21 shows how the relative increase in outlet NO per amount of Fuel-N added in the solid fuel model, i.e., Figure 20 is basically the gradient of the black line in Figure 22. Note that only the input HCN is increased while the propane flow, temperature, and mixing profiles remain constant. The results reveal that the addition of HCN (Fuel-N) to propane gives a non-linear increase in outlet NO, which reflects the inhibiting effect of NO on Fuel-N oxidation to NO, mainly through the determining N oxidation through the reaction $N+NO=>N_2+O$. In conclusion, a small amount of Fuel-N increases significantly the NO formation, while further addition of Fuel-N provides less extra NO formation. The rate of NO increase as a function of the Fuel-N intake is asymptotic.

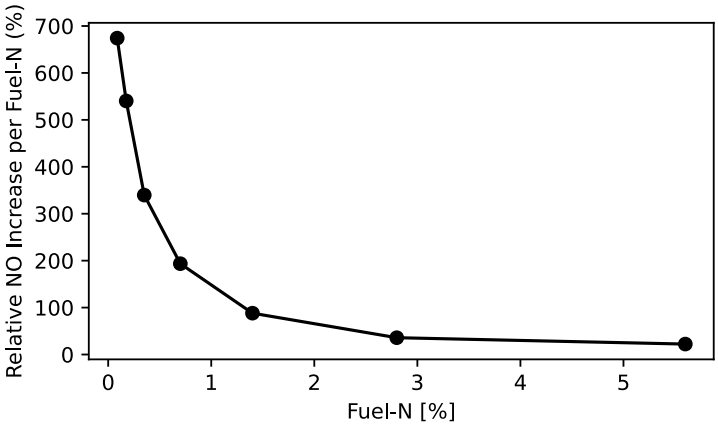

Figure 21. Relative outlet NO as a function of Fuel-N introduced into the model (ppm/%Fuel-N).

Concerning the in-flame temperature, it is observed that in-flame temperature decreases as the lignite-to-propane ratio increases, as measured with a suction pyrometer. This higher temperature along the replacement of lignite by propane is likely to accelerate the heating rate of the lignite particles during co-firing, promoting the release of Fuel-N in the volatiles and leading to earlier ignition. Finally, the in-flame O_2 concentration increases with the rising lignite-to-propane ratio, as discussed in the previous section. The overall higher O_2 flame concentration creates an oxidizing environment in the presence of both nitrogen and high temperatures, leading to a larger flame volume associated with NO formation.

Figure 22 illustrates the spatial change in NO concentration in the centre plane, determined from in-flame NO measurements conducted in the Chalmers experimental furnace. This change, expressed in parts per million per square centimetre (ppm/cm²), is used to define the region of NO formation.

The first general observation is that the maximum rate of increase becomes significantly higher with increasing proportion of lignite. For the three cases, the highest rate of NO increase is observed in the richest O_2 zone.

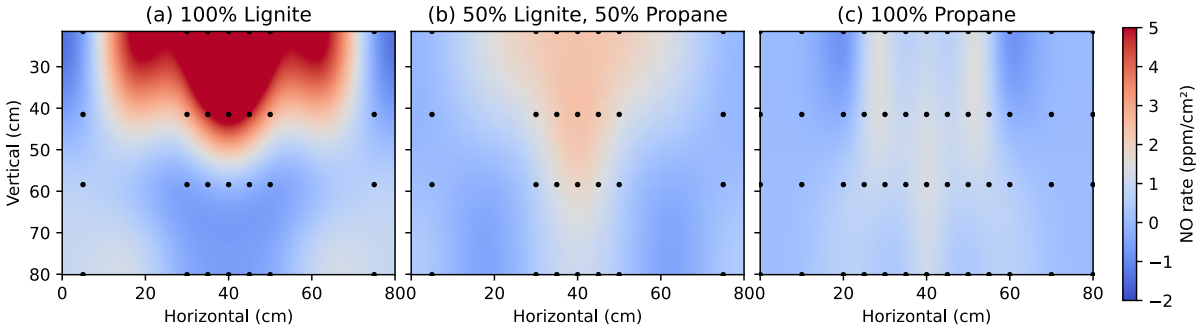

Figure 22. Rates NO increase in flames generated with: (a) 100% lignite; (b) 50% lignite and 50% propane; and (c) 100% propane.

The NO formation zone exhibits not only a higher rate of NO increase in the lignite flame, but also a significantly larger area than the propane flame. Estimations of areas were done using three thresholds, specifically, rates exceeding 1 ppm/cm^2, 2 ppm/cm^2, and 3 ppm/cm^2. The results are illustrated in Figure 23. Notably, the area associated with a rate greater than 1 ppm/cm^2 decreases by 8% in the co-firing case, as compared with a pure lignite flame, whereas it diminishes by 43% in a pure propane flame. At the threshold of 2 ppm/cm^2, transitioning from lignite to a mixture of 50% lignite and 50% propane results in a 36% reduction in surface area, while further transitioning to pure propane yields a substantial decrease of 91% in surface area.

Although the peak combustion temperature is lower for the lignite flame compared to the propane flame, the trend in formation of thermal-NO may not follow the exponential decrease along the temperature. The magnitude of the increase in partial pressure of O_2 in high-temperature zones may limit the decrease of thermal-NO. In other words, the maximum rate of thermal NO formation may be lower for the lignite flame then for the propane flame, although the region in which thermal NO_x are formed is larger.

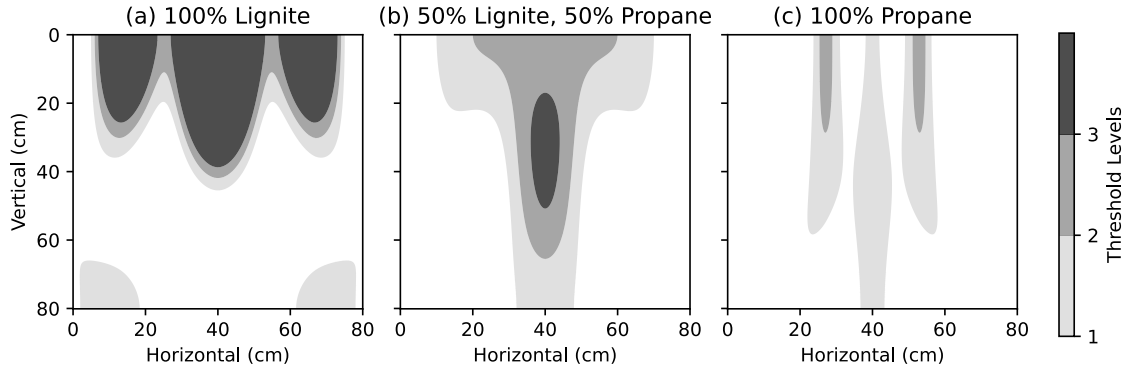

Figure 23. Rates of NO formation at three threshold rates (in ppm/cm^2): >1; >2; >3; and >5. The *x*-axis is the diameter of the furnace, while the *y*-axis is the vertical length from the burner head to the latest in-flame measurements.

6.2 Step 2: Co-firing Sub-bituminous Coal and Hydrogen (Papers II & III)

In **Papers II** and **III**, the results shows that the presence of hydrogen can both increase and decrease NO_x emissions in the outlet compared to a pure coal flame. The pure coal flame shows NO_x emissions in the range of 831–976 mg/MJ, while the combi-burner has NO_x emissions in the range of 517–688 mg/MJ, and the lancing method lands in the range of 846–1,739 mg/MJ, showing large fluctuations in the function of the hydrogen injection method. The combi-burner shows the lowest emissions, while the lancing method can at best lie in an emissions range similar to that of a pure coal flame.

The combi-burner method demonstrates on average a 48% decrease in NO_x emissions relative to the lancing technique. The lancing method reveals that the proximity of hydrogen injection to the coal significantly influences NO_x emissions: closer injection corresponds to a 44% reduction in NO_x levels for the low-velocity cases while the reduction in NO_x levels for the high-velocity cases is only 9%. While injection velocity plays a critical role in the lancing method, its effect is less pronounced in the combi-burner. In the context of the combi-burner, a decrease in injection velocity correlates with reductions in NO_x emissions of 13% for the O- design and 9% for the I-design. In the lancing method, when the hydrogen lance is positioned near the coal burner, a decrease in velocity also leads to a 21% decrease in NO_x emissions, consistent with the outcomes observed in the combi-burner. However, when the hydrogen lance is located further away from the coal, the lowest level of NO_x emissions (a decrease of 22%) is observed at the highest injection velocity.

The effect of angling by 15° the hydrogen lance towards the coal flame helps to decrease further the NO_x emissions, particularly for the L_ case (32% reduction), while the N_ case shows a reduction of only 2.5%.

The presence of hydrogen may impact the coal flame in several ways. Due to its fast reaction, it consumes an amount of O_2 in an early stage of the overall flame (hydrogen plus coal case), creating a reduction zone, thereby limiting locally the rate of NO_x formation from the Fuel-N. In the case of the combi-burner, this reduction zone is directly implemented in the coal flow, increasing the efficiency of limiting NO_x formation, whereas in lancing, the O_2-lean zone is moved to the side and is likely to be less integrated into the coal flow, thereby limiting its positive impact.

Furthermore, the increase in temperature of the coal particles when hydrogen is present (measured by spectrometry and the flame intensity measured using cameras) demonstrates that a quantity of energy from the hydrogen flame is transferred to the coal particles, diminishing the peak temperature of the hydrogen flame, and thereby diminishing the formation of thermal-NO.

Finally, the early combustion of hydrogen is believed to increase the rate of the temperature increase of the coal particles, helping releasing more Fuel-N in the volatiles. As discussed earlier, an increasing rate of coal particle temperature is an effective primary measure to decrease the overall NO_x.

It is worth mentioning here the scenario in which hydrogen is injected far from the coal burner. Unfortunately, during the experiments, the hydrogen flame was not visible, making it impossible

to confirm definitively that there was complete separation of the coal and hydrogen flames. However, it is hypothesised that the flames, if not entirely disconnected from the coal flame, are predominantly burning in parallel locations. This assumption is supported by the measured behaviours of the coal flames in the L_ lancing configuration, which exhibits characteristics that more similar to those of pure coal flames than to those in the N_ cases (except for the angled one that directs hydrogen closer to the coal). The potential for flame separation is considered to represent the worst-case scenario for overall NO_x emissions. The overall higher NO_x emissions are believed to arise from increases of both thermal-NO and Fuel-NO. The hydrogen flame, transferring significantly less heat to the coal particles, increases its peak temperature, thus enhancing thermal-NO formation, while the coal flame is less well-promoted, releasing less Fuel-N in the volatiles and also increasing its in-flame O_2 concentrations. This theory of NO_x increase in conditions of double flames is supported by the full-scale data analysis.

Co-firing has been investigated at full scale with the current fuels: coal and heavy oil (EO5). It has been established that emissions of nitrogen oxides (NO_x) are significantly higher when coal is used compared to EO5. While further investigation with higher-quality measurements is necessary to validate these observations, some insights can be deduced. Oil is believed to contribute mainly to thermal NO_x due to its higher flame temperature (higher intensity from the video analysis), and a significantly lower Fuel-N content of around 0.1%–0.2%-mass. However, the NOx emissions associated with co-firing are influenced by the specific configuration of the burner. Figure 24 shows photographic images of a co-firing flame with 50% oil and 50% coal (power-based) for three plants. In two plants, a single flame is observed and the resulting NO_x species are comparable in behaviour to those seen in propane and lignite, as in **Paper I**, with a linear trend along an increasing coal:oil ratio. In the third photograph, two distinct flames are seen. In this case, the NO_x emissions do not follow a linear trend; instead, the NO_x level peaks during co-firing before decreasing towards 100% coal, whereas the NO_x emissions from 100% oil remain significantly lower than those from 100% coal.

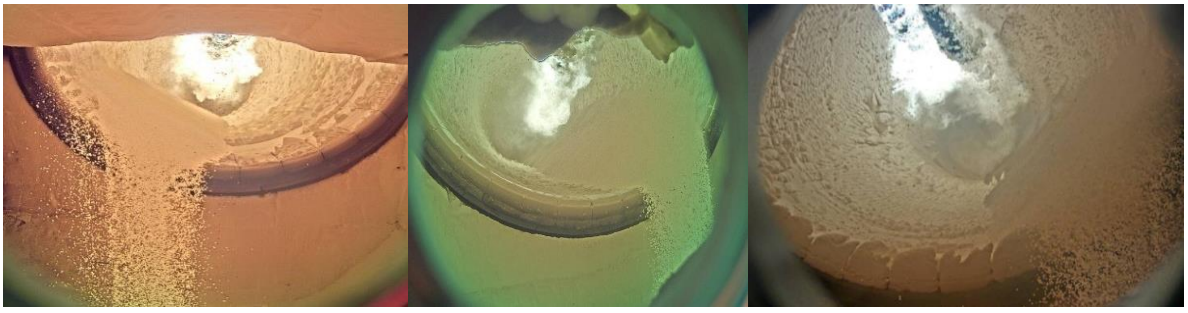

Figure 24. Photographs of the co-firing of 50% oil and 50% coal, with three burner configurations: single jet for panels 1 and 2 versus two jets for panel 3.

The decrease of NO_x emissions, along with the decrease of the in-flame O_2 concentration in coal, is also supported by the results of a full-scale trial. Figure 25 presents the NO_x emissions (mg/MJ) on the *y*-axis and the fuel mixture on the *x*-axis, ranging from 100% heavy oil (EO5) to 100% coal for a specific plant; the orange data-points are for an old coal facility configuration, and the purple data-points are for the new configuration. Oil produces much lower NO_x emissions than a coal flame, with consistent values seen between the old and new data-sets. However, the levels of NO_x have decreased significantly by 14% between the old and the new coal facility configurations. The primary measure implemented through the new facility enables operation with a coal:air ratio of 10 kg coal per kg of air, as compared with the previous ratio of 1 kg coal per kg of air. Thus, the new configuration presents a lower in-flame O_2 concentration.

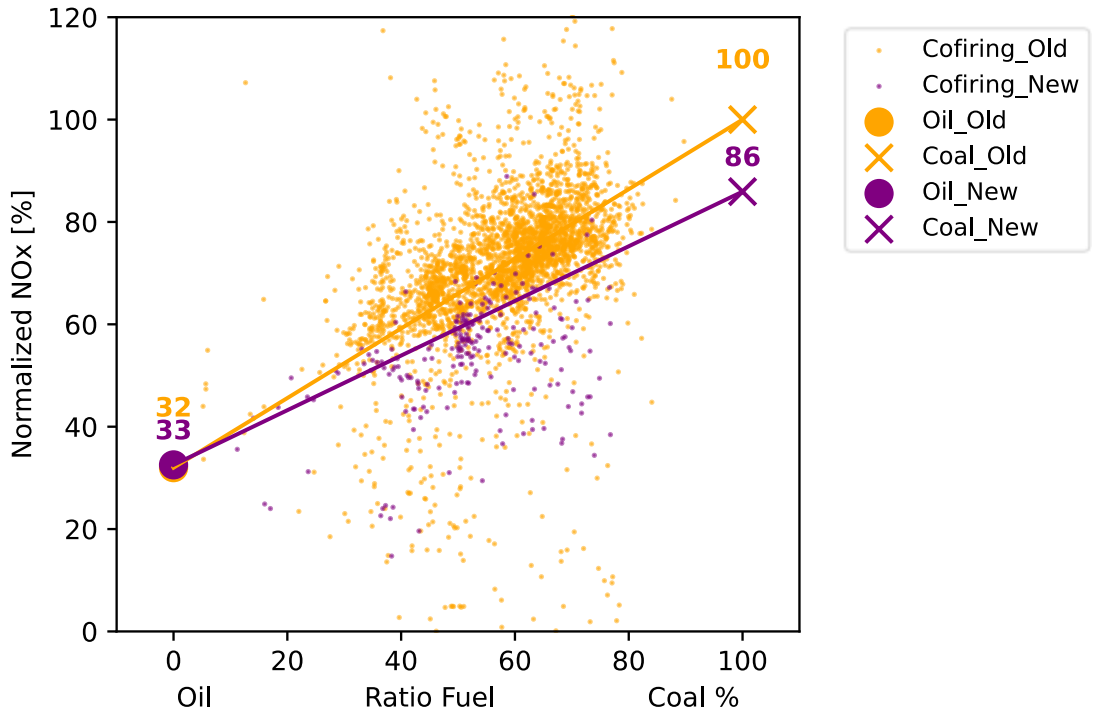

Figure 25. Levels of NO_x normalised in % measured in the chimney of a full-scale unit using fuel mixtures that range from 100% EO5 to 100% pulverised coal, before and after the implementation of a new coal facility that decreases the level of transport air in the coal. The orange data-points indicate 1 kg of coal per kg of air (Old configuration), while the purple colours data-points indicate 10 kg of coal per kg of air (New configuration). Data are filtered with a narrow range of power input and a production load minimum of 80%.

6.3 Scaling comparison measurements

Scaling perfectly a flame, as discussed in the theory section, is a difficult or perhaps impossible task. In the same experimental furnace and plants, Edland et al.[323] have observed that techniques to reduce NO_x emissions through primary measures in the ECF Unit were less-efficient in full-scale. This discrepancy was attributed to the limited scalability of char combustion.

Figure 26 illustrates the comparison of NOx emissions at the outlet of the HICK, ECF and full-scale Units, expressed in mg/MJ, as a function of the mixture, going from 100% coal to 100% hydrogen. The ECF data are derived from a previous campaign that evaluated various coal types; data from the ongoing campaign involving co-firing hydrogen and coal have not yet been incorporated. Thus, the ECF and full-scale Units present only data on pure coal firing.

The NO_x emissions measured at full scale are lower than those recorded in the ECF and HICK systems. Besides the scaling issues discussed in the *Theory* section, two other conditions are different. In the HICK and ECF furnaces, both the hot secondary air temperature and the wall temperatures are significantly lower than in the full-scale furnace. A higher furnace temperature enhances coal combustion, as observed during the HICK lancing campaign. On the final day of the experiments, the increased temperature led to an earlier ignition in the pure coal cases compared to the previous days. In addition, achieving the desired transport air-to-coal ratio at small pilot scale is challenging; due to the limited pipe diameters, the volume of transport air required for conveyance of the coal is higher.

A final point must be made regarding the impact of the bed on the flame. Certain chemical reactions cause the bed to cool the flame, which may contribute to the observed differences in NO_x emissions between the full-scale and pilot-scale set-ups. In the ECF Unit, there is an option to operate with a simulated bed. The results clearly demonstrate reductions in both the flame temperature and the levels of NO_x emissions when the bed is included in the conditions.

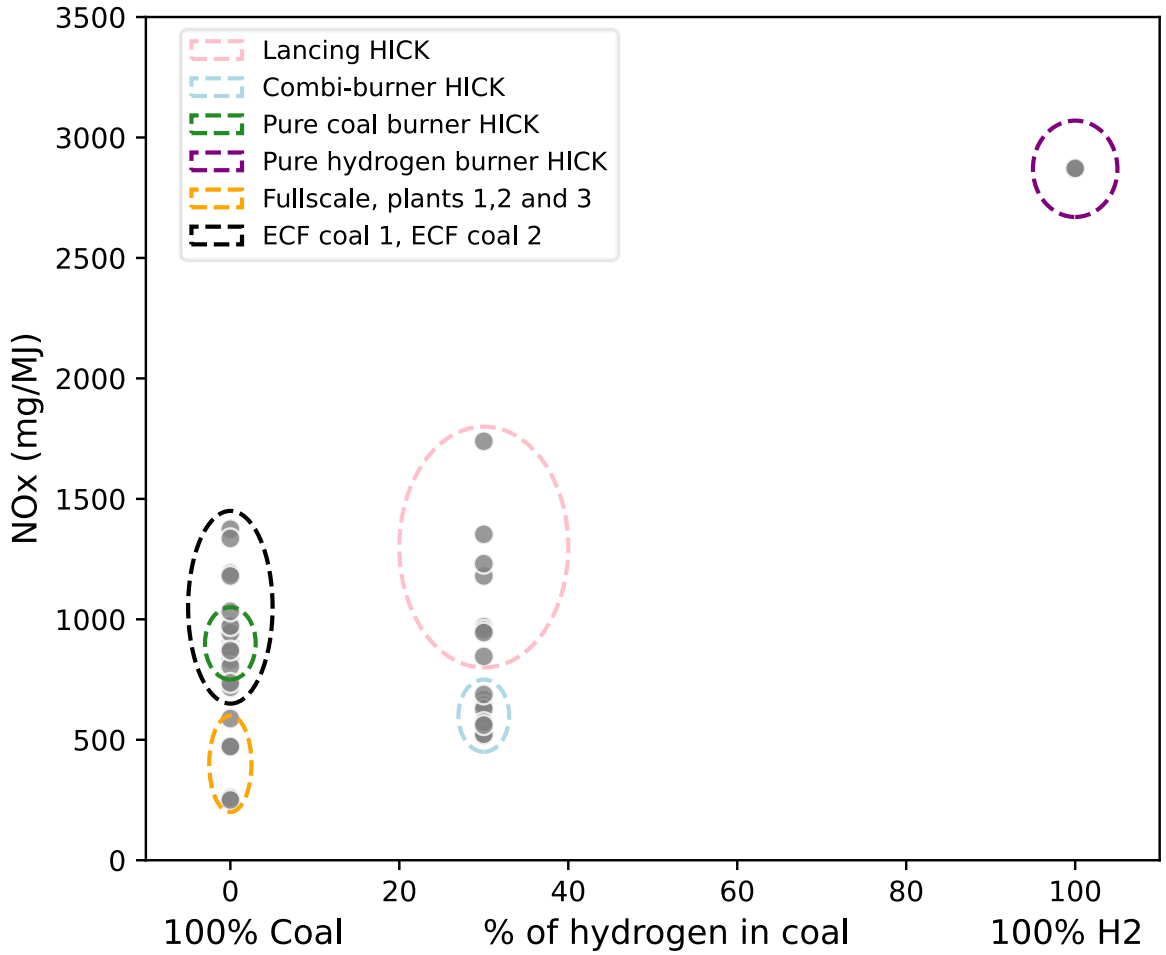

Figure 26. Comparisons of the outlet NO_x emissions (in mg/MJ) for the HICK, ECF and full-scale Units. The data presented for the ECF Unit are from a previous campaign[338].

7 On-going work

7.1 Measurement of Flame Temperature via OH* Chemiluminescence

Measuring the hydrogen flame temperature is essential for evaluating changes in flame characteristics and NO_x formation when co-firing hydrogen with coal. The absorption of OH[339–342] and the fluorescence emission of OH*– captured by either cameras[343,344] or emission spectra[345] in the middle-UV band – have proven to be reliable indicators of the gas temperature near the flame front. While absorption spectroscopy requires parallel open view-ports and the cameras comprise complex, costly systems, emission spectroscopy is preferred for its flexibility and cost-effectiveness at both the pilot and industrial scales. In large-scale applications, flame accessibility is often limited to a single view-port, making emission spectra a practical choice. Given the lack of research on OH* measurements in large-scale units, this on-going work explores the feasibility of using OH* emission spectra as a temperature indicator in highly turbulent, industrial-scale flames, thereby filling the gap in knowledge. Scaling up to more complex flame structures entails the following challenges, describing the on-going work:

1. Characterising the self-absorption of OH* for the rotational transitions at 306.7 nm and 309.2 nm of the vibrational transitions v=o and the rotational transitions at 312.5 nm and 314.8 nm for the vibrational transition v=1. Moreover, vibrational transitions in the range of 280–295 nm may warrant investigation.

2. Cleaning the background of the spectra. The super-positioning of other emission spectra, such as that for CO_2*, may show overlap with the OH* spectra, requiring background correction. In a pure hydrogen flame, this problem does not arise. However, in a methane flame and, potentially, in the co-firing coal and hydrogen, super-positioning of the CO_2* and OH* spectra may be observed. In such a case, it is highly important to subtract the CO_2* profile, to achieve high-precision fitting of the OH* spectra, and thereby a highly precise temperature.

3. Calibrating instruments in the UV range is challenging. A broad-band lamp (deuterium lamp) has been tested for calibration but it exhibits poor reliability in the middle UV range. Testing of a plasma source for UV-calibration is underway.

The ongoing work includes measurements in bench-scale flat flame burners and diffusion flame burners, as well as in technical-scale hydrogen flames (400 kW) and co-firing of hydrogen and coal (580 kW). In the laboratory scale, the OH* spectra are measured with the spectrometer

presented in the measurement section, and the extracted temperature is related to a temperature measurement made by the TDLAS H_2O and absorption measurements, and these are compared to the adiabatic flame temperature. In the pilot scale, only emissions spectra are measured in the hydrogen flame, while in the co-firing flame, both emission and absorption spectra are planned to be performed.

7.2 Scaling-up Co-firing of Coal and Hydrogen

The on-going initiatives to scale up co-firing technologies are scheduled to proceed in two phases. The first phase is planned for March 2025, followed by a second phase in the fall of 2025. To facilitate smoother integration of hydrogen at full scale, the burner designs are based on existing, large-scale coal burners. Variants will be developed and tested with different hydrogen velocities, hydrogen injection locations, axial and swirl primary air configurations, as well as single and multipipe coal setups.

8 Conclusion

The motivation for the presented work is partial coal replacement with hydrogen as a strategic step toward decarbonising the iron-ore pelletising process. In this context, this work delves into the changes in flame behaviour and NO_x emissions along the transition from solid fuel to gaseous fuels. In this respect, the findings reveal that hydrogen can feasibly replace up to 30% of the coal while maintaining NO_x emissions at acceptable levels. However, further up-scaling and characterisation of production conditions are needed.

The shift in the gaseous-to-solid fuel ratio not only influences the combustion efficiency, but also alters the structural intensity of the flame, which may have a significant impact on the thermal distribution in the kiln. From an industrial perspective, this transformation could re-define the heat transfer patterns along the kiln's length – potentially increasing radiation towards the pellet bed at the kiln's exit, while reducing it at the entrance. Such a shift poses challenges for pellet quality, as uneven heating may compromise the structural integrity of the pellets. To counteract a potentially more-unbalanced heat transfer profile, further optimisation is recommended, with emphasis on refining the coal particle size, hydrogen velocity, and burner design.

Hydrogen-coal co-firing, though a promising alternative for carbon reduction, requires consideration to control NO_x emissions. Two possible strategies are: (i) a lancing approach, which is cost-effective as it preserves the existing coal burner; and (ii) a fully integrated burner designed for hydrogen co-firing. From a NO_x emission perspective, hydrogen inject close to the coal flow is preferred, yielding the lowest NO_x emissions for combi-burners. For lancing, besides the positioning, angeling the flow towards the coal limits NO_x formation.

References

(1) *Chapter 3: Human Influence on the Climate System*. https://www.ipcc.ch/report/ar6/wg1/chapter/chapter-3/#faq-3-1/ (accessed 2024-08-16).
(2) (PDF) CO2 as a Primary Driver of Phanerozoic Climate. *ResearchGate* **2024**.
(3) Zachos, J. C.; Dickens, G. R.; Zeebe, R. E. An Early Cenozoic Perspective on Greenhouse Warming and Carbon-Cycle Dynamics. *Nature* **2008**, *451* (7176), 279–283. https://doi.org/10.1038/nature06588.
(4) Lisiecki, L. E.; Raymo, M. E. A Pliocene-Pleistocene Stack of 57 Globally Distributed Benthic δ18O Records. *Paleoceanography* **2005**, *20* (1). https://doi.org/10.1029/2004PA001071.
(5) Augustin, L.; Barbante, C.; Barnes, P. R. F.; Marc Barnola, J.; Bigler, M.; Castellano, E.; Cattani, O.; Chappellaz, J.; Dahl-Jensen, D.; Delmonte, B.; Dreyfus, G.; Durand, G.; Falourd, S.; Fischer, H.; Flückiger, J.; Hansson, M. E.; Huybrechts, P.; Jugie, G.; Johnsen, S. J.; Jouzel, J.; Kaufmann, P.; Kipfstuhl, J.; Lambert, F.; Lipenkov, V. Y.; Littot, G. C.; Longinelli, A.; Lorrain, R.; Maggi, V.; Masson-Delmotte, V.; Miller, H.; Mulvaney, R.; Oerlemans, J.; Oerter, H.; Orombelli, G.; Parrenin, F.; Peel, D. A.; Petit, J.-R.; Raynaud, D.; Ritz, C.; Ruth, U.; Schwander, J.; Siegenthaler, U.; Souchez, R.; Stauffer, B.; Peder Steffensen, J.; Stenni, B.; Stocker, T. F.; Tabacco, I. E.; Udisti, R.; van de Wal, R. S. W.; van den Broeke, M.; Weiss, J.; Wilhelms, F.; Winther, J.-G.; Wolff, E. W.; Zucchelli, M.; EPICA community members; EPICA community members (participants are listed alphabetically). Eight Glacial Cycles from an Antarctic Ice Core. *Nature* **2004**, *429* (6992), 623–628. https://doi.org/10.1038/nature02599.
(6) Marcott, S. A.; Shakun, J. D.; Clark, P. U.; Mix, A. C. A Reconstruction of Regional and Global Temperature for the Past 11,300 Years. *Science* **2013**, *339* (6124), 1198–1201. https://doi.org/10.1126/science.1228026.
(7) Andersen, K. K.; Azuma, N.; Barnola, J.-M.; Bigler, M.; Biscaye, P.; Caillon, N.; Chappellaz, J.; Clausen, H. B.; Dahl-Jensen, D.; Fischer, H.; Flückiger, J.; Fritzsche, D.; Fujii, Y.; Goto-Azuma, K.; Grønvold, K.; Gundestrup, N. S.; Hansson, M.; Huber, C.; Hvidberg, C. S.; Johnsen, S. J.; Jonsell, U.; Jouzel, J.; Kipfstuhl, S.; Landais, A.; Leuenberger, M.; Lorrain, R.; Masson-Delmotte, V.; Miller, H.; Motoyama, H.; Narita, H.; Popp, T.; Rasmussen, S. O.; Raynaud, D.; Rothlisberger, R.; Ruth, U.; Samyn, D.; Schwander, J.; Shoji, H.; Siggard-Andersen, M.-L.; Steffensen, J. P.; Stocker, T.; Sveinbjörnsdóttir, A. E.; Svensson, A.; Takata, M.; Tison, J.-L.; Thorsteinsson, Th.; Watanabe, O.; Wilhelms, F.; White, J. W. C.; North Greenland Ice Core Project members. High-Resolution Record of Northern Hemisphere Climate Extending into the Last Interglacial Period. *Nature* **2004**, *431* (7005), 147–151. https://doi.org/10.1038/nature02805.
(8) *Contents | Science 341, 6145*. Science. https://www.science.org/toc/science/341/6145 (accessed 2024-08-12).
(9) Minière, A.; von Schuckmann, K.; Sallée, J.-B.; Vogt, L. Robust Acceleration of Earth System Heating Observed over the Past Six Decades. *Sci Rep* **2023**, *13* (1), 22975. https://doi.org/10.1038/s41598-023-49353-1.
(10) Song, H.; Kemp, D. B.; Tian, L.; Chu, D.; Song, H.; Dai, X. Thresholds of Temperature Change for Mass Extinctions. *Nat Commun* **2021**, *12* (1), 4694. https://doi.org/10.1038/s41467-021-25019-2.
(11) *Geosphere-Biosphere Interactions and Climate*; Bengtsson, L. O., Hammer, C. U., Eds.; Cambridge University Press: Cambridge, 2001. https://doi.org/10.1017/CBO9780511529429.
(12) Lethiers, F. *Evolution de la biosphère et événements géologiques*; Taylor & Francis, 1998.
(13) Song, H.; Kemp, D. B.; Tian, L.; Chu, D.; Song, H.; Dai, X. Thresholds of Temperature Change for Mass Extinctions. *Nat Commun* **2021**, *12* (1), 4694. https://doi.org/10.1038/s41467-021-25019-2.
(14) Kaiho, K. Relationship between Extinction Magnitude and Climate Change during Major Marine and Terrestrial Animal Crises. *Biogeosciences* **2022**, *19* (14), 3369–3380. https://doi.org/10.5194/bg-19-3369-2022.

(15) Ritchie, H.; Roser, M. Half of the World's Habitable Land Is Used for Agriculture. *Our World in Data* **2019**.
(16) Schmaljohann, H.; Both, C. The Limits of Modifying Migration Speed to Adjust to Climate Change. *Nature Clim Change* **2017**, *7* (8), 573–576. https://doi.org/10.1038/nclimate3336.
(17) Radchuk, V.; Reed, T.; Teplitsky, C.; van de Pol, M.; Charmantier, A.; Hassall, C.; Adamík, P.; Adriaensen, F.; Ahola, M. P.; Arcese, P.; Miguel Avilés, J.; Balbontin, J.; Berg, K. S.; Borras, A.; Burthe, S.; Clobert, J.; Dehnhard, N.; de Lope, F.; Dhondt, A. A.; Dingemanse, N. J.; Doi, H.; Eeva, T.; Fickel, J.; Filella, I.; Fossøy, F.; Goodenough, A. E.; Hall, S. J. G.; Hansson, B.; Harris, M.; Hasselquist, D.; Hickler, T.; Joshi, J.; Kharouba, H.; Martínez, J. G.; Mihoub, J.-B.; Mills, J. A.; Molina-Morales, M.; Moksnes, A.; Ozgul, A.; Parejo, D.; Pilard, P.; Poisbleau, M.; Rousset, F.; Rödel, M.-O.; Scott, D.; Senar, J. C.; Stefanescu, C.; Stokke, B. G.; Kusano, T.; Tarka, M.; Tarwater, C. E.; Thonicke, K.; Thorley, J.; Wilting, A.; Tryjanowski, P.; Merilä, J.; Sheldon, B. C.; Pape Møller, A.; Matthysen, E.; Janzen, F.; Dobson, F. S.; Visser, M. E.; Beissinger, S. R.; Courtiol, A.; Kramer-Schadt, S. Adaptive Responses of Animals to Climate Change Are Most Likely Insufficient. *Nat Commun* **2019**, *10* (1), 3109. https://doi.org/10.1038/s41467-019-10924-4.
(18) Gowdy, J. Our Hunter-Gatherer Future: Climate Change, Agriculture and Uncivilization. *Futures* **2020**, *115*, 102488. https://doi.org/10.1016/j.futures.2019.102488.
(19) Gowdy, J.; Krall, L. Agriculture as a Major Evolutionary Transition to Human Ultrasociality. *J Bioecon* **2014**, *16* (2), 179–202. https://doi.org/10.1007/s10818-013-9156-6.
(20) Marcott, S. A.; Shakun, J. D. Global Temperature Changes Mapped across the Past 24,000 Years. *Nature* **2021**, *599* (7884), 208–209. https://doi.org/10.1038/d41586-021-03011-6.
(21) Bhargava, A.; Srivastava, S. Human Civilization and Agriculture. In *Participatory Plant Breeding: Concept and Applications*; Bhargava, A., Srivastava, S., Eds.; Springer: Singapore, 2019; pp 1–27. https://doi.org/10.1007/978-981-13-7119-6_1.
(22) Dasgupta, S.; Robinson, E. J. Z. Attributing Changes in Food Insecurity to a Changing Climate. *Sci Rep* **2022**, *12* (1), 4709. https://doi.org/10.1038/s41598-022-08696-x.
(23) *Chapter 5 : Food Security — Special Report on Climate Change and Land*. https://www.ipcc.ch/srccl/chapter/chapter-5/ (accessed 2024-08-12).
(24) Wu, X.; Lu, Y.; Zhou, S.; Chen, L.; Xu, B. Impact of Climate Change on Human Infectious Diseases: Empirical Evidence and Human Adaptation. *Environment International* **2016**, *86*, 14–23. https://doi.org/10.1016/j.envint.2015.09.007.
(25) Auffhammer, M. Quantifying Economic Damages from Climate Change. *The Journal of Economic Perspectives* **2018**, *32* (4), 33–52.
(26) Newman, R.; Noy, I. The Global Costs of Extreme Weather That Are Attributable to Climate Change. *Nat Commun* **2023**, *14* (1), 6103. https://doi.org/10.1038/s41467-023-41888-1.
(27) Kotz, M.; Levermann, A.; Wenz, L. The Economic Commitment of Climate Change. *Nature* **2024**, *628* (8008), 551–557. https://doi.org/10.1038/s41586-024-07219-0.
(28) Gilli, M.; Calcaterra, M.; Emmerling, J.; Granella, F. Climate Change Impacts on the Within-Country Income Distributions. *Journal of Environmental Economics and Management* **2024**, *127*, 103012. https://doi.org/10.1016/j.jeem.2024.103012.
(29) Gupta, A.; Venkataraman, S. Insurance and Climate Change. *Current Opinion in Environmental Sustainability* **2024**, *67*, 101412. https://doi.org/10.1016/j.cosust.2023.101412.
(30) Dlugolecki, A. F. Climate Change and the Insurance Industry. *Geneva Pap Risk Insur Issues Pract* **2000**, *25* (4), 582–601. https://doi.org/10.1111/1468-0440.00084.
(31) Collier, S. J.; Elliott, R.; Lehtonen, T.-K. Climate Change and Insurance. *Economy and Society* **2021**, *50* (2), 158–172. https://doi.org/10.1080/03085147.2021.1903771.
(32) Studio, U. of E. D. *1: Earth System Tipping Points*. Global Tipping Points. https://report-2023.global-tipping-points.org (accessed 2024-12-16).
(33) Canadell, J. G.; Jackson, R. B. Ecosystem Collapse and Climate Change: An Introduction. In *Ecosystem Collapse and Climate Change*; Canadell, J. G., Jackson, R. B., Eds.; Springer International Publishing: Cham, 2021; pp 1–9. https://doi.org/10.1007/978-3-030-71330-0_1.
(34) *Has the Earth's sixth mass extinction already arrived? | Nature*. https://www.nature.com/articles/nature09678 (accessed 2024-10-17).

(35) *Mass Extinction - an overview | ScienceDirect Topics*. https://www.sciencedirect.com/topics/earth-and-planetary-sciences/mass-extinction (accessed 2024-10-17).
(36) Robinson, A.; Lehmann, J.; Barriopedro, D.; Rahmstorf, S.; Coumou, D. Increasing Heat and Rainfall Extremes Now Far Outside the Historical Climate. *npj Clim Atmos Sci* **2021**, *4* (1), 1–4. https://doi.org/10.1038/s41612-021-00202-w.
(37) *NGFS publishes latest long-term climate macro-financial scenarios for climate risks assessment*. Network for Greening the Financial System. https://www.ngfs.net/en/press-release/ngfs-publishes-latest-long-term-climate-macro-financial-scenarios-climate-risks-assessment (accessed 2025-02-14).
(38) Tarpey, J.; McDonald, H.; Tröltzsch, J.; Valverde, M. J.; Tabares, E. T.; Umana, G.; Neumann, T.; Arvis, B.; Cauchy, A.; Bourkane, I. *Costs of Adaptation vs Costs of Inaction*; Report; Ramboll Management Consulting, Belgium, 2022. https://www.ecologic.eu/19650 (accessed 2025-02-09).
(39) OECD. *Economic Aspects of Adaptation to Climate Change: Costs, Benefits and Policy Instruments*; Agrawala, S., Fankhauser, S., Eds.; OECD, 2008. https://doi.org/10.1787/9789264046214-en.
(40) Bilal, A.; Känzig, D. R. The Macroeconomic Impact of Climate Change: Global vs. Local Temperature.
(41) Trust, S.; Joshi, S.; Lenton, T.; Oliver, J. The Emperor's New Climate Scenarios.
(42) Nordhaus, W. D. Economic Growth and Climate: The Carbon Dioxide Problem. *The American Economic Review* **1977**, *67* (1), 341–346.
(43) Piontek, F.; Kalkuhl, M.; Kriegler, E.; Schultes, A.; Leimbach, M.; Edenhofer, O.; Bauer, N. Economic Growth Effects of Alternative Climate Change Impact Channels in Economic Modeling. *Environ Resource Econ* **2019**, *73* (4), 1357–1385. https://doi.org/10.1007/s10640-018-00306-7.
(44) Weitzman, M. L. On Modeling and Interpreting the Economics of Catastrophic Climate Change. *Review of Economics and Statistics* **2009**, *91* (1), 1–19. https://doi.org/10.1162/rest.91.1.1.
(45) Burke, M.; Craxton, M.; Kolstad, C. D.; Onda, C.; Allcott, H.; Baker, E.; Barrage, L.; Carson, R.; Gillingham, K.; Graff-Zivin, J.; Greenstone, M.; Hallegatte, S.; Hanemann, W. M.; Heal, G.; Hsiang, S.; Jones, B.; Kelly, D. L.; Kopp, R.; Kotchen, M.; Mendelsohn, R.; Meng, K.; Metcalf, G.; Moreno-Cruz, J.; Pindyck, R.; Rose, S.; Rudik, I.; Stock, J.; Tol, R. S. J. Opportunities for Advances in Climate Change Economics. *Science* **2016**, *352* (6283), 292–293. https://doi.org/10.1126/science.aad9634.
(46) *Figures and data for the updated Planetary Boundaries*. https://www.stockholmresilience.org/research/planetary-boundaries/planetary-boundaries-data.html (accessed 2023-05-16).
(47) Rockström, J.; Steffen, W.; Noone, K.; Persson, Å.; Chapin, F. S. I.; Lambin, E.; Lenton, T.; Scheffer, M.; Folke, C.; Schellnhuber, H. J.; Nykvist, B.; de Wit, C.; Hughes, T.; van der Leeuw, S.; Rodhe, H.; Sörlin, S.; Snyder, P.; Costanza, R.; Svedin, U.; Falkenmark, M.; Karlberg, L.; Corell, R.; Fabry, V.; Hansen, J.; Walker, B.; Liverman, D.; Richardson, K.; Crutzen, P.; Foley, J. Planetary Boundaries: Exploring the Safe Operating Space for Humanity. *Ecology and Society* **2009**, *14* (2). https://doi.org/10.5751/ES-03180-140232.
(48) Rockström, J.; Gupta, J.; Qin, D.; Lade, S. J.; Abrams, J. F.; Andersen, L. S.; Armstrong McKay, D. I.; Bai, X.; Bala, G.; Bunn, S. E.; Ciobanu, D.; DeClerck, F.; Ebi, K.; Gifford, L.; Gordon, C.; Hasan, S.; Kanie, N.; Lenton, T. M.; Loriani, S.; Liverman, D. M.; Mohamed, A.; Nakicenovic, N.; Obura, D.; Ospina, D.; Prodani, K.; Rammelt, C.; Sakschewski, B.; Scholtens, J.; Stewart-Koster, B.; Tharammal, T.; van Vuuren, D.; Verburg, P. H.; Winkelmann, R.; Zimm, C.; Bennett, E. M.; Bringezu, S.; Broadgate, W.; Green, P. A.; Huang, L.; Jacobson, L.; Ndehedehe, C.; Pedde, S.; Rocha, J.; Scheffer, M.; Schulte-Uebbing, L.; de Vries, W.; Xiao, C.; Xu, C.; Xu, X.; Zafra-Calvo, N.; Zhang, X. Safe and Just Earth System Boundaries. *Nature* **2023**, *619* (7968), 102–111. https://doi.org/10.1038/s41586-023-06083-8.
(49) Randall, D. A.; Wood, R. A.; Bony, S.; Colman, R.; Fichefet, T.; Fyfe, J.; Kattsov, V.; Pitman, A.; Shukla, J.; Srinivasan, J.; Stouffer, R. J.; Sumi, A.; Taylor, K. E.; AchutaRao, K.; Allan, R.; Berger, A.; Blatter, H.; Bonfils, C.; Boone, A.; Bretherton, C.; Broccoli, A.; Brovkin, V.;

Dirmeyer, P.; Doutriaux, C.; Drange, H.; Frei, A.; Ganopolski, A.; Gent, P.; Gleckler, P.; Goosse, H.; Graham, R.; Gregory, J. M.; Gudgel, R.; Hall, A.; Hallegatte, S.; Hasumi, H.; Henderson-Sellers, A.; Hendon, H.; Hodges, K.; Holland, M.; Holtslag, A. A. M.; Hunke, E.; Huybrechts, P.; Ingram, W.; Joos, F.; Kirtman, B.; Klein, S.; Koster, R.; Kushner, P.; Lanzante, J.; Latif, M.; Pavlova, T.; Federationi, R.; Petoukhov, V.; Phillips, T.; Power, S.; Rahmstorf, S.; Raper, S. C. B.; Renssen, H.; Rind, D.; Roberts, M.; Rosati, A.; Schär, C.; Schmittner, A.; Scinocca, J.; Seidov, D.; Slater, A. G.; Slingo, J.; Smith, D.; Soden, B.; Stern, W.; Stone, D. A.; Sudo, K.; Takemura, T.; Tselioudis, G.; Webb, M.; Wild, M.; Manzini, E.; Matsuno, T.; McAvaney, B. Climate Models and Their Evaluation.

(50) Ito, G.; Romanou, A.; Kiang, N. Y.; Faluvegi, G.; Aleinov, I.; Ruedy, R.; Russell, G.; Lerner, P.; Kelley, M.; Lo, K. Global Carbon Cycle and Climate Feedbacks in the NASA GISS ModelE2.1. *Journal of Advances in Modeling Earth Systems* **2020**, *12* (10), e2019MS002030. https://doi.org/10.1029/2019MS002030.

(51) SubbaRao, H.-N. K., Lori Perkins, Gavin A. Schmidt, and Mark. *NASA Scientific Visualization Studio | Climate Drivers*. NASA Scientific Visualization Studio. https://svs.gsfc.nasa.gov/4908 (accessed 2024-08-15).

(52) Filonchyk, M.; Peterson, M. P.; Zhang, L.; Hurynovich, V.; He, Y. Greenhouse Gases Emissions and Global Climate Change: Examining the Influence of CO2, CH4, and N2O. *Science of The Total Environment* **2024**, *935*, 173359. https://doi.org/10.1016/j.scitotenv.2024.173359.

(53) Eyring, V.; Gillett, N. P.; Achutarao, K. M.; Barimalala, R.; Barreiro Parrillo, M.; Bellouin, N.; Cassou, C.; Durack, P. J.; Kosaka, Y.; McGregor, S.; Min, S.-K.; Morgenstern, O.; Sun, Y. Human Influence on the Climate System. In *Climate Change 2021: The Physical Science Basis. Contribution of Working Group I to the Sixth Assessment Report of the Intergovernmental Panel on Climate Change*; Masson-Delmotte, V., Zhai, P., Pirani, A., Connors, S. L., Péan, C., Berger, S., Caud, N., Chen, Y., Goldfarb, L., Gomis, M. I., Huang, M., Leitzell, K., Lonnoy, E., Matthews, J. B. R., Maycock, T. K., Waterfield, T., Yelekçi, Ö., Yu, R., Zhou, B., Eds.; Cambridge University Press: Cambridge, United Kingdom and New York, NY, USA, 2021; pp 423–552. https://doi.org/10.1017/9781009157896.001.

(54) Schmidt, G. A.; Ruedy, R. A.; Miller, R. L.; Lacis, A. A. Attribution of the Present-day Total Greenhouse Effect. *J. Geophys. Res.* **2010**, *115* (D20), 2010JD014287. https://doi.org/10.1029/2010JD014287.

(55) Jones, M. W.; Peters, G. P.; Gasser, T.; Andrew, R. M.; Schwingshackl, C.; Gütschow, J.; Houghton, R. A.; Friedlingstein, P.; Pongratz, J.; Le Quéré, C. National Contributions to Climate Change Due to Historical Emissions of Carbon Dioxide, Methane, and Nitrous Oxide since 1850. *Sci Data* **2023**, *10* (1), 155. https://doi.org/10.1038/s41597-023-02041-1.

(56) *Understanding methane emissions – Global Methane Tracker 2023 – Analysis*. IEA. https://www.iea.org/reports/global-methane-tracker-2023/understanding-methane-emissions (accessed 2024-08-12).

(57) Heilig, G. K. The Greenhouse Gas Methane (CH4): Sources and Sinks, the Impact of Population Growth, Possible Interventions. *Popul Environ* **1994**, *16* (2), 109–137. https://doi.org/10.1007/BF02208779.

(58) *Nitrous oxide emissions by sector*. Our World in Data. https://ourworldindata.org/grapher/nitrous-oxide-emissions-by-sector (accessed 2024-08-12).

(59) Ritchie, H.; Rosado, P.; Roser, M. Energy Mix. *Our World in Data* **2024**.

(60) Ritchie, H.; Roser, M. How Have the World's Energy Sources Changed over the Last Two Centuries? *Our World in Data* **2023**.

(61) Kaya, Y.; Yokobori, K. Environment, Energy and Economy: Strategies for Sustainability; 1999.

(62) *World Bank Open Data*. World Bank Open Data. https://data.worldbank.org (accessed 2025-03-13).

(63) *The Shift Data Portal*. https://theshiftdataportal.org/ (accessed 2025-03-13).

(64) Ritchie, H.; Rodés-Guirao, L.; Mathieu, E.; Gerber, M.; Ortiz-Ospina, E.; Hasell, J.; Roser, M. Population Growth. *Our World in Data* **2023**.

(65) *International - U.S. Energy Information Administration (EIA)*. https://www.eia.gov/international/overview/world (accessed 2025-03-13).

(66) Bloom, D. E.; Luca, D. L. Chapter 1 - The Global Demography of Aging: Facts, Explanations, Future. In *Handbook of the Economics of Population Aging*; Piggott, J., Woodland, A., Eds.; North-Holland, 2016; Vol. 1, pp 3–56. https://doi.org/10.1016/bs.hespa.2016.06.002.
(67) Prskawetz, A.; Kögel, T.; Sanderson, W. C.; Scherbov, S. The Effects of Age Structure on Economic Growth: An Application of Probabilistic Forecasting to India. *International Journal of Forecasting* **2007**, *23* (4), 587–602. https://doi.org/10.1016/j.ijforecast.2007.08.001.
(68) *[2006.03718] Past production constrains current energy demands: persistent scaling in global energy consumption and implications for climate change mitigation*. https://arxiv.org/abs/2006.03718?utm_source=chatgpt.com (accessed 2025-02-11).
(69) *The Future Population of the World: What Can We Assume Today*, 2nd ed.; Lutz, W., Ed.; Routledge: London, 2013. https://doi.org/10.4324/9781315066929.
(70) *The Dawn of Everything: A New History of Humanity by David Graeber | Goodreads*. https://www.goodreads.com/book/show/56269264-the-dawn-of-everything (accessed 2024-07-11).
(71) *Population Dynamics and Projection Methods | SpringerLink*. https://link.springer.com/book/10.1007/978-90-481-8930-4 (accessed 2024-07-11).
(72) *2052.info – A Global Forecast for the Next 40 Years*. http://www.2052.info/ (accessed 2024-07-11).
(73) Hubacek, K.; Chen, X.; Feng, K.; Wiedmann, T.; Shan, Y. Evidence of Decoupling Consumption-Based CO2 Emissions from Economic Growth. *Advances in Applied Energy* **2021**, *4*, 100074. https://doi.org/10.1016/j.adapen.2021.100074.
(74) Bithas, K.; Kalimeris, P. Re-Estimating the Decoupling Effect: Is There an Actual Transition towards a Less Energy-Intensive Economy? *Energy* **2013**, *51*, 78–84. https://doi.org/10.1016/j.energy.2012.11.033.
(75) Csereklyei, Z.; Rubio-Varas, M. d. M.; Stern, D. I. Energy and Economic Growth: The Stylized Facts. *The Energy Journal* **2016**, *37* (2), 223–256. https://doi.org/10.5547/01956574.37.2.zcse.
(76) Wang, F.; Zhang, Z. Decoupling Economic Growth from Energy Consumption in Top Five Energy Consumer Economies: A Technological and Urbanization Perspective. *Journal of Cleaner Production* **2022**, *357*, 131890. https://doi.org/10.1016/j.jclepro.2022.131890.
(77) Guo, Q.; You, W. Decoupling Analysis of Economic Growth, Energy Consumption and CO2 Emissions in the Industrial Sector of Guangdong Province. *International Journal of Low-Carbon Technologies* **2023**, *18*, 494–506. https://doi.org/10.1093/ijlct/ctad040.
(78) Parrique, T. The political economy of degrowth.
(79) *Ralentir ou périr: L'économie de la décroissance (Frenc…*. https://www.goodreads.com/book/show/62654568-ralentir-ou-p-rir (accessed 2024-07-11).
(80) Shafique, D.; Bi, K.; Steblyanskaya, A.; Hussain, S. Carbon Dioxide Emissions Reduction Efficiency and Growth Potential (A Case of Pakistan and China). *BRICS Report Series* **2023**, *2023*, 243–263. https://doi.org/10.3897/brics-econ.4.e93805.
(81) Borghesi, S. The Environmental Kuznets Curve: A Survey of the Literature. Social Science Research Network: Rochester, NY November 1, 1999. https://doi.org/10.2139/ssrn.200556.
(82) Chen, J.; Hu, T. E.; van Tulder, R. Is the Environmental Kuznets Curve Still Valid: A Perspective of Wicked Problems. *Sustainability* **2019**, *11* (17), 4747. https://doi.org/10.3390/su11174747.
(83) Kuznets, S. National Income, 1929-1932. In *National Income, 1929-1932*; NBER, 1934; pp 1–12.
(84) Stiglitz-Sen-Fitoussi-Commission-Report.Pdf. https://ec.europa.eu/eurostat/documents/8131721/8131772/Stiglitz-Sen-Fitoussi-Commission-report.pdf (accessed 2025-02-06).
(85) Daly, H. E. *Beyond Growth : The Economics of Sustainable Development*; Boston : Beacon Press, 1996.
(86) Jackson, T. *Prosperity without Growth: Economics for a Finite Planet*; Routledge: London, 2009. https://doi.org/10.4324/9781849774338.
(87) *Capital in the Twenty-First Century*. Harvard University Press. https://www.hup.harvard.edu/books/9780674430006 (accessed 2025-02-06).
(88) Parmigiani, A. The Political Power of Economic Elites in Contemporary Western Democracies.

(89) Brezis, E. Elites and Economic Outcomes - in New Palgrave Dictionary of Economics. *the New Palgrave Encyclopedia* **2008**.
(90) Nau, M. Economic Elites, Investments, and Income Inequality. *Social Forces* **2013**, *92* (2), 437–461.
(91) Solimano, A. Economic Elites, the Super Rich and Taxation: Implications for Development.
(92) Solimano, A. Economic Elites and the Super-Rich in the Twenty-First Century. In *Economic Elites, Crises, and Democracy: Alternatives Beyond Neoliberal Capitalism*; Solimano, A., Ed.; Oxford University Press, 2014; p 0. https://doi.org/10.1093/acprof:oso/9780199355983.003.0002.
(93) *Beyond Money: Toward an Economy of Well-Being - Ed Diener, Martin E.P. Seligman, 2004*. https://journals.sagepub.com/doi/10.1111/j.0963-7214.2004.00501001.x (accessed 2025-02-06).
(94) Lambert, J. G.; Hall, C. A. S.; Balogh, S.; Gupta, A.; Arnold, M. Energy, EROI and Quality of Life. *Energy Policy* **2014**, *64*, 153–167. https://doi.org/10.1016/j.enpol.2013.07.001.
(95) Zhang, W.; Balloo, K.; Hosein, A.; Medland, E. A Scoping Review of Well-Being Measures: Conceptualisation and Scales for Overall Well-Being. *BMC Psychology* **2024**, *12* (1), 585. https://doi.org/10.1186/s40359-024-02074-0.
(96) Galbraith, E. D.; Barrington-Leigh, C.; Miñarro, S.; Álvarez-Fernández, S.; Attoh, E. M. N. A. N.; Benyei, P.; Calvet-Mir, L.; Carmona, R.; Chakauya, R.; Chen, Z.; Chengula, F.; Fernández-Llamazares, Á.; García-del-Amo, D.; Glauser, M.; Huanca, T.; Izquierdo, A. E.; Junqueira, A. B.; Lanker, M.; Li, X.; Mariel, J.; Miara, M. D.; Porcher, V.; Porcuna-Ferrer, A.; Schlingmann, A.; Seidler, R.; Shrestha, U. B.; Singh, P.; Torrents-Ticó, M.; Ulambayar, T.; Wu, R.; Reyes-García, V. High Life Satisfaction Reported among Small-Scale Societies with Low Incomes. *Proceedings of the National Academy of Sciences* **2024**, *121* (7), e2311703121. https://doi.org/10.1073/pnas.2311703121.
(97) *A conceptual comparison of well-being measures used in the UK*. https://orda.shef.ac.uk/articles/report/A_conceptual_comparison_of_well-being_measures_used_in_the_UK/25118510?utm_source=chatgpt.com&file=44331752 (accessed 2025-02-17).
(98) Pretty, J.; Garrity, D.; Badola, H. K.; Barrett, M.; Butler Flora, C.; Cameron, C.; Grist, N.; Hepburn, L.; Hilburn, H.; Isham, A.; Jacobi, E.; Lal, R.; Lyster, S.; Magnason, A. S.; McGlade, J.; Middendorf, J.; Milner-Gulland, E. J.; Orr, D.; Peck, L.; Reij, C.; Rockström, J.; Ronesh, Y.; Saito, O.; Smith, J.; Smith, P.; Thorne, P.; Watabe, A.; Waters, S.; Wells, G. How the Concept of "Regenerative Good Growth" Could Help Increase Public and Policy Engagement and Speed Transitions to Net Zero and Nature Recovery. *Sustainability* **2025**, *17* (3), 849. https://doi.org/10.3390/su17030849.
(99) *Development: Time to leave GDP behind | Nature*. https://www.nature.com/articles/505283a (accessed 2025-02-06).
(100) Torino, U. degli S. di. *Complexity Economics*. Corso di laurea magistrale Interateneo in Fisica dei sistemi complessi. https://fisica-sc.campusnet.unito.it/do/corsi.pl/Show?_id=anfb (accessed 2024-07-11).
(101) *Well-Being in Contemporary Society*; Søraker, J. H., Van Der Rijt, J.-W., De Boer, J., Wong, P.-H., Brey, P., Eds.; Happiness Studies Book Series; Springer International Publishing: Cham, 2015. https://doi.org/10.1007/978-3-319-06459-8.
(102) *TOWARDS A NORDIC WELLBEING ECONOMY*. https://pub.norden.org/nord2021-049/# (accessed 2024-07-11).
(103) *The spirit level: why more equal societies almost alway…*. https://www.goodreads.com/book/show/6304389-the-spirit-level (accessed 2024-07-11).
(104) *Small Is Beautiful: Economics as if People Mattered*. https://www.goodreads.com/book/show/1117634.Small_Is_Beautiful (accessed 2024-07-11).
(105) Sirgy, M. J. *Positive Balance: A Theory of Well-Being and Positive Mental Health*; Social Indicators Research Series; Springer International Publishing: Cham, 2020; Vol. 80. https://doi.org/10.1007/978-3-030-40289-1.
(106) Sirgy, M. Philosophical Foundations, Definitions, and Measures of Wellbeing; 2021; pp 5–35. https://doi.org/10.1007/978-3-030-71888-6_1.

(107) *Making Sense of Chaos: A Better Economics for a Better …*. https://www.goodreads.com/book/show/197643461-making-sense-of-chaos (accessed 2024-07-11).
(108) *Le Monde sans fin*. https://www.goodreads.com/book/show/59478153-le-monde-sans-fin (accessed 2024-07-11).
(109) *Capitalism, Socialism, Ecology*. https://www.goodreads.com/book/show/486961.Capitalism_Socialism_Ecology (accessed 2024-07-11).
(110) Hawkins, M. Neo-Extractivism, (de)Growth and Resurgent Pink Tide Governments in Latin America. *Geography Compass* **2024**, *18* (6), e12761. https://doi.org/10.1111/gec3.12761.
(111) Harbin Engineering University; Steblyanskaya, A.; Ai, M.; Harbin Engineering University; Bocharnikov, V.; Pacific Geographical InstitutePacific Geographical Institute; Denisov, A.; Kostroma State University. Strategies for Green Economy in China. In *Foresight and STI Governance*; 2021; Vol. 15, pp 74–85. https://doi.org/10.17323/2500-2597.2021.1.74.85.
(112) *Yearly Electricity Data*. Ember. https://ember-energy.org/data/yearly-electricity-data (accessed 2025-02-10).
(113) Institute, E. *Home*. Statistical review of world energy. https://www.energyinst.org/statistical-review/home (accessed 2025-02-10).
(114) *Carbon intensity of electricity generation*. Our World in Data. https://ourworldindata.org/grapher/carbon-intensity-electricity (accessed 2024-12-16).
(115) *Carbon dioxide emissions factors*. Our World in Data. https://ourworldindata.org/grapher/carbon-dioxide-emissions-factor (accessed 2024-12-16).
(116) *Estimation of the quantity of metals to phase out fossil fuels in a full system replacement, compared to mineral resources - Publications, reports, maps and posters*. Hakku. https://hakku.gtk.fi/en/publications?id=100074 (accessed 2024-12-09).
(117) Liang, Y.; Kleijn, R.; van der Voet, E. Increase in Demand for Critical Materials under IEA Net-Zero Emission by 2050 Scenario. *Applied Energy* **2023**, *346*, 121400. https://doi.org/10.1016/j.apenergy.2023.121400.
(118) Kalkanis, K.; Vokas, G.; Kiskira, K.; Psomopoulos, C. S. Investigating the Sustainability of Wind Turbine Recycling: A Case Study—Greece. *Mater Circ Econ* **2024**, *6* (1), 52. https://doi.org/10.1007/s42824-024-00147-4.
(119) *End-of-life management Solar Photovoltaic Panels*. https://www.irena.org/publications/2016/Jun/End-of-life-management-Solar-Photovoltaic-Panels (accessed 2025-03-08).
(120) Domínguez, A.; Geyer, R. Photovoltaic Waste Assessment of Major Photovoltaic Installations in the United States of America. *Renewable Energy* **2019**, *133*, 1188–1200. https://doi.org/10.1016/j.renene.2018.08.063.
(121) Sproul, E. G.; Khalifa, S. A.; Ennis, B. L. Environmental and Economic Assessment of Wind Turbine Blade Recycling Approaches. *ACS Sustainable Resour. Manage.* **2025**, *2* (1), 39–49. https://doi.org/10.1021/acssusresmgt.4c00256.
(122) Belançon, M. P.; Sandrini, M.; Tonholi, F.; Herculano, L. S.; Dias, G. S. Towards Long Term Sustainability of C-Si Solar Panels: The Environmental Benefits of Glass Sheet Recovery. *Renewable Energy Focus* **2022**, *42*, 206–210. https://doi.org/10.1016/j.ref.2022.06.009.
(123) Jasińska, D.; Dutkiewicz, M. Waste Management of Wind Turbine Blades—A Review of Recycling Methods and Applications in Cementitious Composites. *Sustainability* **2025**, *17* (3), 805. https://doi.org/10.3390/su17030805.
(124) Canada, N. R. *Iron ore facts*. https://natural-resources.canada.ca/our-natural-resources/minerals-mining/mining-data-statistics-and-analysis/minerals-metals-facts/iron-ore-facts/20517 (accessed 2024-08-13).
(125) All the Metals We've Mined in One Visualization. https://elements.visualcapitalist.com/wp-content/uploads/2021/09/all-of-the-metals-one-visualization.html (accessed 2024-07-02).
(126) *Iron and Steel Technology Roadmap – Analysis*. IEA. https://www.iea.org/reports/iron-and-steel-technology-roadmap (accessed 2024-08-13).
(127) Reichl, D. C. World Mining Data 2024.

(128) *World Mining Data - Data Section*. https://www.world-mining-data.info/?World_Mining_Data___Data_Section (accessed 2024-07-02).
(129) Bhagat, R. P. *Agglomeration of Iron Ores*; CRC Press: Boca Raton, 2019. https://doi.org/10.1201/9781315269504.
(130) Gan, Y.; Griffin, W. M. Analysis of Life-Cycle GHG Emissions for Iron Ore Mining and Processing in China—Uncertainty and Trends. *Resources Policy* **2018**, *58*, 90–96. https://doi.org/10.1016/j.resourpol.2018.03.015.
(131) Mourao, J.; Cameron, I.; Huerta, M.; Patel, N.; Pereira, R. COMPARISON OF SINTER AND PELLET USAGE IN AN INTEGRATED STEEL PLANT 1; 2020.
(132) *Steel – Breakthrough Agenda Report 2023 – Analysis*. IEA. https://www.iea.org/reports/breakthrough-agenda-report-2023/steel (accessed 2024-07-03).
(133) Fan, Z.; Friedmann, S. J. Low-Carbon Production of Iron and Steel: Technology Options, Economic Assessment, and Policy. *Joule* **2021**, *5* (4), 829–862. https://doi.org/10.1016/j.joule.2021.02.018.
(134) *Ultra-Low CO2 steelmaking | ULCOS Project | Fact Sheet | FP6*. CORDIS | European Commission. https://cordis.europa.eu/project/id/515960 (accessed 2025-02-12).
(135) *Our program SALCOS®*. SALCOS®. https://salcos.salzgitter-ag.com/en/salcos.html (accessed 2025-02-12).
(136) *HYBRIT - Fossilfritt stål - en gemensam möjlighet!*. HYBRIT. https://www.hybritdevelopment.se/ (accessed 2024-07-02).
(137) *MIDREX H2: Ultimate Low CO2 Ironmaking and its place in the new Hydrogen Economy*. Midrex Technologies, Inc. https://www.midrex.com/tech-article/midrex-h2-ultimate-low-co2-ironmaking-and-its-place-in-the-new-hydrogen-economy/ (accessed 2025-02-12).
(138) Federation, T. J. I. and S. *course50 - Green Innovation Fund Project Hydrogen Steelmaking Consortium*. GREINS -. https://www.greins.jp/course50/en/ (accessed 2025-02-23).
(139) *Circored™ hydrogen-based reduction*. Metso. https://www.metso.com/portfolio/circored-hydrogen-based-reduction/ (accessed 2024-07-02).
(140) *HYFOR pilot plant under operation – the next step for carbon free, hydrogen-based direct reduction is done*. https://www.primetals.com/press-media/news/hyfor-pilot-plant-under-operation-the-next-step-for-carbon-free-hydrogen-based-direct-reduction-is-done (accessed 2024-07-09).
(141) Dumas, J.; Dubois, A.; Thiran, P.; Jacques, P.; Contino, F.; Cornélusse, B.; Limpens, G. The Energy Return on Investment of Whole Energy Systems: Application to Belgium. *Biophys Econ Sust* **2022**, *7* (4), 12. https://doi.org/10.1007/s41247-022-00106-0.
(142) Hall, C. A. S.; Lambert, J. G.; Balogh, S. B. EROI of Different Fuels and the Implications for Society. *Energy Policy* **2014**, *64*, 141–152. https://doi.org/10.1016/j.enpol.2013.05.049.
(143) Murphy, D. J.; Raugei, M.; Carbajales-Dale, M.; Rubio Estrada, B. Energy Return on Investment of Major Energy Carriers: Review and Harmonization. *Sustainability* **2022**, *14* (12), 7098. https://doi.org/10.3390/su14127098.
(144) *Fossil fuels increasingly offer a poor return on energy investment*. ScienceDaily. https://www.sciencedaily.com/releases/2019/07/190711114846.htm (accessed 2025-02-10).
(145) Delannoy, L.; Longaretti, P.-Y.; Murphy, D. J.; Prados, E. Assessing Global Long-Term EROI of Gas: A Net-Energy Perspective on the Energy Transition. *Energies* **2021**, *14* (16), 5112. https://doi.org/10.3390/en14165112.
(146) *Renewable Energies*; García Márquez, F. P., Karyotakis, A., Papaelias, M., Eds.; Springer International Publishing: Cham, 2018. https://doi.org/10.1007/978-3-319-45364-4.
(147) Dsilva Winfred Rufuss, D.; Sonu Ashritha, K. S.; Suganthi, L. Green Energy Revolution: A Unique Approach for Energy Forecasting and Optimization towards Sustainable Energy Planning and Social Development. *Environ Dev Sustain* **2024**. https://doi.org/10.1007/s10668-024-04826-9.
(148) Ameray, A.; Cavard, X.; Cyr, D.; Valeria, O.; Girona, M. M.; Bergeron, Y. One Century of Carbon Dynamics in the Eastern Canadian Boreal Forest under Various Management Strategies and Climate Change Projections. *Ecological Modelling* **2024**, *498*, 110894. https://doi.org/10.1016/j.ecolmodel.2024.110894.

(149) *Forest carbon budgets and Finnish climate policy: explaining my position*. https://www.linkedin.com/pulse/forest-carbon-budgets-finnish-climate-policy-my-johan-rockstr%C3%B6m-smize (accessed 2025-03-13).
(150) Ke, P.; Ciais, P.; Sitch, S.; Li, W.; Bastos, A.; Liu, Z.; Xu, Y.; Gui, X.; Bian, J.; Goll, D. S.; Xi, Y.; Li, W.; O'Sullivan, M.; Souza, J. G. de; Friedlingstein, P.; Chevallier, F. Low Latency Carbon Budget Analysis Reveals a Large Decline of the Land Carbon Sink in 2023. arXiv July 17, 2024. https://doi.org/10.48550/arXiv.2407.12447.
(151) Islam, Md. R.; Jönsson, A. M.; Bergkvist, J.; Lagergren, F.; Lindeskog, M.; Mölder, M.; Scholze, M.; Kljun, N. Projected Effects of Climate Change and Forest Management on Carbon Fluxes and Biomass of a Boreal Forest. *Agricultural and Forest Meteorology* **2024**, *349*, 109959. https://doi.org/10.1016/j.agrformet.2024.109959.
(152) Kelly, J.; Kljun, N.; Cai, Z.; Doerr, S. H.; D'Onofrio, C.; Holst, T.; Lehner, I.; Lindroth, A.; Thapa, S.; Vestin, P.; Santín, C. Wildfire Impacts on the Carbon Budget of a Managed Nordic Boreal Forest. *Agricultural and Forest Meteorology* **2024**, *351*, 110016. https://doi.org/10.1016/j.agrformet.2024.110016.
(153) Martínez-García, E.; Nilsson, M. B.; Laudon, H.; Lundmark, T.; Fransson, J. E. S.; Wallerman, J.; Peichl, M. Drought Response of the Boreal Forest Carbon Sink Is Driven by Understorey–Tree Composition. *Nat. Geosci.* **2024**, *17* (3), 197–204. https://doi.org/10.1038/s41561-024-01374-9.
(154) Yu, L.; Fan, L.; Ciais, P.; Xiao, J.; Frappart, F.; Sitch, S.; Chen, J.; Xiao, X.; Fensholt, R.; Chang, Z.; Fang, H.; Li, X.; Cui, T.; Ma, M.; Wigneron, J.-P. Forest Degradation Contributes More to Carbon Loss than Forest Cover Loss in North American Boreal Forests. *International Journal of Applied Earth Observation and Geoinformation* **2024**, *128*, 103729. https://doi.org/10.1016/j.jag.2024.103729.
(155) de Villafranca Casas, M. J.; Smit, S.; Nilsson, A.; Kuramochi, T. Climate Targets by Major Steel Companies: An Assessment of Collective Ambition and Planned Emission Reduction Measures. *Energy and Climate Change* **2024**, *5*, 100120. https://doi.org/10.1016/j.egycc.2023.100120.
(156) Ocko, I. B.; Hamburg, S. P. Climate Consequences of Hydrogen Emissions. *Atmospheric Chemistry and Physics* **2022**, *22* (14), 9349–9368. https://doi.org/10.5194/acp-22-9349-2022.
(157) Ehhalt, D. H.; Dorn, H.-P.; Poppe, D. The Chemistry of the Hydroxyl Radical in the Troposphere. *Proceedings of the Royal Society of Edinburgh, Section B: Biological Sciences* **1990**, *97*, 17–34. https://doi.org/10.1017/S0269727000005273.
(158) Kordzadeh, E.; Campos, F.; Strueber, G.; Schwalm, T. CONTRIBUÇÃO PARA COMPARAÇÕES ENTRE AS TECNOLOGIAS STRAIGHT GRATE E GRATE-KILN; 2017; pp 222–236. https://doi.org/10.5151/2594-357X-30901.
(159) 2286 - SİVRİKAYA, O., AROL, A.I. - ALTERNATIVE BINDERS TO BENTONITE FOR IRON ORE PELLETIZING, PART I, EFFECTS ON PHYSICAL AND MECHANICAL PROPERTIES.Pdf. https://publicacoes.entmme.org/filebase/2013/2286%20-%20S%C4%B0VR%C4%B0KAYA%2C%20O.%2C%20AROL%2C%20A.I.%20-%20ALTERNATIVE%20BINDERS%20TO%20BENTONITE%20FOR%20IRON%20ORE%20PELLETIZING%2C%20PART%20I%2C%20EFFECTS%20ON%20PHYSICAL%20AND%20MECHANICAL%20PROPERTIES.PDF?utm_source=chatgpt.com (accessed 2025-02-12).
(160) Sivrikaya, O.; Arol, A. I. ALTERNATIVE BINDERS TO BENTONITE FOR IRON ORE PELLETIZING : PART II : EFFECTS ON METALLURGICAL AND CHEMICAL PROPERTIES. *HOLOS* **2014**, *3*, 104–111. https://doi.org/10.15628/holos.2014.1759.
(161) (PDF) Use of Organic Binders and Borates in Pelletizing of Iron Oxides. In *ResearchGate*.
(162) Eisele, T. C.; Kawatra, S. K. A Review of Binders in Iron Ore Pelletization. *Mineral Processing and Extractive Metallurgy Review* **2003**, *24* (1), 1.
(163) Umadevi, T.; Lobo, N. F.; Desai, S.; Mahapatra, P. C.; Sah, R.; Prabhu, M. Optimization of Firing Temperature for Hematite Pellets. *ISIJ Int.* **2013**, *53* (9), 1673–1682. https://doi.org/10.2355/isijinternational.53.1673.
(164) Ayyandurai, A.; Pal, J. Kinetics of Carbon Oxidation During Induration of Hematite Ore Pellet. *Mining, Metallurgy & Exploration* **2022**, *39* (6), 2551–2560. https://doi.org/10.1007/s42461-022-00692-z.

(165) Kumar, S.; Ravi, B.; Sivrikaya, O.; Nanda, R. The Study of Pelletizing of Mixed Hematite and Magnetite Ores. *Science of Sintering* **2019**, *51*. https://doi.org/10.2298/SOS1901027K.
(166) Meyer, K. Pelletizing of Iron Ores; 1980.
(167) Boateng, A. A. 1 - The Rotary Kiln Evolution and Phenomenon. In *Rotary Kilns*; Boateng, A. A., Ed.; Butterworth-Heinemann: Burlington, 2008; pp 1–14. https://doi.org/10.1016/B978-075067877-3.50003-9.
(168) Mungyeko Bisulandu, B.-J. R.; Huchet, F. Rotary Kiln Process: An Overview of Physical Mechanisms, Models and Applications. *Applied Thermal Engineering* **2023**, *221*, 119637. https://doi.org/10.1016/j.applthermaleng.2022.119637.
(169) Mourao, J.; Huerta, M.; Medeiros, U.; Cameron, I.; O'leary, K. GUIDELINES FOR SELECTING PELLET PLANT TECHNOLOGY; 2012.
(170) *DR-Grade Iron Ore Pellets 2025-2033 Trends: Unveiling Growth Opportunities and Competitor Dynamics*. https://www.datainsightsmarket.com/reports/dr-grade-iron-ore-pellets-1066877 (accessed 2025-02-14).
(171) *Iron Ore Pellets Market Size, Share And Growth Report, 2030*. https://www.grandviewresearch.com/industry-analysis/iron-ore-pellets-market (accessed 2025-02-14).
(172) Thorat, T.; Nurni, V. N.; Basavaraja, M.; Singhai, M.; Hazra, S.; Mogale, A. Modelling of Heat Transfer in a Straight Grate Pellet Induration Reactor Complemented with Plant Scale Experiments. *Mineral Processing and Extractive Metallurgy* **2022**, *131* (3), 283–289. https://doi.org/10.1080/25726641.2021.1984828.
(173) Barati, M. Dynamic Simulation of Pellet Induration Process in Straight-Grate System. *International Journal of Mineral Processing* **2008**, *89* (1–4), 30–39. https://doi.org/10.1016/j.minpro.2008.09.008.
(174) Thurlby, J. A.; Batterham, R. J.; Turner, R. E. Development and Validation of a Mathematical Model for the Moving Grate Induration of Iron Ore Pellets. *International Journal of Mineral Processing* **1979**, *6* (1), 43–64. https://doi.org/10.1016/0301-7516(79)90031-0.
(175) Dave, S.; Patra, S.; Bapat, Y.; Banerjee, G.; Chattopadhyay, S. A Mathematical Model for Straight-Grate Iron Oxide Pellet Induration Furnace: Formulation, Plant Scale Validation, Implementation and Control. *JOM* **2023**, *75* (7), 2406–2420. https://doi.org/10.1007/s11837-023-05819-1.
(176) Ehlmé, E.; Gunnarsson, A.; Andersson, K.; Normann, F. Heat Transfer Conditions in Hydrogen-Fired Rotary Kilns for Iron Ore Processing. *Ind. Eng. Chem. Res.* **2023**, *62* (37), 15098–15108. https://doi.org/10.1021/acs.iecr.3c02264.
(177) Gunnarsson, A.; Andersson, K.; Adams, B. R.; Fredriksson, C. Full-Scale 3D-Modelling of the Radiative Heat Transfer in Rotary Kilns with a Present Bed Material. *International Journal of Heat and Mass Transfer* **2020**, *147*, 118924. https://doi.org/10.1016/j.ijheatmasstransfer.2019.118924.
(178) Gunnarsson, A.; Andersson, K.; Adams, B. R.; Fredriksson, C. Discrete-Ordinates Modelling of the Radiative Heat Transfer in a Pilot-Scale Rotary Kiln. *Energies* **2020**, *13* (9), 2192. https://doi.org/10.3390/en13092192.
(179) Bäckström, D.; Johansson, R.; Andersson, K.; Wiinikka, H.; Fredriksson, C. On the Use of Alternative Fuels in Rotary Kiln Burners — An Experimental and Modelling Study of the Effect on the Radiative Heat Transfer Conditions. *Fuel Processing Technology* **2015**, *138*, 210–220. https://doi.org/10.1016/j.fuproc.2015.05.021.
(180) Scherbyna, V.; Gondlyakh, A.; Sokolskiy, A.; Shilovich, Y.; Bulavina, N. Failure Analysis of Refractories in Rotary Kilns. In *Advanced Manufacturing Processes IV*; Tonkonogyi, V., Ivanov, V., Trojanowska, J., Oborskyi, G., Pavlenko, I., Eds.; Springer International Publishing: Cham, 2023; pp 562–573. https://doi.org/10.1007/978-3-031-16651-8_53.
(181) Heidari, A.; Heikkilä, A.; Iljana, M.; Fabritius, T. A Comparison Between the Reduction Behavior of DRI and BF Pellets in H2 and CO Atmospheres. *J. Sustain. Metall.* **2024**, *10* (4), 2068–2084. https://doi.org/10.1007/s40831-024-00951-x.
(182) *Effect of BF-Grade Pellets on DR Plant Operations*. Midrex Technologies, Inc. https://www.midrex.com/tech-article/effect-of-bf-grade-pellets-on-dr-plant-operations/ (accessed 2025-02-13).

(183) Elahidoost, H.; Sheibani, S.; Raygan, S.; Hosseini, L.; Ahmadabadi, A. D.; Esmaeili, N. Influence of Magnetite Concentrate Morphology on Oxidation and Sintering Rates of Pellet during Induration. *Journal of Materials Research and Technology* **2023**, *26*, 7116–7126. https://doi.org/10.1016/j.jmrt.2023.09.085.
(184) *Iron Ore Pellet - an overview | ScienceDirect Topics*. https://www.sciencedirect.com/topics/chemical-engineering/iron-ore-pellet (accessed 2025-03-08).
(185) Gupta, P.; Yapar, G.; Poletto, M.; Barletta, D. Procedures for the Determination of Physical Properties of DR Raw Materials, Intermediate and Products - Report on Bed-Scale Experiments on Two Different Pellet Types.
(186) (PDF) Some Correlation Between Physical and Metallurgical Properties of Iron Ore Pellets. In *ResearchGate*.
(187) Bersenev, I. S.; Pokolenko, S. I.; Sabirov, E. R.; Spirin, N. A.; Borisenko, A. V.; Kurochkin, A. R. Influence of the Iron Ore Pellets Macrostructure on Their Strength. *Steel Transl.* **2023**, *53* (11), 1018–1022. https://doi.org/10.3103/S0967091223110062.
(188) Alsop, P. A. *Cement Plant Operations Handbook: For Dry Process Plants*; Tradeship Publications Ltd, 2007.
(189) John, J. P. Parametric Studies of Cement Production Processes. *Journal of Energy* **2020**, *2020* (1), 4289043. https://doi.org/10.1155/2020/4289043.
(190) Farfan, J.; Fasihi, M.; Breyer, C. Trends in the Global Cement Industry and Opportunities for Long-Term Sustainable CCU Potential for Power-to-X. *Journal of Cleaner Production* **2019**, *217*, 821–835. https://doi.org/10.1016/j.jclepro.2019.01.226.
(191) Cheng, D.; Reiner, D. M.; Yang, F.; Cui, C.; Meng, J.; Shan, Y.; Liu, Y.; Tao, S.; Guan, D. Projecting Future Carbon Emissions from Cement Production in Developing Countries. *Nat Commun* **2023**, *14* (1), 8213. https://doi.org/10.1038/s41467-023-43660-x.
(192) Summerbell, D. L.; Barlow, C. Y.; Cullen, J. M. Potential Reduction of Carbon Emissions by Performance Improvement: A Cement Industry Case Study. *Journal of Cleaner Production* **2016**, *135*, 1327–1339. https://doi.org/10.1016/j.jclepro.2016.06.155.
(193) Gartner, E. Industrially Interesting Approaches to "Low-CO2" Cements. *Cement and Concrete Research* **2004**, *34* (9), 1489–1498. https://doi.org/10.1016/j.cemconres.2004.01.021.
(194) Oates, J. A. H. *Lime and Limestone: Chemistry and Technology, Production and Uses*; John Wiley & Sons, 2008.
(195) Simoni, M.; Wilkes, M. D.; Brown, S.; Provis, J. L.; Kinoshita, H.; Hanein, T. Decarbonising the Lime Industry: State-of-the-Art. *Renewable and Sustainable Energy Reviews* **2022**, *168*, 112765. https://doi.org/10.1016/j.rser.2022.112765.
(196) de Vries, W. Impacts of Nitrogen Emissions on Ecosystems and Human Health: A Mini Review. *Current Opinion in Environmental Science & Health* **2021**, *21*, 100249. https://doi.org/10.1016/j.coesh.2021.100249.
(197) Shaw, S.; Van Heyst, B. Nitrogen Oxide (NOx) Emissions as an Indicator for Sustainability. *Environmental and Sustainability Indicators* **2022**, *15*, 100188. https://doi.org/10.1016/j.indic.2022.100188.
(198) Tang, L.; Xue, X.; Jia, M.; Jing, H.; Wang, T.; Zhen, R.; Huang, M.; Tian, J.; Guo, J.; Li, L.; Bo, X.; Wang, S. Iron and Steel Industry Emissions and Contribution to the Air Quality in China. *Atmospheric Environment* **2020**, *237*, 117668. https://doi.org/10.1016/j.atmosenv.2020.117668.
(199) *Photochemical Smog - an overview | ScienceDirect Topics*. https://www.sciencedirect.com/topics/earth-and-planetary-sciences/photochemical-smog (accessed 2024-07-04).
(200) Nguyen, D.-H.; Lin, C.; Vu, C.-T.; Cheruiyot, N. K.; Nguyen, M. K.; Le, T. H.; Lukkhasorn, W.; Vo, T.-D.-H.; Bui, X.-T. Tropospheric Ozone and NOx<math><msub Is="true"><mrow Is="true"></Mrow><mrow Is="true"><mi Mathvariant="normal" Is="true">x</Mi></Mrow></Msub></Math>: A Review of Worldwide Variation and Meteorological Influences. *Environmental Technology & Innovation* **2022**, *28*, 102809. https://doi.org/10.1016/j.eti.2022.102809.

(201) Cramer, E. S.; Briggs, M. S.; Liu, N.; Mailyan, B.; Dwyer, J. R.; Rassoul, H. K. The Impact on the Ozone Layer from NOx Produced by Terrestrial Gamma Ray Flashes. *Geophysical Research Letters* **2017**, *44* (10), 5240–5245. https://doi.org/10.1002/2017GL073215.
(202) Cox, R. A. Chemical Transformation Processes for NoX Species in the Atmosphere. In *Studies in Environmental Science*; Schneider, T., Grant, L., Eds.; Air Pollution by Nitrogen Oxides; Elsevier, 1982; Vol. 21, pp 249–261. https://doi.org/10.1016/B978-0-444-42127-2.50027-0.
(203) Badr, O.; Probert, S. D. Oxides of Nitrogen in the Earth's Atmosphere: Trends, Sources, Sinks and Environmental Impacts. *Applied Energy* **1993**, *46* (1), 1–67. https://doi.org/10.1016/0306-2619(93)90076-2.
(204) Liu, X.; Zhang, Y.; Han, W.; Tang, A.; Shen, J.; Cui, Z.; Vitousek, P.; Erisman, J. W.; Goulding, K.; Christie, P.; Fangmeier, A.; Zhang, F. Enhanced Nitrogen Deposition over China. *Nature* **2013**, *494* (7438), 459–462. https://doi.org/10.1038/nature11917.
(205) *EU air quality standards - European Commission*. https://environment.ec.europa.eu/topics/air/air-quality/eu-air-quality-standards_en (accessed 2024-07-04).
(206) *CEN - EN 14792 - Stationary source emissions - Determination of mass concentration of nitrogen oxides - Standard reference method: chemiluminescence | GlobalSpec*. https://standards.globalspec.com/std/10069594/EN%2014792 (accessed 2024-07-04).
(207) Zhu, J.; Liu, X.; Xu, Y.; Xu, J.; Wang, H.; Zhang, K.; Cheng, X.; Yu, D. Probing into Volatile Combustion Flame and Particulate Formation Behavior During the Coal and Ammonia Co-Firing Process. *Energy Fuels* **2022**, *36* (16), 9347–9356. https://doi.org/10.1021/acs.energyfuels.2c01450.
(208) Ueki, Y.; Yoshiie, R.; Naruse, I.; Matsuzaki, S. Effect of Hydrogen Gas Addition on Combustion Characteristics of Pulverized Coal. *Fuel Processing Technology* **2017**, *161*, 289–294. https://doi.org/10.1016/j.fuproc.2017.02.034.
(209) Ishihara, S.; Zhang, J.; Ito, T. Numerical Calculation with Detailed Chemistry on Ammonia Co-Firing in a Coal-Fired Boiler: Effect of Ammonia Co-Firing Ratio on NO Emissions. *Fuel* **2020**, *274*, 117742. https://doi.org/10.1016/j.fuel.2020.117742.
(210) Tamura, M.; Gotou, T.; Ishii, H.; Riechelmann, D. Experimental Investigation of Ammonia Combustion in a Bench Scale 1.2 MW-Thermal Pulverised Coal Firing Furnace. *Applied Energy* **2020**, *277*, 115580. https://doi.org/10.1016/j.apenergy.2020.115580.
(211) Zhang, A.; Liu, X.; Xu, Y.; Zhai, Y.; Li, Y.; Xu, M. Effect of Ammonia and Coal Co-Firing on the Formation Mechanism and Composition Characteristics of Particulate Matter. *Fuel* **2024**, *358*, 130231. https://doi.org/10.1016/j.fuel.2023.130231.
(212) Ding, X.; Li, W.; Liu, P.; Kang, Z. Numerical Calculation on Combustion Process and NO Transformation Behavior in a Coal-Fired Boiler Blended Ammonia: Effects of the Injection Position and Blending Ratio. *International Journal of Hydrogen Energy* **2023**, *48* (76), 29771–29785. https://doi.org/10.1016/j.ijhydene.2023.04.140.
(213) Chen, P.; Gong, C.; Hua, C.; Gu, M.; Jiang, B.; Fan, J.; Wang, Y. Mechanism Analysis of Fuel-N Oxidation during Ammonia-Coal Co-Combustion: Influence of H2O. *Fuel* **2023**, *342*, 127747. https://doi.org/10.1016/j.fuel.2023.127747.
(214) Biebl, M.; Leicher, J.; Giese, A.; Wieland, C. A Comprehensive Study of Non-Premixed Combustion of Ammonia and Its Blends: Flame Stability and Emission Reduction. *Fuel* **2025**, *386*, 134501. https://doi.org/10.1016/j.fuel.2025.134501.
(215) Hercog, J.; Lewtak, R.; Glot, B.; Jóźwiak, P.; Nehring, G.; Tavares, V. D.; Nunes, A. M.; Gaspar, D. Pilot Testing and Numerical Simulations of the Multifuel Burner for the Cement Kiln. *Fuel* **2023**, *342*, 127801. https://doi.org/10.1016/j.fuel.2023.127801.
(216) Pisa, I.; Lazaroiu, G.; Prisecaru, T. Influence of Hydrogen Enriched Gas Injection upon Polluting Emissions from Pulverized Coal Combustion. *International Journal of Hydrogen Energy* **2014**, *39* (31), 17702–17709. https://doi.org/10.1016/j.ijhydene.2014.08.119.
(217) İlbaş, M.; Karyeyen, S. A Numerical Study on Combustion Behaviours of Hydrogen-Enriched Low Calorific Value Coal Gases. *International Journal of Hydrogen Energy* **2015**, *40* (44), 15218–15226. https://doi.org/10.1016/j.ijhydene.2015.04.141.

(218) Ehlmé, E.; Gunnarsson, A.; Andersson, K.; Normann, F. Heat Transfer Conditions in Hydrogen-Fired Rotary Kilns for Iron Ore Processing. *Ind. Eng. Chem. Res.* **2023**, *62* (37), 15098–15108. https://doi.org/10.1021/acs.iecr.3c02264.
(219) Gan, M. J.; Liu, Y.; Shen, Y. Co-Injection of Hydrogen and Biochar (CoHB) in a Simulated Blast Furnace: A Univariate and Multivariate Study. *Fuel* **2024**, *371*, 131966. https://doi.org/10.1016/j.fuel.2024.131966.
(220) Ren, M.; Liu, W.; Zhao, J.; Zou, C.; Ren, L.; Wu, H.; Zhao, J. Effects of Hydrogen Fraction in Co-Injection Gas on Combustion Characteristics of the Raceway in Low Carbon Emission Blast Furnace. *International Journal of Hydrogen Energy* **2023**, *48* (30), 11530–11540. https://doi.org/10.1016/j.ijhydene.2022.06.106.
(221) Liu, Y.; Hu, Z.; Shen, Y. CFD Study of Hydrogen Injection in Blast Furnaces: Tuyere Co-Injection of Hydrogen and Coal. *Metall Mater Trans B* **2021**, *52* (5), 2971–2991. https://doi.org/10.1007/s11663-021-02156-z.
(222) Lee, S.; Park, J.; Park, S.; Choi, N.; Shin, J. Experimental Study of Natural Gas and Hydrogen Co-Firing Characteristics Using Different Types of Single Nozzles of F-Class Practical Gas Turbine Combustors. *NaN* **2024**, No. NaN, 1–31. https://doi.org/10.1115/1.4066210.
(223) Kim, K.-M.; Kim, G.-B.; Lee, B.-H.; Jeon, C.-H.; Keum, J.-H. Methane Gas Cofiring Effects on Combustion and NOx Emission in 550 MW Tangentially Fired Pulverized-Coal Boiler. *ACS Omega* **2021**, *6* (46), 31132–31146. https://doi.org/10.1021/acsomega.1c04574.
(224) Miller, J. A.; Bowman, C. T. Mechanism and Modeling of Nitrogen Chemistry in Combustion. *Progress in Energy and Combustion Science* **1989**, *15* (4), 287–338. https://doi.org/10.1016/0360-1285(89)90017-8.
(225) *Gas-Phase Combustion Chemistry*; Gardiner, W. C., Ed.; Springer: New York, NY, 2000. https://doi.org/10.1007/978-1-4612-1310-9.
(226) 26. Oxidation of Nitrogen in Combustion and Explosions. In *26. Oxidation of Nitrogen in Combustion and Explosions*; Princeton University Press, 2014; pp 404–410. https://doi.org/10.1515/9781400862979.404.
(227) Bozzelli, J. W.; Dean, A. M. O + NNH: A Possible New Route for NOX Formation in Flames. *International Journal of Chemical Kinetics* **1995**, *27* (11), 1097–1109. https://doi.org/10.1002/kin.550271107.
(228) Haworth, N. L.; Mackie, J. C.; Bacskay, G. B. An Ab Initio Quantum Chemical and Kinetic Study of the NNH + O Reaction Potential Energy Surface: How Important Is This Route to NO in Combustion? *J. Phys. Chem. A* **2003**, *107* (35), 6792–6803. https://doi.org/10.1021/jp034421p.
(229) Purohit, A. L.; Nalbandyan, A.; Malte, P. C.; Novosselov, I. V. NNH Mechanism in Low-NOx Hydrogen Combustion: Experimental and Numerical Analysis of Formation Pathways. *Fuel* **2021**, *292*, 120186. https://doi.org/10.1016/j.fuel.2021.120186.
(230) Glarborg, P.; Miller, J. A.; Ruscic, B.; Klippenstein, S. J. Modeling Nitrogen Chemistry in Combustion. *Progress in Energy and Combustion Science* **2018**, *67*, 31–68. https://doi.org/10.1016/j.pecs.2018.01.002.
(231) Harrington, J. E.; Smith, G. P.; Berg, P. A.; Noble, A. R.; Jeffries, J. B.; Crosley, D. R. Evidence for a New No Production Mechanism in Flames. *Symposium (International) on Combustion* **1996**, *26* (2), 2133–2138. https://doi.org/10.1016/S0082-0784(96)80038-5.
(232) Durocher, A.; Meulemans, M.; Versailles, P.; Bourque, G.; Bergthorson, J. M. Back to Basics – NO Concentration Measurements in Atmospheric Lean-to-Rich, Low-Temperature, Premixed Hydrogen–Air Flames Diluted with Argon. *Proceedings of the Combustion Institute* **2021**, *38* (2), 2093–2100. https://doi.org/10.1016/j.proci.2020.06.124.
(233) Xu, Z.-F.; Sun, J.-Z. Ab Initio Study on the Mechanism of the Radical Reaction NNH(2A′)+N(4S)→N2+NH(3Σ-). *Chemical Physics Letters* **1997**, *281* (4–6), 452–456. https://doi.org/10.1016/S0009-2614(97)01272-4.
(234) Hayhurst, A. N.; Hutchinson, E. M. Evidence for a New Way of Producing NO via NNH in Fuel- Rich Flames at Atmospheric Pressure. *Combustion and Flame* **1998**, *114* (1–2), 274–279. https://doi.org/10.1016/S0010-2180(97)00328-3.
(235) Konnov, A. A.; Colson, G.; De Ruyck, J. NO Formation Rates for Hydrogen Combustion in Stirred Reactors. *Fuel* **2001**, *80* (1), 49–65. https://doi.org/10.1016/S0016-2361(00)00060-0.

(236) WESTBROOK, C. K.; DRYER, F. L. Simplified Reaction Mechanisms for the Oxidation of Hydrocarbon Fuels in Flames. *Combustion Science and Technology* **1981**, *27* (1–2), 31–43. https://doi.org/10.1080/00102208108946970.
(237) Konnov, A. A.; Colson, G.; De Ruyck, J. The New Route Forming NO via NNH. *Combustion and Flame* **2000**, *121* (3), 548–550. https://doi.org/10.1016/S0010-2180(99)00164-9.
(238) Rørtveit, G. J.; Hustad, J. E.; Li, S.-C.; Williams, F. A. Effects of Diluents on NOx Formation in Hydrogen Counterflow Flames. *Combustion and Flame* **2002**, *130* (1), 48–61. https://doi.org/10.1016/S0010-2180(02)00362-0.
(239) Konnov, A. A.; De Ruyck, J. Temperature-Dependent Rate Constant for the Reaction NNH + O → NH + NO. *Combustion and Flame* **2001**, *125* (4), 1258–1264. https://doi.org/10.1016/S0010-2180(01)00250-4.
(240) Konnov, A. A. On the Relative Importance of Different Routes Forming NO in Hydrogen Flames. *Combustion and Flame* **2003**, *134* (4), 421–424. https://doi.org/10.1016/S0010-2180(03)00135-4.
(241) Rutar, T.; Lee, J. C. Y.; Dagaut, P.; Malte, P. C.; Byrne, A. A. NOx Formation Pathways in Lean-Premixed-Prevapourized Combustion of Fuels with Carbon-to-Hydrogen Ratio between 0.25 and 0.88. *Proceedings of the Institution of Mechanical Engineers, Part A: Journal of Power and Energy* **2007**, *221* (3), 387–398. https://doi.org/10.1243/09576509JPE288.
(242) Skottene, M.; Rian, K. E. A Study of NOx<math><msub Is="true"><mrow Is="true"><mi Is="true">NO</Mi></Mrow><mrow Is="true"><mi Is="true">x</Mi></Mrow></Msub></Math> Formation in Hydrogen Flames. *International Journal of Hydrogen Energy* **2007**, *32* (15), 3572–3585. https://doi.org/10.1016/j.ijhydene.2007.02.038.
(243) Fenimore, C. P. Formation of Nitric Oxide in Premixed Hydrocarbon Flames. *Symposium (International) on Combustion* **1971**, *13* (1), 373–380. https://doi.org/10.1016/S0082-0784(71)80040-1.
(244) Lamoureux, N.; Desgroux, P.; El Bakali, A.; Pauwels, J. F. Experimental and Numerical Study of the Role of NCN in Prompt-NO Formation in Low-Pressure CH4–O2–N2 and C2H2–O2–N2 Flames. *Combustion and Flame* **2010**, *157* (10), 1929–1941. https://doi.org/10.1016/j.combustflame.2010.03.013.
(245) Averitt, P. *Coal Resources of the United States, January 1, 1974*; 1412; U.S. Govt. Print. Off., 1975. https://doi.org/10.3133/b1412.
(246) Miller, B. G.; Tillman, D. A. Chapter 2 - Coal Characteristics. In *Combustion Engineering Issues for Solid Fuel Systems*; Miller, B. G., Tillman, D. A., Eds.; Academic Press: Burlington, 2008; pp 33–81. https://doi.org/10.1016/B978-0-12-373611-6.00002-1.
(247) Davidson, R. M. Nitrogen in Coal. **1994**.
(248) Dzurenda, L.; Hroncová, E.; Ladomerský, J. Extensive Operating Experiments on the Conversion of Fuel-Bound Nitrogen into Nitrogen Oxides in the Combustion of Wood Fuel. *Forests* **2016**, *8* (1), 1. https://doi.org/10.3390/f8010001.
(249) Colin, S.; Normann, F.; Fredriksson, C.; Andersson, K. Flame Characterization of Cofiring Gaseous and Solid Fuels in Suspensions. *ACS Omega* **2024**, *9* (26), 28268–28282. https://doi.org/10.1021/acsomega.4c01770.
(250) Solum, M. S.; Pugmire, R. J.; Grant, D. M. Carbon-13 Solid-State NMR of Argonne-Premium Coals. *Energy Fuels* **1989**, *3* (2), 187–193. https://doi.org/10.1021/ef00014a012.
(251) Mullins, O. C.; Mitra-Kirtley, S.; Van Elp, J.; Cramer, S. P. Molecular Structure of Nitrogen in Coal from XANES Spectroscopy. *Appl Spectrosc* **1993**, *47* (8), 1268–1275. https://doi.org/10.1366/0003702934067991.
(252) Kelemen, S. R.; Gorbaty, M. L.; Kwiatek, P. J. Quantification of Nitrogen Forms in Argonne Premium Coals. *Energy Fuels* **1994**, *8* (4), 896–906. https://doi.org/10.1021/ef00046a013.
(253) Wójtowicz, M. A.; Pels, J. R.; Moulijn, J. A. The Fate of Nitrogen Functionalities in Coal during Pyrolysis and Combustion. *Fuel* **1995**, *74* (4), 507–516. https://doi.org/10.1016/0016-2361(95)98352-F.
(254) Kambara, S.; Takarada, T.; Toyoshima, M.; Kato, K. Relation between Functional Forms of Coal Nitrogen and NOx Emissions from Pulverized Coal Combustion. *Fuel* **1995**, *74* (9), 1247–1253. https://doi.org/10.1016/0016-2361(95)00090-R.

(255) Burchill, P.; Welch, L. S. Variation of Nitrogen Content and Functionality with Rank for Some UK Bituminous Coals. *Fuel* **1989**, *68* (1), 100–104. https://doi.org/10.1016/0016-2361(89)90019-7.
(256) Milne, T. A.; Evans, R. J.; Abatzaglou, N. *Biomass Gasifier "'Tars'": Their Nature, Formation, and Conversion*; NREL/TP-570-25357; ON: DE00003726; National Renewable Energy Laboratory, Golden, CO (US), 1998. https://doi.org/10.2172/3726.
(257) Watt, M.; Fletcher, T. H.; Bai, S.; Solum, M. S.; Pugmire, R. J. Chemical Structure of Coal Tar during Devolatilization. *Symposium (International) on Combustion* **1996**, *26* (2), 3153–3160. https://doi.org/10.1016/S0082-0784(96)80160-3.
(258) Tchapda, A. H.; Krishnamoorthy, V.; Yeboah, Y. D.; Pisupati, S. V. Analysis of Tars Formed during Co-Pyrolysis of Coal and Biomass at High Temperature in Carbon Dioxide Atmosphere. *Journal of Analytical and Applied Pyrolysis* **2017**, *128*, 379–396. https://doi.org/10.1016/j.jaap.2017.09.011.
(259) Solomon, P. R.; Hamblen, D. G.; Carangelo, R. M.; Serio, M. A.; Deshpande, G. V. Models of Tar Formation during Coal Devolatilization. *Combustion and Flame* **1988**, *71* (2), 137–146. https://doi.org/10.1016/0010-2180(88)90003-X.
(260) Fletcher, T. H.; Lignell, D. O.; Josephson, A.; Richards, A.; Holland, T. Advances in Modeling Coal Pyrolysis, Char Combustion, and Soot Formation from Coal and Biomass Tar. In *Clean Coal and Sustainable Energy*; Lyu, J., Li, S., Eds.; Springer: Singapore, 2022; pp 29–37. https://doi.org/10.1007/978-981-16-1657-0_3.
(261) Ma, J.; Fletcher, T. H.; Webb, B. W. Effect of Flame Environment on Soot Formation in Coal Combustion. **1995**.
(262) Jovanovski, G.; Boev, B.; Makreski, P. Chemistry and Geology of Coal: Nature, Composition, Coking, Gasification, Liquefaction, Production of Chemicals, Formation, Peatification, Coalification, Coal Types, and Ranks. *ChemTexts* **2023**, *9* (1), 2. https://doi.org/10.1007/s40828-022-00177-y.
(263) Howard, J. B.; Fong, W. S.; Peters, W. A. Kinetics of Devolatilization. In *Fundamentals of the Physical-Chemistry of Pulverized Coal Combustion*; Lahaye, J., Prado, G., Eds.; Springer Netherlands: Dordrecht, 1987; pp 77–103. https://doi.org/10.1007/978-94-009-3661-4_3.
(264) Pohl, J. H.; Sarofim, A. F. Devolatilization and Oxidation of Coal Nitrogen. *Symposium (International) on Combustion* **1977**, *16* (1), 491–501. https://doi.org/10.1016/S0082-0784(77)80346-9.
(265) Solomon, P. R.; Colket, M. B. Evolution of Fuel Nitrogen in Coal Devolatilization. *Fuel* **1978**, *57* (12), 749–755. https://doi.org/10.1016/0016-2361(78)90133-3.
(266) Zhang, H.; Fletcher, T. H. Nitrogen Transformations during Secondary Coal Pyrolysis. *Energy Fuels* **2001**, *15* (6), 1512–1522. https://doi.org/10.1021/ef010118g.
(267) Blair, D. W.; Wendt, J. O. L.; Bartok, W. Evolution of Nitrogen and Other Species during Controlled Pyrolysis of Coal. *Symposium (International) on Combustion* **1977**, *16* (1), 475–489. https://doi.org/10.1016/S0082-0784(77)80345-7.
(268) Kimber, G. M.; Gray, M. D. Rapid Devolatilization of Small Coal Particles. *Combustion and Flame* **1967**, *11* (4), 360–362. https://doi.org/10.1016/0010-2180(67)90028-4.
(269) van der Lans, R. P.; Glarborg, P.; Dam-Johansen, K. Influence of Process Parameters on Nitrogen Oxide Formation in Pulverized Coal Burners. *Progress in Energy and Combustion Science* **1997**, *23* (4), 349–377. https://doi.org/10.1016/S0360-1285(97)00012-9.
(270) Glarborg, P.; Jensen, A. D.; Johnsson, J. E. Fuel Nitrogen Conversion in Solid Fuel Fired Systems. *Progress in Energy and Combustion Science* **2003**, *29* (2), 89–113. https://doi.org/10.1016/S0360-1285(02)00031-X.
(271) Glarborg, P.; Jensen, A. D.; Johnsson, J. E. Fuel Nitrogen Conversion in Solid Fuel Fired Systems. *Progress in Energy and Combustion Science* **2003**, *29* (2), 89–113. https://doi.org/10.1016/S0360-1285(02)00031-X.
(272) Miller, J. A.; Bowman, C. T. Mechanism and Modeling of Nitrogen Chemistry in Combustion. *Progress in Energy and Combustion Science* **1989**, *15* (4), 287–338. https://doi.org/10.1016/0360-1285(89)90017-8.

(273) Li, C.-Z. Chapter 6 - Conversion of Coal-N and Coal-S during Pyrolysis, Gasification and Combustion. In *Advances in the Science of Victorian Brown Coal*; Li, C.-Z., Ed.; Elsevier Science: Amsterdam, 2004; pp 286–359. https://doi.org/10.1016/B978-008044269-3/50007-8.
(274) Nelson, P. F.; Li, C.-Z.; Ledesma, E. Formation of HNCO from the Rapid Pyrolysis of Coals. *Energy Fuels* **1996**, *10* (1), 264–265. https://doi.org/10.1021/ef950183o.
(275) Wolfrum, J. Bildung von Stickstoffoxiden bei der Verbrennung. *Chemie Ingenieur Technik* **1972**, *44* (10), 656–659. https://doi.org/10.1002/cite.330441004.
(276) Bassilakis, R.; Zhao, Y.; Solomon, P. R.; Serio, M. A. Sulfur and Nitrogen Evolution in the Argonne Coals. Experiment and Modeling. *Energy Fuels* **1993**, *7* (6), 710–720. https://doi.org/10.1021/ef00042a004.
(277) Schäfer, S.; Bonn, B. Hydrolysis of HCN as an Important Step in Nitrogen Oxide Formation in Fluidised Combustion. Part 1. Homogeneous Reactions. *Fuel* **2000**, *79* (10), 1239–1246. https://doi.org/10.1016/S0016-2361(99)00254-9.
(278) Li, C.-Z.; Tan, L. L. Formation of NOx and SOx Precursors during the Pyrolysis of Coal and Biomass. Part III. Further Discussion on the Formation of HCN and NH3 during Pyrolysis. *Fuel* **2000**, *79* (15), 1899–1906. https://doi.org/10.1016/S0016-2361(00)00008-9.
(279) Yuan, S.; 军李; 陈雪莉; 代正华; 周志杰; 王辅臣. Study on NH3 and HCN Formation Mechanisms during Rapid Pyrolysis of Pyrrolic Nitrogen. *JFCT* **2011**, *39* (11), 801–805. https://doi.org/10.0000/j.2097-213X.20113911801805.
(280) Liu, J.; Lu, Q.; Jiang, X.; Hu, B.; Zhang, X.; Dong, C.; Yang, Y. Theoretical Investigation of the Formation Mechanism of NH3 and HCN during Pyrrole Pyrolysis: The Effect of H2O. *Molecules* **2018**, *23* (4), 711. https://doi.org/10.3390/molecules23040711.
(281) Glarborg, P.; Miller, J. A.; Ruscic, B.; Klippenstein, S. J. Modeling Nitrogen Chemistry in Combustion. *Progress in Energy and Combustion Science* **2018**, *67*, 31–68. https://doi.org/10.1016/j.pecs.2018.01.002.
(282) Glarborg, P.; Miller, J. A.; Ruscic, B.; Klippenstein, S. J. Modeling Nitrogen Chemistry in Combustion. *Progress in Energy and Combustion Science* **2018**, *67*, 31–68. https://doi.org/10.1016/j.pecs.2018.01.002.
(283) Smoot, L. Fundamentals of Coal Combustion : For Clean and Efficient Use; 1993.
(284) Solomon, P. R.; Colket, M. B. Evolution of Fuel Nitrogen in Coal Devolatilization. *Fuel* **1978**, *57* (12), 749–755. https://doi.org/10.1016/0016-2361(78)90133-3.
(285) Pershing, D. W.; Wendt, J. O. L. Relative Contributions of Volatile Nitrogen and Char Nitrogen to NOx Emissions from Pulverized Coal Flames. *Ind. Eng. Chem. Proc. Des. Dev.* **1979**, *18* (1), 60–67. https://doi.org/10.1021/i260069a008.
(286) Spinti, J. P.; Pershing, D. W. The Fate of Char-N at Pulverized Coal Conditions. *Combustion and Flame* **2003**, *135* (3), 299–313. https://doi.org/10.1016/S0010-2180(03)00168-8.
(287) Jensen, L. S.; Jannerup, H. E.; Glarborg, P.; Jensen, A.; Dam-Johansen, K. Experimental Investigation of No from Pulverized Char Combustion. *Proceedings of the Combustion Institute* **2000**, *28* (2), 2271–2278. https://doi.org/10.1016/S0082-0784(00)80637-2.
(288) Brix, J.; Navascués, L. G.; Nielsen, J. B.; Bonnek, P. L.; Larsen, H. E.; Clausen, S.; Glarborg, P.; Jensen, A. D. Oxy-Fuel Combustion of Millimeter-Sized Coal Char: Particle Temperatures and NO Formation. *Fuel* **2013**, *106*, 72–78. https://doi.org/10.1016/j.fuel.2013.01.017.
(289) Spinti, J. P.; Pershing, D. W. The Fate of Char-N at Pulverized Coal Conditions. *Combustion and Flame* **2003**, *135* (3), 299–313. https://doi.org/10.1016/S0010-2180(03)00168-8.
(290) Nelson, P. F.; Nancarrow, P. C.; Bus, J.; Prokopiuk, A. Fractional Conversion of Char N to No in an Entrained Flow Reactor. *Proceedings of the Combustion Institute* **2002**, *29* (2), 2267–2274. https://doi.org/10.1016/S1540-7489(02)80276-0.
(291) Molina, A.; Eddings, E. G.; Pershing, D. W.; Sarofim, A. F. Nitric Oxide Destruction during Coal and Char Oxidation under Pulverized-Coal Combustion Conditions. *Combustion and Flame* **2004**, *136* (3), 303–312. https://doi.org/10.1016/j.combustflame.2003.10.009.
(292) Song, Y. H.; Pohl, J. H.; Beér, J. M.; Sarofim, A. F. Nitric Oxide Formation During Pulverized Coal Combustion. *Combustion Science and Technology* **1982**, *28* (1–2), 31–40. https://doi.org/10.1080/00102208208952538.

(293) Pershing, D. W.; Wendt, J. O. L. Relative Contributions of Volatile Nitrogen and Char Nitrogen to NOx Emissions from Pulverized Coal Flames. *Ind. Eng. Chem. Proc. Des. Dev.* **1979**, *18* (1), 60–67. https://doi.org/10.1021/i260069a008.
(294) Phong-Anant, D.; Wibberley, L. J.; Wall, T. F. Nitrogen Oxide Formation from Australian Coals. *Combustion and Flame* **1985**, *62* (1), 21–30. https://doi.org/10.1016/0010-2180(85)90090-2.
(295) Molina, A.; Eddings, E. G.; Pershing, D. W.; Sarofim, A. F. Char Nitrogen Conversion: Implications to Emissions from Coal-Fired Utility Boilers. *Progress in Energy and Combustion Science* **2000**, *26* (4), 507–531. https://doi.org/10.1016/S0360-1285(00)00010-1.
(296) Molina, A.; Murphy, J. J.; Winter, F.; Haynes, B. S.; Blevins, L. G.; Shaddix, C. R. Pathways for Conversion of Char Nitrogen to Nitric Oxide during Pulverized Coal Combustion. *Combustion and Flame* **2009**, *156* (3), 574–587. https://doi.org/10.1016/j.combustflame.2008.11.012.
(297) Visona, S. P.; Stanmore, B. R. Modeling NOx Release from a Single Coal Particle II. Formation of NO from Char-Nitrogen. *Combustion and Flame* **1996**, *106* (3), 207–218. https://doi.org/10.1016/0010-2180(95)00257-X.
(298) Shimizu, T.; Sazawa, Y.; Adschiri, T.; Furusawa, T. Conversion of Char-Bound Nitrogen to Nitric Oxide during Combustion. *Fuel* **1992**, *71* (4), 361–365. https://doi.org/10.1016/0016-2361(92)90022-G.
(299) Pohl, J. H.; Sarofim, A. F. Devolatilization and Oxidation of Coal Nitrogen. *Symposium (International) on Combustion* **1977**, *16* (1), 491–501. https://doi.org/10.1016/S0082-0784(77)80346-9.
(300) Solomon, P. R.; Colket, M. B. Evolution of Fuel Nitrogen in Coal Devolatilization. *Fuel* **1978**, *57* (12), 749–755. https://doi.org/10.1016/0016-2361(78)90133-3.
(301) Blair, D. W.; Wendt, J. O. L.; Bartok, W. Evolution of Nitrogen and Other Species during Controlled Pyrolysis of Coal. *Symposium (International) on Combustion* **1977**, *16* (1), 475–489. https://doi.org/10.1016/S0082-0784(77)80345-7.
(302) Zhang, H.; Fletcher, T. H. Nitrogen Transformations during Secondary Coal Pyrolysis. *Energy Fuels* **2001**, *15* (6), 1512–1522. https://doi.org/10.1021/ef010118g.
(303) Song, G.-L.; Lv, Q.-G.; Zhou, J.-H.; Cen, K.-F. Effect of Pulverized Coal Concentration on Emission Characteristics of NO x. In *Challenges of Power Engineering and Environment*; Cen, K., Chi, Y., Wang, F., Eds.; Springer Berlin Heidelberg: Berlin, Heidelberg, 2007; pp 727–732. https://doi.org/10.1007/978-3-540-76694-0_136.
(304) Hansson, K.-M.; Samuelsson, J.; Tullin, C.; Åmand, L.-E. Formation of HNCO, HCN, and NH3 from the Pyrolysis of Bark and Nitrogen-Containing Model Compounds. *Combustion and Flame* **2004**, *137* (3), 265–277. https://doi.org/10.1016/j.combustflame.2004.01.005.
(305) Pershing, D. W.; Wendt, J. O. L. Relative Contributions of Volatile Nitrogen and Char Nitrogen to NOx Emissions from Pulverized Coal Flames. *Ind. Eng. Chem. Proc. Des. Dev.* **1979**, *18* (1), 60–67. https://doi.org/10.1021/i260069a008.
(306) Edland, R.; Normann, F.; Andersson, K. Modeling the Contributions of Volatile and Char-Bound Nitrogen to the Formation of NOx Species in Iron Ore Rotary Kilns. *Energy Fuels* **2018**, *32* (2), 2321–2331. https://doi.org/10.1021/acs.energyfuels.7b02707.
(307) Meulemans, M.; Durocher, A.; Bourque, G.; Bergthorson, J. M. NO Measurements in High Temperature Hydrogen Flames: The Crucial Role of the Hydrogen Oxidation Chemistry for Accurate NO Predictions. *Combustion and Flame* **2024**, *261*, 113279. https://doi.org/10.1016/j.combustflame.2023.113279.
(308) Lee, S.-R.; Park, S.-S.; Chung, S.-H. Flame Structure and Thermal NOx Formation in Hydrogen Diffusion Flames with Reduced Kinetic Mechanisms. *KSME Journal* **1995**, *9* (3), 377–384. https://doi.org/10.1007/BF02953636.
(309) Edland, R.; Normann, F.; Allgurén, T.; Fredriksson, C.; Andersson, K. Scaling of Pulverized-Fuel Jet Flames That Apply Large Amounts of Excess Air—Implications for NOx Formation. *Energies* **2019**, *12* (14), 2680. https://doi.org/10.3390/en12142680.
(310) SMART, J. P.; MORGAN, D. J. Exploring the Effects of Employing Different Scaling Criteria on Swirl Stabilised Pulverised Coal Burner Performance. *Combustion Science and Technology* **1994**, *100* (1–6), 331–343. https://doi.org/10.1080/00102209408935459.

(311) Weber, R. Scaling Characteristics of Aerodynamics, Heat Transfer, and Pollutant Emissions in Industrial Flames. *Symposium (International) on Combustion* **1996**, *26* (2), 3343–3354. https://doi.org/10.1016/S0082-0784(96)80182-2.
(312) *(PDF) Fundamental Scaling of NOx Emissions from Burners and Furnaces*. ResearchGate. https://www.researchgate.net/publication/252903335_Fundamental_Scaling_of_NOx_Emissions_from_Burners_and_Furnaces (accessed 2025-02-20).
(313) Sun, P.; Zhang, T.; Huang, X. Size Scale Effect on Mass Burning Flux and Flame Behavior of Solid Fuels. *J Therm Anal Calorim* **2024**, *149* (17), 9575–9586. https://doi.org/10.1007/s10973-024-13453-5.
(314) Reburning of Nitric Oxide in Oxy-Fuel Firing—The Influence of Combustion Conditions | Request PDF. *ResearchGate* **2024**. https://doi.org/10.1021/ef101054t.
(315) (PDF) K–Cl–S Chemistry in Air and Oxy-Combustion Atmospheres. *ResearchGate* **2024**. https://doi.org/10.1016/j.proci.2016.08.069.
(316) (PDF) Formation of Soot in Oxygen-Enriched Turbulent Propane Flames at the Technical Scale. *ResearchGate* **2024**. https://doi.org/10.3390/en13010191.
(317) Mendiara, T.; Glarborg, P. Ammonia Chemistry in Oxy-Fuel Combustion of Methane. *Combustion and Flame* **2009**, *156* (10), 1937–1949. https://doi.org/10.1016/j.combustflame.2009.07.006.
(318) Wiinikka, H.; Sepman, A.; Ögren, Y.; Lindblom, B.; Nordin, L.-O. Combustion Evaluation of Renewable Fuels for Iron-Ore Pellet Induration. *Energy Fuels* **2019**, *33* (8), 7819–7829. https://doi.org/10.1021/acs.energyfuels.9b01356.
(319) Johansson, A.; Fernberg, J.; Sepman, A.; Colin, S.; Wennebro, J.; Normann, F.; Wiinikka, H. Cofiring of Hydrogen and Pulverized Coal in Rotary Kilns Using One Integrated Burner. *International Journal of Hydrogen Energy* **2024**, *90*, 342–352. https://doi.org/10.1016/j.ijhydene.2024.09.327.
(320) Larsson, I. A. S.; Johansson, S. P. A.; Lundström, T. S.; Marjavaara, B. D. PIV/PLIF Experiments of Jet Mixing in a Model of a Rotary Kiln. *Exp Fluids* **2015**, *56* (5), 111. https://doi.org/10.1007/s00348-015-1984-9.
(321) Sepman, A.; Fredriksson, C.; Ögren, Y.; Wiinikka, H. Laser-Based, Optical, and Traditional Diagnostics of NO and Temperature in 400 kW Pilot-Scale Furnace. *Applied Sciences* **2021**, *11* (15), 7048. https://doi.org/10.3390/app11157048.
(322) Sefidari, H.; Ma, C.; Fredriksson, C.; Lindblom, B.; Wiinikka, H.; Nordin, L. O.; Wu, G.; Yazhenskikh, E.; Müller, M.; Öhman, M. The Effect of Co-Firing Coal and Woody Biomass upon the Slagging/Deposition Tendency in Iron-Ore Pelletizing Grate-Kiln Plants. *Fuel Processing Technology* **2020**, *199*, 106254. https://doi.org/10.1016/j.fuproc.2019.106254.
(323) Edland, R.; Smith, N.; Allgurén, T.; Fredriksson, C.; Normann, F.; Haycock, D.; Johnson, C.; Frandsen, J.; Fletcher, T. H.; Andersson, K. Evaluation of NOx-Reduction Measures for Iron-Ore Rotary Kilns. *Energy Fuels* **2020**, *34* (4), 4934–4948. https://doi.org/10.1021/acs.energyfuels.9b04091.
(324) Salzer, R. Peter R. Griffiths, James A. de Haseth: Fourier Transform Infrared Spectrometry (2nd Edn.). *Anal Bioanal Chem* **2008**, *391* (7), 2379–2380. https://doi.org/10.1007/s00216-008-2144-3.
(325) FTIRProtocol.Pdf. https://www3.epa.gov/ttn/emc/ftir/FTIRProtocol.pdf?utm_source=chatgpt.com (accessed 2025-03-15).
(326) (PDF) Quantitative Measurement of Combustion Gases in Harsh Environments Using NDIR Spectroscopy. *ResearchGate* **2024**. https://doi.org/10.5194/jsss-8-123-2019.
(327) A Review on Non-Dispersive Infrared Gas Sensors: Improvement of Sensor Detection Limit and Interference Correction | Request PDF. *ResearchGate* **2024**. https://doi.org/10.1016/j.snb.2016.03.040.
(328) Stetter, J. R.; Li, J. Amperometric Gas SensorsA Review. *Chem. Rev.* **2008**, *108* (2), 352–366. https://doi.org/10.1021/cr0681039.
(329) Jasek, K.; Pasternak, M.; Grabka, M. Paramagnetic Sensors for the Determination of Oxygen Concentration in Gas Mixtures. *ACS Sens.* **2022**, *7* (11), 3228–3242. https://doi.org/10.1021/acssensors.2c00938.

(330) Sepman, A.; Ögren, Y.; Gullberg, M.; Wiinikka, H. Development of TDLAS Sensor for Diagnostics of CO, H2O and Soot Concentrations in Reactor Core of Pilot-Scale Gasifier. *Appl. Phys. B* **2016**, *122* (2), 29. https://doi.org/10.1007/s00340-016-6319-x.
(331) Gas-Phase-Ftir-Spectroscopy-Introduction-BR52338.Pdf. https://assets.thermofisher.com/TFS-Assets/MSD/brochures/gas-phase-ftir-spectroscopy-introduction-BR52338.pdf?utm_source=chatgpt.com (accessed 2025-02-19).
(332) Tóth, P.; Ögren, Y.; Sepman, A.; Vikström, T.; Gren, P.; Wiinikka, H. Spray Combustion of Biomass Fast Pyrolysis Oil: Experiments and Modeling. *Fuel* **2019**, *237*, 580–591. https://doi.org/10.1016/j.fuel.2018.10.031.
(333) Ögren, Y.; Gullberg, M.; Wennebro, J.; Sepman, A.; Tóth, P.; Wiinikka, H. Influence of Oxidizer Injection Angle on the Entrained Flow Gasification of Torrefied Wood Powder. *Fuel Processing Technology* **2018**, *181*, 8–17. https://doi.org/10.1016/j.fuproc.2018.09.005.
(334) *Tunable Diode Laser Spectrometers | Yokogawa Electric Corporation*. https://www.yokogawa.com/solutions/products-and-services/measurement/analyzers/gas-analyzers/tunable-diode-laser-spectrometer/#Details (accessed 2025-02-23).
(335) Yang, X.; Peng, Z.; Ding, Y.; Du, Y. Temperature and OH Concentration Measurements by Ultraviolet Broadband Absorption of OH(X) in Laminar Methane/Air Premixed Flames. *Fuel* **2021**, *288*, 119666. https://doi.org/10.1016/j.fuel.2020.119666.
(336) Sepman, A.; Fredriksson, C.; Ögren, Y.; Wiinikka, H. Laser-Based, Optical, and Traditional Diagnostics of NO and Temperature in 400 kW Pilot-Scale Furnace. *Applied Sciences* **2021**, *11* (15), 7048. https://doi.org/10.3390/app11157048.
(337) *The water-cooled suction pyrometer – theory, design and calibration*. https://ifrf.net/research/archive/the-water-cooled-suction-pyrometer-theory-design-and-calibration/ (accessed 2025-01-23).
(338) Ekland, R.; Allguren, T.; Fredriksson, C.; Haycock, D.; Johnson, C.; Fransen, J.; Fletcher, T.; Andersson, K. Evaluation of NOx-Reduction Measures for Iron-Ore Rotary Kilns. *Faculty Publications* **2020**.
(339) *X-MOL*. x-mol.net. https://www.x-mol.net/paper/article/1336467896413577216 (accessed 2025-02-22).
(340) Xin-Yu Y.; Zhi-Min P.; Yan-Jun D.; Yan-Jun D. Synchronic measurements of temperatures and concentrations of OH, NH, and NO in flames based on broadband ultraviolet absorption spectroscopy. *Acta Phys. Sin.* **2022**, *71* (17), 173301–173311. https://doi.org/10.7498/aps.71.20220208.
(341) Liu, N.; Chen, T. Y.; Zhong, H.; Lin, Y.; Wang, Z.; Ju, Y. Femtosecond Ultraviolet Laser Absorption Spectroscopy for Simultaneous Measurements of Temperature and OH Concentration. *Applied Physics Letters* **2022**, *120* (20), 201103. https://doi.org/10.1063/5.0091572.
(342) (PDF) OH Concentration and Temperature Measurements Using Femtosecond Ultraviolet Laser Absorption Spectroscopy. In *ResearchGate*.
(343) Tian, X.; Yang, J.; Gong, Y.; Guo, Q.; Wang, X.; Yu, G. Experimental Study on OH*, CH*, and CO2* Chemiluminescence Diagnosis of CH4/O2 Diffusion Flame with CO2-Diluted Fuel. *ACS Omega* **2022**, *7* (45), 41137–41146. https://doi.org/10.1021/acsomega.2c04689.
(344) Liu, Y.; Tan, J.; Wan, M.; Zhang, L.; Yao, X. Quantitative Measurement of OH* and CH* Chemiluminescence in Jet Diffusion Flames. *ACS Omega* **2020**, *5* (26), 15922–15930. https://doi.org/10.1021/acsomega.0c01093.
(345) Vaidya, D. B.; Horvath, J. J.; Green, A. E. S. Remote Temperature Measurements in Gas and Gas–Coal Flames Using the OH(0,0) Middle-UV Band. *Appl. Opt., AO* **1982**, *21* (18), 3357–3362. https://doi.org/10.1364/AO.21.003357.